

สำนักหอสมุดกลาง พระจอมเกล้าลาดกระบัง

A SWITCHED-BEAM FLAT DIVERSITY ANTENNA



**A THESIS SUBMITTED IN PARTIAL FULFILLMENT OF
THE REQUIREMENT FOR THE DEGREE OF
MASTER OF ENGINEERING IN ELECTRICAL ENGINEERING
SCHOOL OF GRADUATE STUDIES
KING MONGKUT'S INSTITUTE OF TECHNOLOGY LADKRABANG**

2001

ISBN 974-648-039-1

เลขหม.....
เลขทะเบียน..... 37747
วัน, เดือน, ปี..... 16 ส.ค. 2544

This material is provided for educational use only, not allowed for commercial use.
You are not allowed to modify the content, and cite the document when use.



COPYRIGHT 2001

SCHOOL OF GRADUATE STUDIES

KING MONGKUT'S INSTITUTE OF TECHNOLOGY LADKRABANG

This material is reserved for educational use only, not allowed for commercial use.

Forbidden to modify the content, and cite the document when use.

หัวข้อวิทยานิพนธ์	สายอากาศไดเวอร์ซิติแบบแบนที่สามารถสวิตช์ลำคลื่นได้
นักศึกษา	นายไพศาล งามจรรยาภรณ์
รหัสประจำตัว	41061061
ปริญญา	วิศวกรรมศาสตรมหาบัณฑิต
สาขาวิชา	วิศวกรรมไฟฟ้า
พ.ศ.	2544
อาจารย์ผู้ควบคุมวิทยานิพนธ์	รศ.ดร.โมไนย ไกรฤกษ์

บทคัดย่อ

วิทยานิพนธ์ฉบับนี้เป็นการนำเสนอสายอากาศไดเวอร์ซิติแบบแบนที่สามารถสวิตช์ลำคลื่นได้ เป็นสายอากาศแพทเทิร์นไดเวอร์ซิติเพื่อประยุกต์ใช้สำหรับการสื่อสารเคลื่อนที่ในระบบโครงข่ายท้องถิ่นไร้สายที่ย่านความถี่ไอเอสเอ็ม โดยโครงสร้างของสายอากาศเป็นสายอากาศวงจรมิพรีรูปสี่เหลี่ยมจัตุรัส ซึ่งมีน้ำหนักเบา ขนาดเล็ก เหมาะสำหรับสายอากาศในระบบการสื่อสารเคลื่อนที่ นอกจากนี้ที่แต่ละด้านของสายอากาศจะมีสวิตช์ความถี่วิทยุต่ออยู่เพื่อใช้ในการสวิตช์ลำคลื่นของสายอากาศสำหรับการประยุกต์ใช้งานเป็นสายอากาศแพทเทิร์นไดเวอร์ซิติ โดยในวิทยานิพนธ์นี้ได้ทำการวิเคราะห์คุณลักษณะการแพร่กระจายคลื่นของสายอากาศด้วยวิธีผลต่างสืบเนื่องเชิงเวลาเพื่อหาขนาดของสายอากาศและตำแหน่งของสวิตช์ความถี่วิทยุที่เหมาะสมที่จะทำให้สายอากาศมีคุณลักษณะการแพร่กระจายคลื่นที่เหมาะสมแก่การประยุกต์ใช้งานเป็นสายอากาศแพทเทิร์นไดเวอร์ซิติ ซึ่งจากผลการวิเคราะห์คุณลักษณะการแพร่กระจายคลื่นของสายอากาศก็ได้นำมาทำการวิเคราะห์คุณลักษณะเชิงไดเวอร์ซิติของสายอากาศ หลังจากนั้นจึงทำการสร้างสายอากาศตามโครงสร้างที่เหมาะสมที่ได้จากการวิเคราะห์และทำการทดสอบคุณลักษณะการแพร่กระจายคลื่นและคุณลักษณะเชิงไดเวอร์ซิติของสายอากาศ ซึ่งจากการทดสอบพบว่าผลที่ได้มีความสอดคล้องกับผลการวิเคราะห์ และแสดงให้เห็นว่าสายอากาศนี้มีคุณลักษณะที่สามารถประยุกต์ใช้งานในระบบโครงข่ายท้องถิ่นไร้สายได้

Thesis Title	A Switched-Beam Flat Diversity Antenna
Student	Mr. Phaisan Ngamjahyaporn
Student ID.	41061061
Degree	Master of Engineering
Programme	Electrical Engineering
Year	2001
Thesis Advisor	Assoc. Prof. Dr. Monai Krairiksh

ABSTRACT

This thesis proposes a switched-beam flat diversity antenna that is a pattern diversity antenna for mobile communication in wireless local area network (WLAN) system at ISM frequency band. The structure of the antenna is a square printed antenna, which is light weight and small size that are required for the mobile antenna. In addition, the RF switches are installed on each side of the antenna for switching the beam of antenna in order that the pattern diversity technique can be accomplished. In this thesis, the radiation characteristics of the antenna are analyzed by using the Finite-Difference Time-Domain (FDTD) method. The size of the antenna and position of the RF switches on each side of the antenna that result the optimum radiation characteristics of the antenna for applying in WLAN system and suitable for pattern diversity technique are found out. The diversity characteristics of the antenna are also investigated. Subsequently, the prototype of a switched-beam flat diversity antenna is fabricated. The radiation characteristics and diversity characteristics of the antenna are tested. The experimental results agree with the calculation and the characteristics of the antenna are validated for WLAN system.

ACKNOWLEDGEMENTS

This thesis can be completed with the contributions from many persons that I am appreciative of their help and I would like to take this chance to express my appreciation to them.

Firstly, I am thankful to my advisor, Associate Professor Monai Krairiksh, who gives me many helpful suggestion and useful advice for this research. I also appreciate his attention and stimulating the progress of this research.

I would like to appreciate to Assistant Professor Sompol Kosulvit for his kindly discussions. Also, I would like to appreciate to Associate Professor Pramote Wardkien for his helpful suggestion for the switched combining circuit.

I would like to acknowledge PHILIPS ELECTRONICS (THAILAND) Ltd. for supporting of PIN diodes that are used in this research.

I would like to thank to my colleagues in Wireless Communication Laboratory for their friendship and generosity. I also appreciate many experience and knowledge that I have received from this laboratory.

Finally, I am very grateful for my parents who always support and encourage for everything and every time in my life.

Phaisan Ngamjanyaporn

TABLE OF CONTENTS

	page
Abstract (Thai).....	I
Abstract (English)	II
Acknowledgements.....	III
Table of Contents.....	IV
List of Figures.....	VI
Chapter 1 Introduction.....	1
1.1 Literature of the Diversity Antennas.....	1
1.2 Purpose and Scope of the Thesis.....	2
Chapter 2 Finite-Difference Time-Domain Method for Antenna Analysis.....	4
2.1 Finite-Difference Time-Domain Formulations.....	4
2.2 Perfectly Matched Layer Absorbing Boundary Condition.....	10
2.3 Antenna Excitation and Feed Models.....	14
2.3.1 Excitation.....	14
2.3.2 Feed models.....	15
2.4 Near-Field to Far-Field Transformations.....	20
2.4.1 Frequency-domain near-field to far-field transformation.....	22
2.4.2 Time-domain near-field to far-field transformation.....	27
2.5 Conclusions.....	29
Chapter 3 A Switched-Beam Flat Diversity Antenna.....	31
3.1 Antenna Configuration.....	31
3.2 FDTD Model.....	32
3.3 Conclusions.....	34
Chapter 4 Radiation Characteristics of the Antenna.....	36
4.1 Radiation Patterns.....	36
4.2 Directivity.....	41
4.3 Experimental Results.....	43
4.4 Conclusions.....	47

This material is reserved for educational use only, not allowed for commercial use.

Forbidden to modify the content, and cite the document when use.

TABLE OF CONTENTS (to)

	page
Chapter 5 Diversity Characteristics of the Antenna.....	49
5.1 Correlation Coefficient.....	49
5.2 Diversity Gain.....	54
5.3 Experimental Results.....	58
5.4 Conclusions.....	62
Chapter 6 Conclusions.....	64
References.....	66
Appendices.....	70
Appendix A Derivations of Stability Criterion.....	71
Appendix B Propagation of Plane Wave in PML Medium.....	75
Appendix C Data Sheet of BAP51-02 General Purpose PIN Diode.....	79
Author Biography.....	85

LIST OF FIGURES

Fig.	Page
2.1 Subdivisions of the computational volume into discrete grid cells.....	7
2.2 Positions of six field components on the Yee cell.....	8
2.3 Structure of two-dimensional FDTD grid with PML ABC.....	12
2.4 (a) Gaussian pulse.....	15
(b) Differentiated Gaussian pulse.....	15
2.5 Delta-gap feed model.....	16
2.6 Magnetic frill feed model.....	17
2.7 Coaxial line feed model.....	18
2.8 Geometry of the problem with zone transformation.....	20
2.9 Zone transformation over the virtual surface.....	21
2.10 The average of the four neighboring values for magnetic field.....	23
3.1 Antenna configuration.....	31
3.2 FDTD model and dimensions of the problem space.....	33
3.3 Relationships for field components at the PMC image plane.....	34
4.1 Radiation patterns of the antenna with single RF switch on each side of the antenna	36
4.2 Comparative results of the radiation pattern from the ninth period data (solid line) and the radiation pattern from various period data (dot line).....	37
(a) second period.....	37
(b) third period.....	37
(c) seventh period.....	37
(d) eighth period.....	37
4.3 Radiation patterns obtained from FDTD model with various grid size.....	38
4.4 Radiation patterns of the antenna with the shorting posts.....	39
(a) Azimuth plane.....	39
(b) Elevation plane.....	39
4.5 Radiation patterns of the antenna without the shorting posts.....	40
(a) Azimuth plane.....	40
(b) Elevation plane.....	40

LIST OF FIGURES (to)

Fig.	Page
4.6 Comparisons of radiation patterns of the antenna with and without shorting posts...	41
(a) x direction.....	41
(b) y direction.....	41
4.7 Switched-beam pattern of the antenna.....	41
4.8 Calculated directivity with respect to d	43
4.9 Prototype of the antenna.....	44
4.10 Radiation patterns in azimuth plane.....	45
(a) x direction.....	45
(b) y direction.....	45
4.11 Radiation patterns in elevation plane.....	46
4.12 Measured directivity with respect to frequency.....	47
5.1 Relation between correlation coefficient and the RF switches spacing d	52
5.2 Calculated envelope correlation coefficient of the antenna.....	53
5.3 Switched combining techniques.....	56
(a) Two fading signals.....	56
(b) Resultant signal using switch-and-stay strategy.....	56
(c) Resultant signal using switch-and-examine strategy.....	56
5.4 CDF of received signal after combining for switched combining with $A = -10$ dB for correlated branches.....	57
5.5 CDF of received signal after combining for switched combining with different values of A for correlated branches with the envelope correlation coefficient of 0.5	58
5.6 Measured envelope correlation coefficient as a function of d	59
5.7 Diagram of the switched combining circuit.....	60
5.8 Antenna with switched combining circuit.....	61
5.9 Radiation pattern of a switched beam flat diversity antenna.....	61
5.10 Cumulative probability and diversity gain.....	62

CHAPTER 1

INTRODUCTION

1.1 Literature of the Diversity Antennas

In mobile communication system, the received signals suffer from multipath fading that is encountered in both indoor and outdoor environments. Multipath fading is caused by reflection, refraction and diffraction of the signals in surrounding environment between transmitting and receiving sites. However, fading signal can be improved by diversity techniques. The diversity techniques are usually applied at the receiving site, and various techniques can be implemented, such as space diversity, polarization diversity and pattern diversity [1]-[4]. There are many publications presented diversity antennas for various diversity schemes for vehicle and portable telephone [5]-[11]. Most of diversity antennas are applied for cellular telephone systems. However, the diversity antenna can be applied for other wireless communication systems. Such wireless local area network (WLAN) system, the diversity antennas are proposed for base and mobile terminal antennas [12]-[18]. The pattern diversity antenna is mostly proposed, and a low-profile antenna is also required, especially for mobile terminal. To realize the pattern diversity antenna for mobile terminal, Kuga and Arai proposed a flat switched-beam array antenna [14]. Four elements of a trapezoidal conducting cavity with an aperture are used to form a square array. Each element is fed through 3-dB hybrid coupler, and excited by an equal amplitude with phase difference 90° . Beam switching is carried out by switching input terminals of the hybrid couplers. This causes sophisticated antenna feeding. A switched-beam flat antenna with simple feed was proposed [19]. The antenna structure is based on center-fed half wavelength printed antenna, and beam switching is accomplished by switching the radio frequency (RF) switches which connected on each side of the printed antenna. Accordingly, the antenna is satisfied to flat and low-profile antenna structure, which is required for mobile terminal antenna, and the complexity of the antenna feeding can be reduced by using only a single printed antenna structure. The characteristics and performance of the antenna show that the antenna can be applied for pattern diversity antenna and suitable for mobile terminal.

1.2 Purpose and Scope of the Thesis

The objective of this thesis is to investigate a switched-beam flat diversity antenna, which is a pattern diversity antenna for mobile terminal in WLAN system. The antenna is analyzed by using the Finite-Difference Time-Domain (FDTD) method. The radiation characteristics and the diversity characteristics of the antenna are investigated. The method and results are provided in the remainder of the this thesis as follows:

Chapter 2 introduces the Finite-Difference Time-Domain method for antenna analysis. The basic elements of FDTD antenna analysis are provided. Finite-Difference Time-Domain equations for updating the electric and magnetic fields in time-domain are derived in rectangular coordinate, and the stability criterion for FDTD calculation in rectangular coordinate is also presented. The Perfectly Matched Layer (PML) absorbing boundary condition is presented for unbounded or radiation problem simulation. Antenna excitation and feed models for FDTD simulation are presented, and frequency-domain near-field to far-field (FD-NFFF) transformation and time-domain near-field to far-field (TD-NFFF) transformation techniques are introduced for far-zone calculation.

Chapter 3 presents the antenna configuration of a switched-beam flat diversity antenna and the model of the antenna for FDTD antenna analysis. The dimension of the antenna, the dielectric constant of the substrate, thickness and property of PML absorbing boundary and position of the transformation surfaces are specified including to the antenna feeding and excitation.

Chapter 4 shows the investigation of the radiation characteristics of the antenna. The radiation patterns and directivity of the antenna are investigated as a function of the spacing d between two RF switches on each side of the antenna by using the FDTD method with the FDTD model in Chapter 3. The experimental results are obtained and compared with the numerical results.

Chapter 5 evaluates the diversity characteristics of the antenna. The correlation coefficient of the antenna is evaluated by using the knowledge of the radiation patterns obtained in Chapter 4 and the Clarke's model as the angular density function of incident waves. The diversity gain of the antenna is evaluated in case of switched combining technique for correlated signals with the obtained correlation coefficient of the antenna. Also, the measurement is set up to test the characteristics of the antenna.

Chapter 6 summarizes the material that is obtained in preceding chapters and includes the discussion for further works.

In addition, the derivation of the stability criterion for FDTD calculation in rectangular coordinate is provided in Appendix A, and the proof of PML absorbing boundary condition for incident plane wave is illustrated in Appendix B.



CHAPTER 2

FINITE-DIFFERENCE TIME-DOMAIN METHOD FOR ANTENNA ANALYSIS

Generally, antenna analysis can be performed by several methods, especially, the numerical methods. The well-known numerical methods are method of moment, finite-element and finite-difference time-domain methods. The finite-difference time-domain (FDTD) method is the efficient one because it can give the accurate modeling and analysis of the antenna with realistic material and structure.

In this chapter, the basic elements for the FDTD analysis of an antenna are addressed. The FDTD equations, Perfectly Matched Layer (PML) absorbing boundary condition, antenna excitation and feed models and Near-Field to Far-Field (NFFF) transformations are introduced, respectively.

2.1 Finite-Difference Time-Domain Formulations

The FDTD algorithm is directly derived from Maxwell's equations in differential form. By using the vector identity for curl of a vector, the Maxwell's equations are written out in form of its corresponding three coordinate components resulting a system of six differential equations. Subsequently, the finite-difference schemes are utilized to approximate the system of six differential equations to form the FDTD equations. In this section, formulation of FDTD equations in rectangular coordinates is introduced. Also, the stability criterion for FDTD in rectangular coordinate is included.

Consider Maxwell's equations in differential form,

$$\nabla \times \bar{E} = -\bar{J}_m - \frac{\partial \bar{B}}{\partial t}, \quad (2.1a)$$

$$\nabla \times \bar{H} = \bar{J}_c + \frac{\partial \bar{D}}{\partial t}, \quad (2.1b)$$

where \bar{E} and \bar{H} are electric and magnetic field intensities. \bar{D} and \bar{B} are electric and magnetic flux densities. \bar{J}_c and \bar{J}_m are electric and equivalent magnetic conduction current densities.

In linear and isotropic nondispersive medium, \bar{B} and \bar{D} can be related to \bar{H} and \bar{E} , respectively, by the constitutive parameter as

$$\bar{B} = \mu \bar{H}, \quad (2.2a)$$

$$\bar{D} = \varepsilon \bar{E}, \quad (2.2b)$$

where μ and ε are permeability and permittivity of the medium, respectively. Also, considering the electric and magnetic losses in medium, \bar{J}_c and \bar{J}_m can be related to \bar{E} and \bar{H} , respectively, as

$$\bar{J}_c = \sigma \bar{E}, \quad (2.2c)$$

$$\bar{J}_m = \sigma^* \bar{H}, \quad (2.2d)$$

where σ and σ^* are electric conductivity and magnetic loss, respectively.

Substituting (2.2a) through (2.2d) into (2.1a) and (2.1b) and rearranging terms,

$$\mu \frac{\partial \bar{H}}{\partial t} + \sigma^* \bar{H} = -\nabla \times \bar{E}, \quad (2.3a)$$

$$\varepsilon \frac{\partial \bar{E}}{\partial t} + \sigma \bar{E} = \nabla \times \bar{H}. \quad (2.3b)$$

By using the vector identity for curl of a vector in rectangular coordinates,

$$\nabla \times \bar{A} = \bar{a}_x \left[\frac{\partial A_z}{\partial y} - \frac{\partial A_y}{\partial z} \right] + \bar{a}_y \left[\frac{\partial A_x}{\partial z} - \frac{\partial A_z}{\partial x} \right] + \bar{a}_z \left[\frac{\partial A_y}{\partial x} - \frac{\partial A_x}{\partial y} \right], \quad (2.4)$$

to write out the vector components of the curl operator in (2.3a) and (2.3b) to yield the following system of six differential equations,

$$\mu \frac{\partial H_x}{\partial t} + \sigma^* H_x = \frac{\partial E_y}{\partial z} - \frac{\partial E_z}{\partial y}, \quad (2.5a)$$

$$\mu \frac{\partial H_y}{\partial t} + \sigma^* H_y = \frac{\partial E_z}{\partial x} - \frac{\partial E_x}{\partial z}, \quad (2.5b)$$

$$\mu \frac{\partial H_z}{\partial t} + \sigma^* H_z = \frac{\partial E_x}{\partial y} - \frac{\partial E_y}{\partial x}, \quad (2.5c)$$

$$\varepsilon \frac{\partial E_x}{\partial t} + \sigma E_x = \frac{\partial H_z}{\partial y} - \frac{\partial H_y}{\partial z}, \quad (2.6a)$$

$$\varepsilon \frac{\partial E_y}{\partial t} + \sigma E_y = \frac{\partial H_x}{\partial z} - \frac{\partial H_z}{\partial x}, \quad (2.6b)$$

$$\varepsilon \frac{\partial E_z}{\partial t} + \sigma E_z = \frac{\partial H_y}{\partial x} - \frac{\partial H_x}{\partial y}. \quad (2.6c)$$

The system of six differential equations in (2.5a) through (2.6c) forms the basis equations for FDTD algorithm. Yee [20] introduced using the central differences to approximate the solution of the system of (2.5a) through (2.6c).

In order to apply the central difference formula to find the solution of the function, $f(x, y, z, t)$, the computational volume is subdivided into discrete grid cells as shown in Fig. 2.1. From Fig. 2.1 the discrete space and time relationship can be written as

$$\begin{aligned} x &= i\Delta x, & i &= 0, 1, 2, \dots, I_{max} \\ y &= j\Delta y, & j &= 0, 1, 2, \dots, J_{max} \\ z &= k\Delta z, & k &= 0, 1, 2, \dots, K_{max} \\ t &= n\Delta t, & n &= 0, 1, 2, \dots, N_{max} \end{aligned}$$

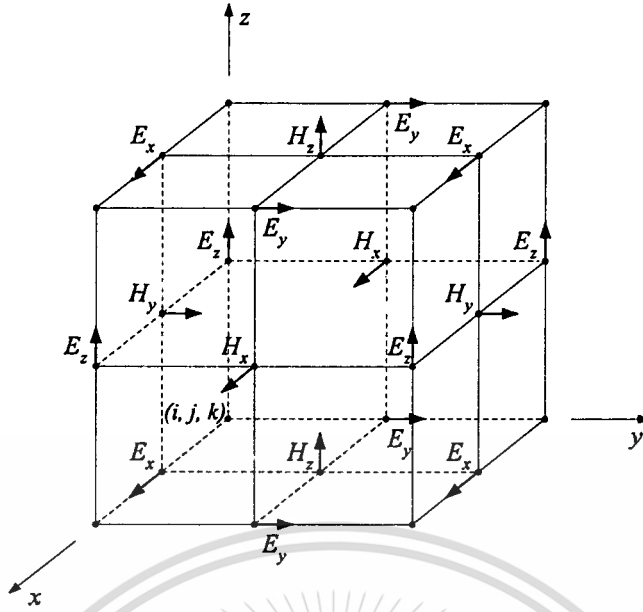


Fig. 2.2 Positions of six field components on the Yee cell

Additionally, the $H_x|_{i,j,k}^n$ term is approximated by averaging the magnetic field component H_x at the advance ($n+1/2$) and previous ($n-1/2$) time steps, as shown below,

$$H_x|_{i,j,k}^n = \frac{H_x|_{i,j,k}^{n+1/2} + H_x|_{i,j,k}^{n-1/2}}{2}. \quad (2.10)$$

Substituting (2.10) into (2.9), then rearranging the terms, the recurrence relation can be obtained as

$$H_x|_{i,j,k}^{n+1/2} = \left(\frac{1 - \frac{\sigma_{i,j,k}^* \Delta t}{2\mu_{i,j,k}}}{1 + \frac{\sigma_{i,j,k}^* \Delta t}{2\mu_{i,j,k}}} \right) H_x|_{i,j,k}^{n-1/2} + \left(\frac{\frac{\Delta t}{\mu_{i,j,k}}}{1 + \frac{\sigma_{i,j,k}^* \Delta t}{2\mu_{i,j,k}}} \right) \left(\frac{E_y|_{i,j,k+1/2}^n - E_y|_{i,j,k-1/2}^n}{\Delta z} - \frac{E_z|_{i,j+1/2,k}^n - E_z|_{i,j-1/2,k}^n}{\Delta y} \right) \quad (2.11a)$$

Similarly, (2.5b) and (2.5c) can be derived to get the recurrence relations, respectively, as

$$H_y|_{i,j,k}^{n+1/2} = \left(\frac{1 - \frac{\sigma_{i,j,k}^* \Delta t}{2\mu_{i,j,k}}}{1 + \frac{\sigma_{i,j,k}^* \Delta t}{2\mu_{i,j,k}}} \right) H_y|_{i,j,k}^{n-1/2} + \left(\frac{\frac{\Delta t}{\mu_{i,j,k}}}{1 + \frac{\sigma_{i,j,k}^* \Delta t}{2\mu_{i,j,k}}} \right) \begin{pmatrix} \frac{E_z|_{i+1/2,j,k}^n - E_z|_{i-1/2,j,k}^n}{\Delta x} \\ -\frac{E_x|_{i,j,k+1/2}^n - E_x|_{i,j,k-1/2}^n}{\Delta z} \end{pmatrix}, \quad (2.11b)$$

$$H_z|_{i,j,k}^{n+1/2} = \left(\frac{1 - \frac{\sigma_{i,j,k}^* \Delta t}{2\mu_{i,j,k}}}{1 + \frac{\sigma_{i,j,k}^* \Delta t}{2\mu_{i,j,k}}} \right) H_z|_{i,j,k}^{n-1/2} + \left(\frac{\frac{\Delta t}{\mu_{i,j,k}}}{1 + \frac{\sigma_{i,j,k}^* \Delta t}{2\mu_{i,j,k}}} \right) \begin{pmatrix} \frac{E_x|_{i,j+1/2,k}^n - E_x|_{i,j-1/2,k}^n}{\Delta y} \\ -\frac{E_y|_{i+1/2,j,k}^n - E_y|_{i-1/2,j,k}^n}{\Delta x} \end{pmatrix}. \quad (2.11c)$$

By the same manner, the FDTD equations for electric field components E_x , E_y and E_z can be obtained, respectively, as

$$E_x|_{i,j,k}^{n+1} = \left(\frac{1 - \frac{\sigma_{i,j,k} \Delta t}{2\varepsilon_{i,j,k}}}{1 + \frac{\sigma_{i,j,k} \Delta t}{2\varepsilon_{i,j,k}}} \right) E_x|_{i,j,k}^n + \left(\frac{\frac{\Delta t}{\varepsilon_{i,j,k}}}{1 + \frac{\sigma_{i,j,k} \Delta t}{2\varepsilon_{i,j,k}}} \right) \begin{pmatrix} \frac{H_z|_{i,j+1/2,k}^{n+1/2} - H_z|_{i,j-1/2,k}^{n+1/2}}{\Delta y} \\ \frac{H_y|_{i,j,k+1/2}^{n+1/2} - H_y|_{i,j,k-1/2}^{n+1/2}}{\Delta z} \end{pmatrix}, \quad (2.12a)$$

$$E_y|_{i,j,k}^{n+1} = \left(\frac{1 - \frac{\sigma_{i,j,k} \Delta t}{2\varepsilon_{i,j,k}}}{1 + \frac{\sigma_{i,j,k} \Delta t}{2\varepsilon_{i,j,k}}} \right) E_y|_{i,j,k}^n + \left(\frac{\frac{\Delta t}{\varepsilon_{i,j,k}}}{1 + \frac{\sigma_{i,j,k} \Delta t}{2\varepsilon_{i,j,k}}} \right) \begin{pmatrix} \frac{H_x|_{i,j,k+1/2}^{n+1/2} - H_x|_{i,j,k-1/2}^{n+1/2}}{\Delta z} \\ -\frac{H_z|_{i+1/2,j,k}^{n+1/2} - H_z|_{i-1/2,j,k}^{n+1/2}}{\Delta x} \end{pmatrix}, \quad (2.12b)$$

$$E_z|_{i,j,k}^{n+1} = \left(\frac{1 - \frac{\sigma_{i,j,k} \Delta t}{2\varepsilon_{i,j,k}}}{1 + \frac{\sigma_{i,j,k} \Delta t}{2\varepsilon_{i,j,k}}} \right) E_z|_{i,j,k}^n + \left(\frac{\frac{\Delta t}{\varepsilon_{i,j,k}}}{1 + \frac{\sigma_{i,j,k} \Delta t}{2\varepsilon_{i,j,k}}} \right) \begin{pmatrix} \frac{H_y|_{i+1/2,j,k}^{n+1/2} - H_y|_{i-1/2,j,k}^{n+1/2}}{\Delta x} \\ -\frac{H_x|_{i,j+1/2,k}^{n+1/2} - H_x|_{i,j-1/2,k}^{n+1/2}}{\Delta y} \end{pmatrix}. \quad (2.12c)$$

Also, the stability criterion which is necessary for determination of the stable region in finite-difference calculation is introduced. The derivation is included in Appendix A. For FDTD in rectangular coordinates, the stability criterion is given as

$$\Delta t \leq \frac{1}{v \sqrt{\frac{1}{(\Delta x)^2} + \frac{1}{(\Delta y)^2} + \frac{1}{(\Delta z)^2}}}, \quad (2.13)$$

where v is maximum phase velocity in computational volume. The above equation provides the upper bound of the time increment Δt that makes the computations still be stable.

2.2 Perfectly Matched Layer Absorbing Boundary Condition

In case of the unbounded electromagnetic problems, the boundary conditions with small nonphysical reflections that are used to truncate solution regions are called radiation boundary conditions (RBCs) or absorbing boundary conditions (ABCs). The most powerful ABC is the perfectly matched layer (PML), which is proposed by Berenger [21]. This approach is based upon splitting of electric or magnetic field components in the absorbing boundary region with the possibility of assigning losses to the individual split field components.

Consider Maxwell's equations in two dimensions for the TE polarization case, where the problem is without variation of electric field along z , it is lying in the xy plane. The electromagnetic field involves three components only, E_x , E_y , H_z , and the Maxwell's equations are reduced to

$$\epsilon_o \frac{\partial E_x}{\partial t} + \sigma E_x = \frac{\partial H_z}{\partial y}, \quad (2.14a)$$

$$\epsilon_o \frac{\partial E_y}{\partial t} + \sigma E_y = -\frac{\partial H_z}{\partial x}, \quad (2.14b)$$

$$\mu_o \frac{\partial H_z}{\partial t} + \sigma^* H_z = \frac{\partial E_x}{\partial y} - \frac{\partial E_y}{\partial x}, \quad (2.14c)$$

where ϵ_o and μ_o are the free-space permittivity and permeability, σ and σ^* denote, respectively, a possible electric conductivity and magnetic loss assigned to free space. Moreover, if the condition

This material is reserved for educational use only, not allowed for commercial use.

Forbidden to modify the content, and cite the document when use.

$$\frac{\sigma}{\varepsilon_0} = \frac{\sigma^*}{\mu_0}, \quad (2.15)$$

is satisfied, then the wave impedance of the lossy free-space medium equals that of lossless vacuum and no reflection occurs when a plane wave propagates normally across an interface between vacuum and lossy free-space medium.

Following to the PML approach, the magnetic field components H_z is split into two subcomponents that are denoted as H_{zx} and H_{zy} . Thus, in the TE case, the absorbing boundary (PML) region is defined as a medium in which the electromagnetic field has four components, E_x , E_y , H_{zx} and H_{zy} . The four field components are coupled by the following equations,

$$\varepsilon_0 \frac{\partial E_x}{\partial t} + \sigma_y E_x = \frac{\partial(H_{zx} + H_{zy})}{\partial y}, \quad (2.16a)$$

$$\varepsilon_0 \frac{\partial E_y}{\partial t} + \sigma_x E_y = -\frac{\partial(H_{zx} + H_{zy})}{\partial x}, \quad (2.16b)$$

$$\mu_0 \frac{\partial H_{zx}}{\partial t} + \sigma_x^* H_{zx} = -\frac{\partial E_y}{\partial x}, \quad (2.16c)$$

$$\mu_0 \frac{\partial H_{zy}}{\partial t} + \sigma_y^* H_{zy} = \frac{\partial E_x}{\partial y}, \quad (2.16d)$$

where σ_x and σ_y denote electric conductivities, and σ_x^* and σ_y^* denote magnetic losses in x and y directions.

From the above equations of (2.16a) through (2.16d), if $\sigma_y = \sigma_y^* = 0$, the PML medium can absorb a plane wave having field components (E_y, H_{zx}) propagating along x , but does not absorb a wave having field components (E_x, H_{zy}) propagating along y , since in the first case propagation is governed by (2.16b) and (2.16c), and in the second case by (2.16a) and (2.16d), and vice versa for wave having field components (E_y, H_{zx}) and (E_x, H_{zy}) if $\sigma_x = \sigma_x^* = 0$. Therefore, the properties of PML medium is characterized by parameters $(\sigma_x, \sigma_x^*, 0, 0)$ and $(\sigma_y, \sigma_y^*, 0, 0)$. That is, if (σ_x, σ_x^*) and (σ_y, σ_y^*) satisfy

This material is reserved for educational use only, not allowed for commercial use.

Forbidden to modify the content, and cite the document when use.

(2.15), then reflection does not occur at vacuum-PML interfaces normal respectively to x and y , which is proved in Appendix B.

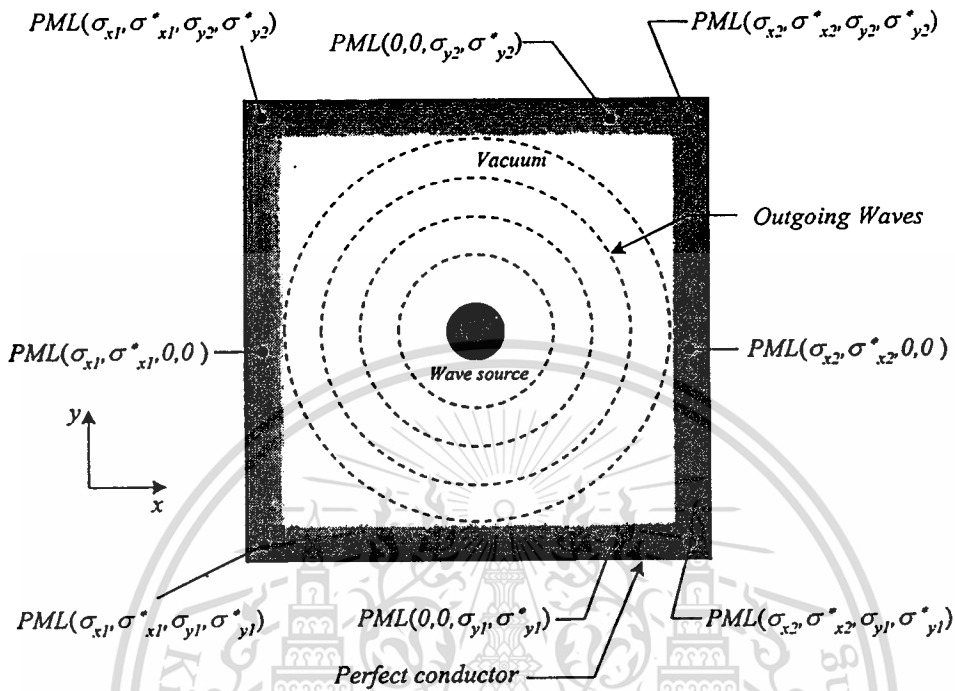


Fig. 2.3 Structure of two-dimensional FDTD grid with PML ABC

Consider the two-dimensional TE FDTD grid, which is a normal free-space computational zone surrounded by a PML backed by perfectly electric conducting (PEC) walls, as shown in Fig. 2.3. From Fig.2.3, each PML at both left and right sides of the grid has only σ_x , and σ_x^* , $(\sigma_x, \sigma_x^*, 0, 0)$, and each PML at both upper and lower sides of the grid has only σ_y , and σ_y^* , $(\sigma_y, \sigma_y^*, 0, 0)$, as described previously, whereas all of σ_x , σ_x^* , σ_y and σ_y^* are present at the four corners the grid where there is overlap of two PMLs. Furthermore, profile of the loss with depth ρ within each PML is following ($n = 1$ for linear, $n = 2$ for parabolic)

$$\sigma(\rho) = \sigma_{max} \left(\frac{\rho}{\delta} \right)^n, \quad (2.17)$$

where δ is the PML thickness and σ is either σ_x or σ_y . This yields a PML reflection coefficient ($R(\theta)$) of

This material is reserved for educational use only, not allowed for commercial use.

Forbidden to modify the content, and cite the document when use.

$$R(\theta) = e^{-2\sigma_{max}\delta \cos\theta / (n+1)\epsilon_0 c} . \quad (2.18a)$$

where c is the speed of light. Thus, at $\theta = 0^\circ$, the theoretical reflection coefficient at normal incidence for the PML over PEC is given by

$$R(0) = e^{-2\sigma_{max}\delta / (n+1)\epsilon_0 c} . \quad (2.18b)$$

By specifying the reflection coefficient in (2.18b), σ_{max} is obtained, then substituting σ_{max} into (2.17) to get σ (σ_x or σ_y) at depth ρ within PML.

Since the wave is attenuated rapidly when propagating inside PML medium, the standard FDTD equations could not be used. Therefore, the use of FDTD equations with exponential time-stepping is preferred. The FDTD equation with exponential time-stepping, for example, is written as [22]

$$E_y \Big|_{i,j+1/2}^{n+1} = e^{-\sigma\Delta t/\epsilon_0} \cdot E_y \Big|_{i,j+1/2}^n + \frac{1}{\sigma\Delta x} \left(e^{-\sigma\Delta t/\epsilon_0} - 1 \right) \cdot \left(H_z \Big|_{i+1/2,j+1/2}^{n+1/2} - H_z \Big|_{i-1/2,j+1/2}^{n+1/2} \right) . \quad (2.19)$$

In three dimensions, all six field components are split, and the resulting PML modification of Maxwell's equations yields 12 equations, as follows:

$$\mu_0 \frac{\partial H_{xy}}{\partial t} + \sigma_y^* H_{xy} = - \frac{\partial (E_{xz} + E_{zy})}{\partial y} , \quad (2.20a)$$

$$\mu_0 \frac{\partial H_{xz}}{\partial t} + \sigma_z^* H_{xz} = \frac{\partial (E_{yx} + E_{yz})}{\partial z} , \quad (2.20b)$$

$$\mu_0 \frac{\partial H_{yz}}{\partial t} + \sigma_z^* H_{yz} = - \frac{\partial (E_{xy} + E_{xz})}{\partial z} , \quad (2.20c)$$

$$\mu_0 \frac{\partial H_{yx}}{\partial t} + \sigma_x^* H_{yx} = \frac{\partial (E_{zx} + E_{zy})}{\partial x} , \quad (2.20d)$$

$$\mu_0 \frac{\partial H_{zx}}{\partial t} + \sigma_x^* H_{zx} = - \frac{\partial (E_{yx} + E_{yz})}{\partial x} , \quad (2.20e)$$

$$\mu_o \frac{\partial H_{zy}}{\partial t} + \sigma_y^* H_{zy} = \frac{\partial(E_{xy} + E_{xz})}{\partial y}, \quad (2.20f)$$

$$\epsilon_o \frac{\partial E_{xy}}{\partial t} + \sigma_y E_{xy} = \frac{\partial(H_{zx} + H_{zy})}{\partial y}, \quad (2.21a)$$

$$\epsilon_o \frac{\partial E_{xz}}{\partial t} + \sigma_z E_{xz} = -\frac{\partial(H_{yx} + H_{yz})}{\partial z}, \quad (2.21b)$$

$$\epsilon_o \frac{\partial E_{yz}}{\partial t} + \sigma_z E_{yz} = \frac{\partial(H_{xy} + H_{xz})}{\partial z}, \quad (2.21c)$$

$$\epsilon_o \frac{\partial E_{yx}}{\partial t} + \sigma_x E_{yx} = -\frac{\partial(H_{zx} + H_{zy})}{\partial x}, \quad (2.21d)$$

$$\epsilon_o \frac{\partial E_{zx}}{\partial t} + \sigma_x E_{zx} = \frac{\partial(H_{yx} + H_{yz})}{\partial x}, \quad (2.21e)$$

$$\epsilon_o \frac{\partial E_{zy}}{\partial t} + \sigma_y E_{zy} = -\frac{\partial(H_{yx} + H_{yz})}{\partial y}. \quad (2.21f)$$

PML matching conditions analogous to the TE case is used.

2.3 Antenna Excitation and Feed Models

In this section, antenna excitation and feed models that are the most important elements of the antenna problem are introduced, especially for transmitting antenna. The implementation of these elements depends upon the particular application. There are various types of excitation and feed model can be applied by using the FDTD method.

2.3.1 Excitation

When the antenna is analyzed at a single frequency, a continuous sinusoidal wave of frequency f_o can be used as an excitation and a length of time is required for the electromagnetic field quantities of interest to reach the sinusoidal steady state. The input voltage at the feed point will be

$$V_{in}(t) = V_o \sin 2\pi f_o t. \quad (2.22)$$

In case of analysis over a band of frequencies, it is efficient to excite the antenna with a pulsed signal. The Gaussian pulse shown in Fig. 2.4(a) can be used for this purpose and the input voltage at the feed point will be

$$V_{in}(t) = V_o \exp[-(t/\tau_p)^2/2]. \quad (2.23a)$$

where τ_p is the characteristics time. However, the Gaussian pulse has high spectrum content near a low frequency range, sometimes, it is not desired for application involving high frequency ranges. An alternative solution is to use the differentiated Gaussian pulse shown in Fig. 2.4(b) because the pulse peaks at the frequency, $\omega_p = 1/\tau_p$, which can be selected by users. The input voltage at the feed point can be written as

$$V_{in}(t) = -V_o (t/\tau_p) \exp\left\{-\left[\left(t/\tau_p\right)^2 - 1\right]/2\right\}. \quad (2.23b)$$

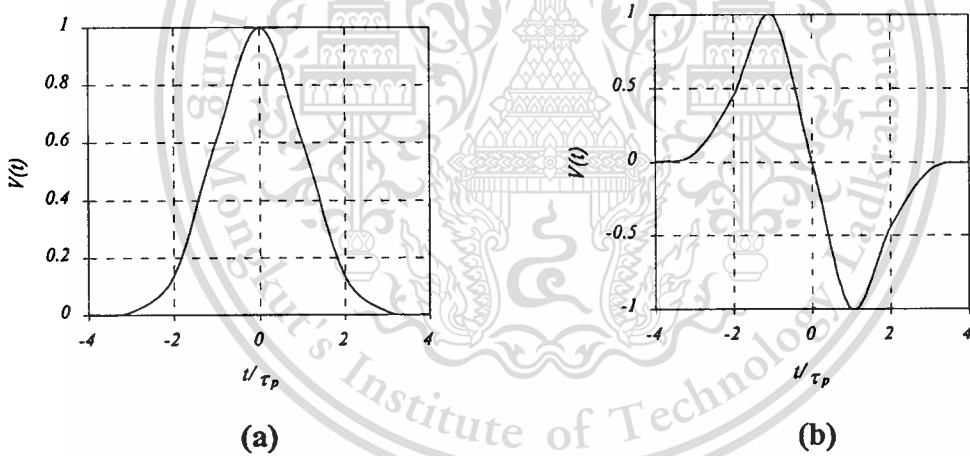


Fig. 2.4 (a) Gaussian pulse (b) Differentiated Gaussian pulse

2.3.2 Feed models

The antenna feeding can be accomplished by various methods. The coaxial probe feed is one of antenna feeding methods that is simple and can be used properly for various antenna structures such as horn antenna, microstrip antenna. In this subsection, the models of the coaxial probe feed in FDTD method are introduced.

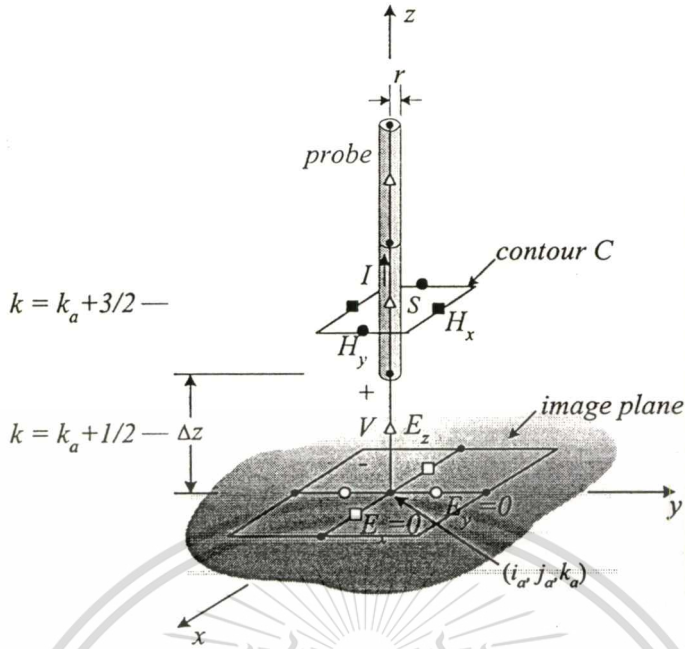


Fig. 2.5 Delta-gap feed model

Firstly, the simplest model, which is corresponding to the delta-gap feed [23], is illustrated in Fig. 2.5. In the feed region, a gap of length Δz exists between the probe and image plane. The lower end of the gap is on the image plane at (i_a, j_a, k_a) . In the probe, the E_z component of the electric field is set to zero, and on the image plane the E_x and E_y components are set to zero. The E_z at the gap is related to the applied voltage $V(t)$ as

$$E_z|_{i_a, j_a, k_a + 1/2}^n = \frac{V(n\Delta t)}{\Delta z}. \quad (2.24)$$

The current in the probe at the feed point is obtained by applying Ampere's law to the surface S with the bounding contour C centered on the probe at $(i_a, j_a, k_a + 3/2)$:

$$\oint_C \bar{H} \cdot d\bar{l} = \iint_S \bar{J} \cdot d\bar{S} + \epsilon_o \iint_S \frac{\partial \bar{E}}{\partial t} \cdot d\bar{S}. \quad (2.25)$$

This gives

$$I|^{n+1/2} = \Delta y \left(H_y|_{i_a+1/2, j_a, k_a+3/2}^{n+1/2} - H_y|_{i_a-1/2, j_a, k_a+3/2}^{n+1/2} \right) \quad (2.26)$$

This material is reserved for educational use only; not allowed for commercial use.

Forbidden to modify the content, and cite the document when use.

where the four magnetic field components that surround the probe are updated using the standard thin-wire FDTD equations [24]; for example,

$$H_y \Big|_{i_a+1/2, j_a, k_a+3/2}^{n+1/2} = H_y \Big|_{i_a+1/2, j_a, k_a+3/2}^{n-1/2} + \left(\frac{\Delta t}{\mu_o \Delta z} \right) \left(E_x \Big|_{i_a+1/2, j_a, k_a+1}^n - E_x \Big|_{i_a+1/2, j_a, k_a+2}^n \right) + \left(\frac{\Delta t}{\mu_o \Delta x} \right) \left(\frac{2}{\ln(\Delta x / r)} \right) E_z \Big|_{i_a+1/2, j_a, k_a+3/2}^n \quad (2.27)$$

The next approach for modeling the coaxial probe feed in FDTD method is shown in Fig. 2.6.

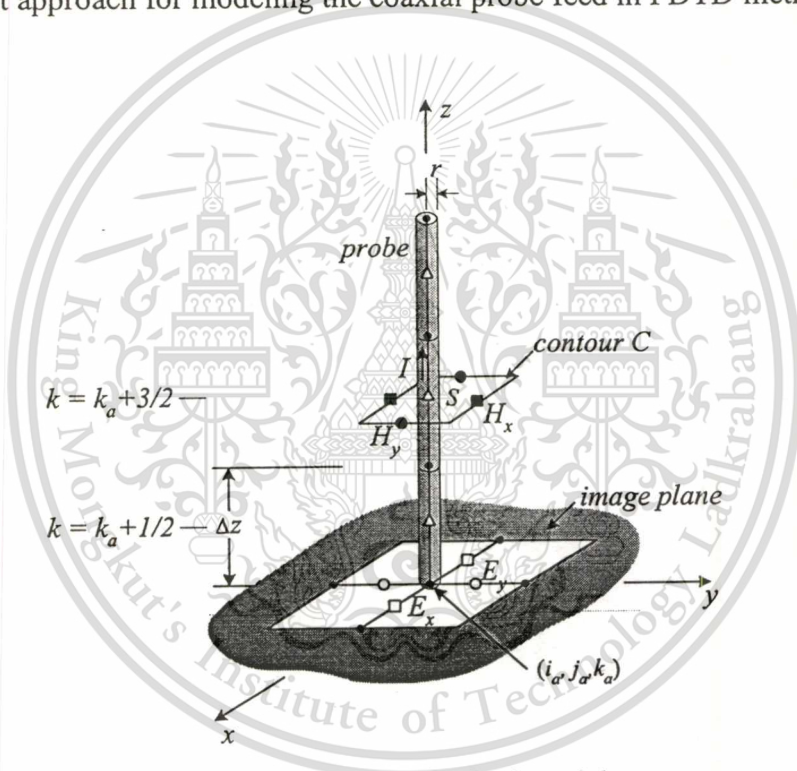


Fig. 2.6 Magnetic frill feed model

By this method, the magnetic frill method is applied [25]. The E_z components along the probe are all set to zero, including the one just above the image plane. But the four electric components on the image plane going radially from the base of the probe, (i_a, j_a, k_a) , are driven. Thus, the E_x and E_y components at the base of the probe are driven as

$$E_x \Big|_{i_a, j_a, k_a}^n = -E_x \Big|_{i_a-1, j_a, k_a}^n = -\frac{V(n\Delta t)}{\ln\left(\frac{\Delta x}{r}\right)} \quad (2.28a)$$

This material is reserved for educational use only, not allowed for commercial use.

Forbidden to modify the content, and cite the document when use.

$$E_y \Big|_{i_a, j_a, k_a}^n = -E_y \Big|_{i_a, j_a - 1, k_a}^n = -\frac{V(n\Delta t)}{\ln\left(\frac{\Delta y}{r}\right)}, \quad (2.28b)$$

where r is the radius of the probe. The current in the probe and four magnetic field components surrounding the probe are computed by (2.26) and (2.27), respectively, as described in previous model.

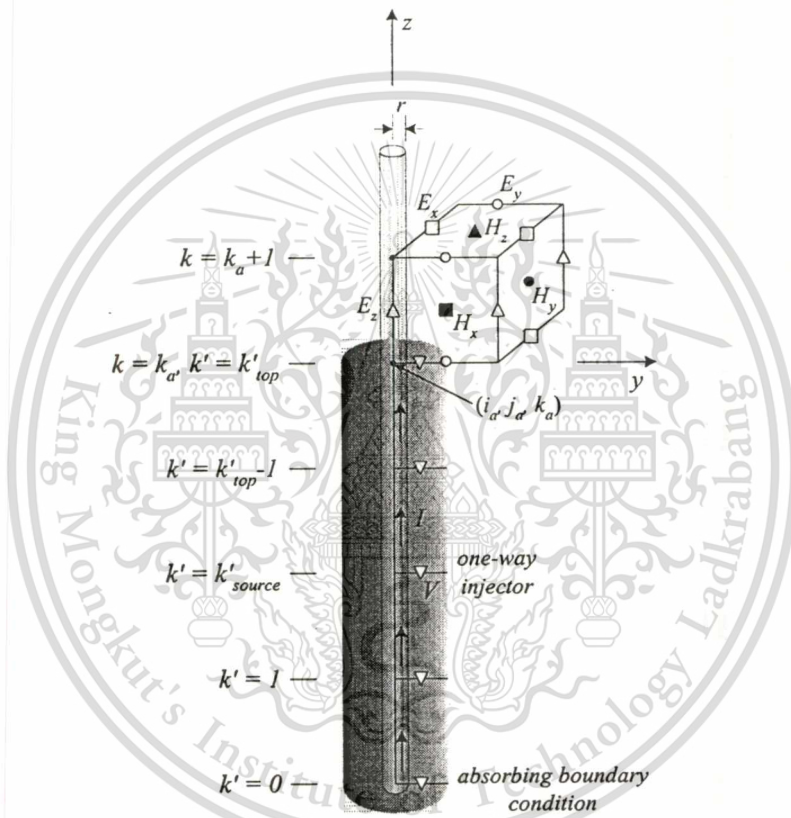


Fig. 2.7 Coaxial line feed model

Furthermore, the full model that includes the transmission line model also be introduced in FDTD method. In this model, the one-dimensional FDTD grid shown in Fig. 2.7 is used to represent the transmission line attach to the probe [26]. The index k' locates a point within one-dimensional grid. The FDTD lattice used for the probe is three-dimensional, and the set indices (i, j, k) locates the point within this lattice. The top end of the transmission line is at point k'_{top} in the one-dimensional grid, and the feed point (the center of the aperture in the coaxial line) is at (i_a, j_a, k_a) in the three-dimensional lattice.

The spatial step within the one-dimensional grid is Δz , the same as the spatial step for the z coordinate in the three-dimensional lattice.

The current and voltage on the transmission line are updated as follow:

$$I|_{k'+1/2}^{n+1/2} = I|_{k'+1/2}^{n-1/2} - \left(\frac{1}{Z_o} \right) \left(\frac{v\Delta t}{\Delta z} \right) (V|_{k'+1}^n - V|_{k'}^n), \quad (2.29a)$$

$$V|_{k'}^{n+1} = V|_{k'}^n - Z_o \left(\frac{v\Delta t}{\Delta z} \right) (I|_{k'+1/2}^{n+1/2} - I|_{k'-1/2}^{n+1/2}), \quad (2.29b)$$

where Z_o is the characteristic impedance, and v is the phase velocity for the transmission line.

To update the voltage in the aperture, $k' = k'_{top}$, the current above the aperture is needed. That is computed from (2.26) but the equations for the magnetic field components that surround the probe at the connection are modified to include the voltage in the aperture,

$$H_y|_{i_a+1/2, j_a, k_a+1/2}^{n+1/2} = H_y|_{i_a+1/2, j_a, k_a+1/2}^{n-1/2} + \left(\frac{\Delta t}{\mu_o \Delta z} \right) \left(\left(\frac{2}{\ln(\Delta x / r)} \right) \frac{V|_{k'_{top}}^n}{\Delta x} - E_x|_{i_a+1/2, j_a, k_a+1}^n \right) + \left(\frac{\Delta t}{\mu_o \Delta x} \right) \left(\frac{2}{\ln(\Delta x / r)} \right) E_z|_{i_a+1, j_a, k_a+1/2}^n. \quad (2.30)$$

The input voltage (V_{in}) is introduced into the coaxial line using a one-way injector at position $k' = k'_{source}$ as follow:

$$I|_{k'_{source}+1/2}^{n+1/2} = I|_{k'_{source}+1/2}^{n-1/2} - \left(\frac{1}{Z_o} \right) \left(\frac{v\Delta t}{\Delta z} \right) [V|_{k'_{source}+1}^n - V|_{k'_{source}}^n] + \left(\frac{1}{Z_o} \right) \left(\frac{v\Delta t}{\Delta z} \right) V_{in}|_{k'_{source}}^n, \quad (2.31a)$$

$$V|_{k'_{source}}^{n+1} = V|_{k'_{source}}^n - Z_o \left(\frac{v\Delta t}{\Delta z} \right) [I|_{k'_{source}+1/2}^{n+1/2} - I|_{k'_{source}-1/2}^{n+1/2}] + \left(\frac{v\Delta t}{\Delta z} \right) V_{in}|_{k'_{source}+1/2}^{n+1/2}. \quad (2.31b)$$

The bottom of the coaxial line, $k' = 0$, is truncated with an absorbing boundary condition.

This material is reserved for educational use only, not allowed for commercial use.

Forbidden to modify the content, and cite the document when use.

2.4 Near Field to Far Field Transformations

Actually, the FDTD method is an inconvenient tool for direct far-field analysis, by directly extending a computational space to reach the far-field region. This is a restriction of the method because of the computational costs, i.e., CPU time and storage memory. Thus, some of auxiliary schemes are needed to achieve the far-field responses. Many schemes of transforming zone of fields with FDTD method are proposed [27]-[30]. In this section, two standard schemes of near field to far field (NFFF) transformation are introduced. The first one is called “Frequency-Domain Near-Field to Far-Field Transformation (FD-NFFF)”, which is usually useful for obtaining the single-frequency radiation patterns. While the antenna gain (broadband) and time-dependent radiation patterns are frequently obtained by another scheme that is called “Time-Domain Near-Field to Far-Field Transformation (TD-NFFF)”. However, these two schemes are based on the same basic idea about zone transformation to achieve far-field response.

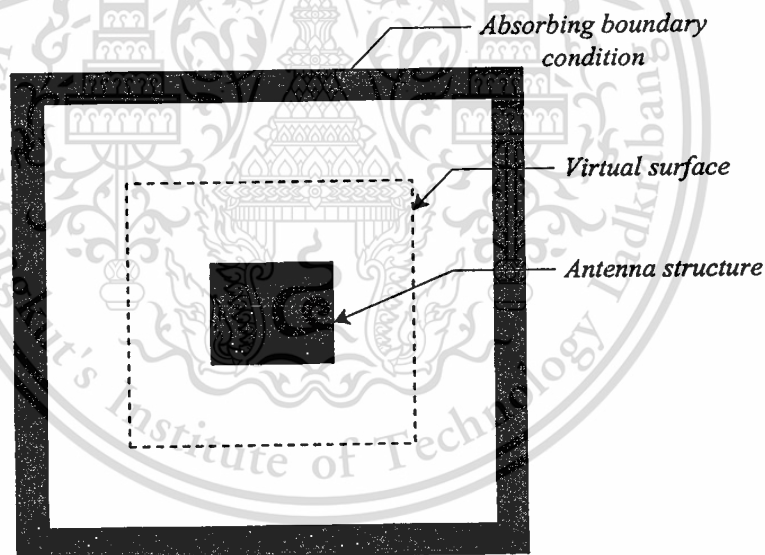


Fig. 2.8 Geometry of the problem with zone transformation

The geometry of the problem that implements the zone of field transformation to obtain the far-field response, specifically for transmitting antenna, can be shown in Fig. 2.8. From the figure, the antenna is enclosed by a virtual surface (transformation surface) and an absorbing boundary condition. The virtual surface is placed between the antenna and the absorbing boundary condition, and encloses entire of the antenna structure. The transformation is performed on the virtual surface by transforming the near-field data on

the virtual surface to obtain the far-field results. In Fig. 2.9, the basic principle of the zone transformation over the virtual surface is illustrated and described below.

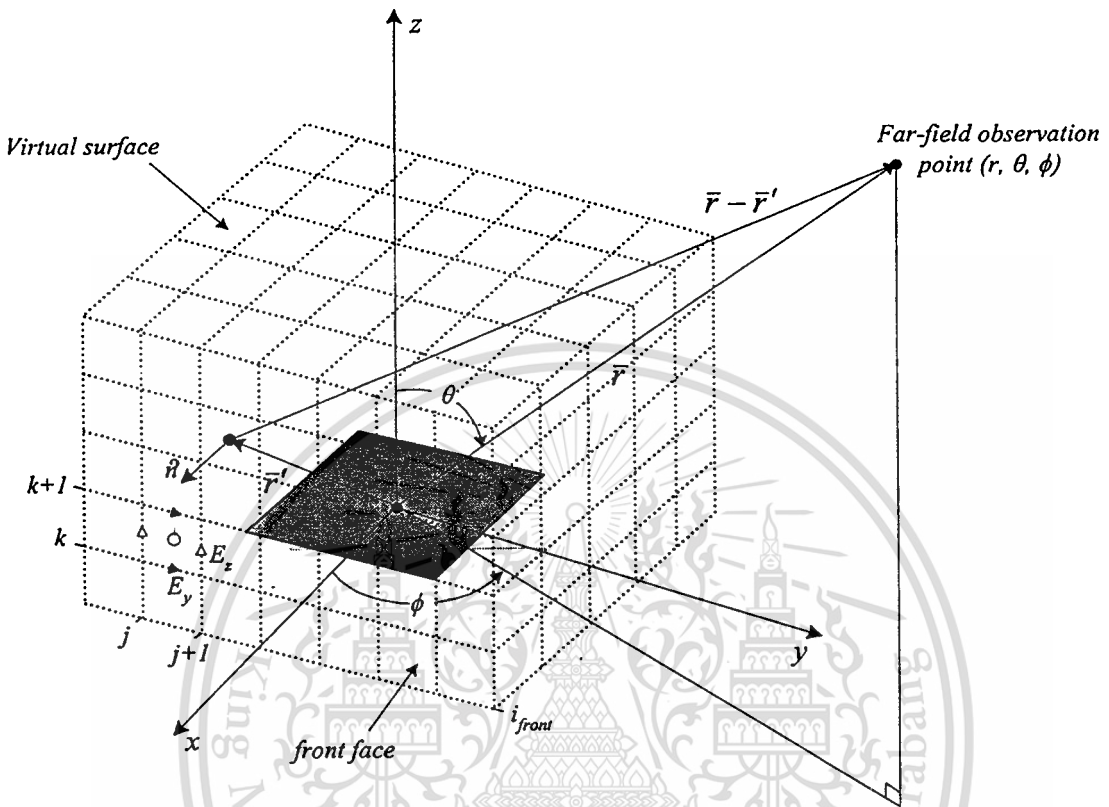


Fig. 2.9 Zone transformation over the virtual surface

From Fig. 2.9, \vec{r}' is the vector originated at the reference point to a near-field source point (a point on the virtual surface) where having the unit outward normal vector \hat{n} . \vec{r} is the vector started from the reference point to a far-field observation point, (r, θ, ϕ) , with distance r . The distance between the near-field source point and the far-field observation point, $|\vec{r} - \vec{r}'|$, causes a delay time that waves use to reach the far-field observation point. The delay time is $|\vec{r} - \vec{r}'|/c$, where c is the speed of light. In order to, transform fields on the virtual surface to far-field observation point, all of near-field source points (each surface patch) are integrated over the entire virtual surface for each far-field observation point (r, θ, ϕ) . By this method, the far-field response at far-zone points of interest, such as radiation patterns, can be obtained.

As the aforementioned, the two near-field to far-field transformation schemes are based on this method, however, for the different purposes, they have some different procedures in computations.

2.4.1 Frequency-domain near-field to far-field transformation

The FD-NFFF transformation is based on the frequency-domain of analytic form of Huygens' principle:

$$\bar{E}'(\bar{r}, \omega) = \frac{j\omega\mu_o}{4\pi r} \iint_S \left\{ \hat{r} \times \hat{r} \times [\hat{n} \times \bar{H}(\bar{r}', \omega)] - \frac{1}{\eta_o} \hat{r} \times [\hat{n} \times \bar{E}(\bar{r}', \omega)] \right\} \times \exp(-j\omega t_{delay}) dS', \quad (2.32)$$

where the delay time, t_{delay} , is defined as

$$t_{delay} = \frac{r - \hat{r} \cdot \bar{r}'}{c}.$$

The surface integral in (2.32) can be approximated by summations of the fields at the center of the surface of the patches. The electric and magnetic fields are crossed with a unit vector, \hat{n} , to leave only the tangential field components on the virtual surface for the transformation. Subsequently, the tangential field components of electric and magnetic fields at the center of each surface patch must be computed by averaging the nearest field components.

For example, consider the surface patch on the front face denoted by a circle in Fig. 2.9. The tangential components of electric field at the center of the patch (i_{front}, j, k) are found from the average of two neighboring values:

$$E_y|_{i_{front}, j+1/2, k+1/2}^{n+1} = 0.5 \cdot \left(E_y|_{i_{front}, j+1/2, k}^{n+1} + E_y|_{i_{front}, j+1/2, k+1}^{n+1} \right) \quad (2.33a)$$

$$E_z|_{i_{front}, j+1/2, k+1/2}^{n+1} = 0.5 \cdot \left(E_z|_{i_{front}, j, k+1/2}^{n+1} + E_z|_{i_{front}, j+1, k+1/2}^{n+1} \right). \quad (2.33b)$$

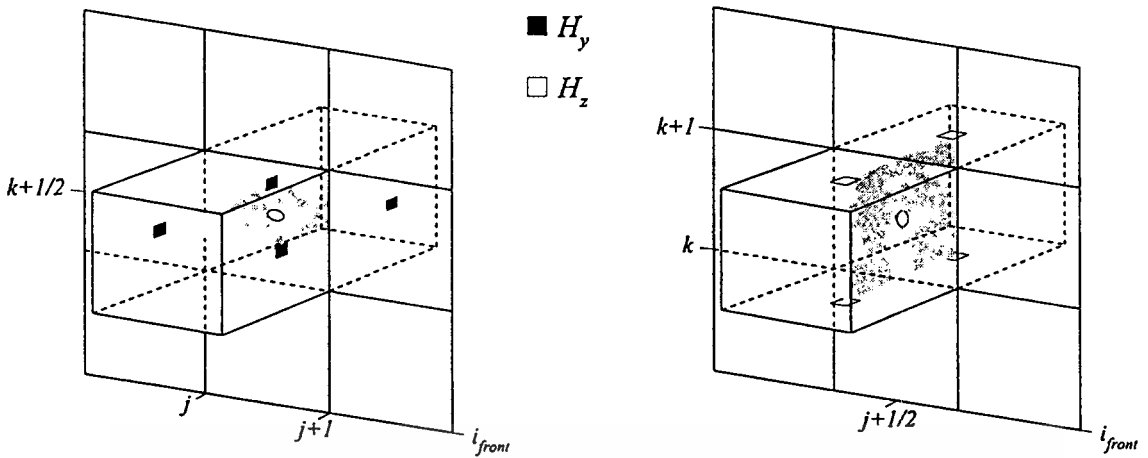


Fig. 2.10 The average of the four neighboring values for magnetic field

Moreover, as illustrated in Fig. 2.10, the tangential components of the magnetic field at the center of the patch are found from the average of the four neighboring values:

$$H_y \Big|_{i_{front}, j+1/2, k+1/2}^{n+1/2} = 0.25 \cdot \left(\begin{array}{l} H_y \Big|_{i_{front}+1/2, j+1, k+1/2}^{n+1/2} + H_y \Big|_{i_{front}+1/2, j, k+1/2}^{n+1/2} + \\ H_y \Big|_{i_{front}-1/2, j+1, k+1/2}^{n+1/2} + H_y \Big|_{i_{front}-1/2, j, k+1/2}^{n+1/2} \end{array} \right) \quad (2.34a)$$

$$H_z \Big|_{i_{front}, j+1/2, k+1/2}^{n+1/2} = 0.25 \cdot \left(\begin{array}{l} H_z \Big|_{i_{front}+1/2, j+1/2, k+1}^{n+1/2} + H_z \Big|_{i_{front}+1/2, j+1/2, k}^{n+1/2} + \\ H_z \Big|_{i_{front}-1/2, j+1/2, k+1}^{n+1/2} + H_z \Big|_{i_{front}-1/2, j+1/2, k}^{n+1/2} \end{array} \right) \quad (2.34b)$$

Since the vector product of $(\hat{n} \times \vec{H})$ and $(\hat{n} \times \vec{E})$ are in rectangular coordinates, so the rectangular-to-spherical coordinate transformation is performed. The relation between spherical and rectangular components,

$$\begin{pmatrix} A_x \\ A_y \\ A_z \end{pmatrix} = \begin{pmatrix} \sin \theta \cos \phi & \cos \theta \cos \phi & -\sin \phi \\ \sin \theta \sin \phi & \cos \theta \sin \phi & \cos \phi \\ \cos \theta & -\sin \theta & 0 \end{pmatrix} \begin{pmatrix} A_r \\ A_\theta \\ A_\phi \end{pmatrix}, \quad (2.35)$$

is used. Considering, the outward unit vector normal to the front face is $\hat{n} = \hat{x}$, the result of vector products in (2.32) are

$$\hat{r} \times \hat{r} \times (\hat{n} \times \bar{H}) = -(H_x \sin \theta + H_z \cos \theta \cos \phi) \hat{\theta} + (H_z \sin \phi) \hat{\phi}, \quad (2.36a)$$

$$\hat{r} \times (\hat{n} \times \bar{E}) = (E_z \sin \phi) \hat{\theta} + (E_x \sin \theta + E_z \cos \theta \cos \phi) \hat{\phi}. \quad (2.36b)$$

Note that the field in the far zone contains only $\hat{\theta}$ and $\hat{\phi}$ components. The contribution from this surface (*front face*) is

$$E_{\theta}^r(\bar{r}, \omega) = \frac{j\omega\mu_o\Delta y\Delta z}{4\pi r} \sum_{\text{front face}} \left(H_y \sin \theta + H_z \cos \theta \sin \phi - \frac{E_z \cos \phi}{\eta_o} \right) \times \exp(-j\omega t_{\text{delay}}) \quad (2.37a)$$

$$E_{\phi}^r(\bar{r}, \omega) = \frac{j\omega\mu_o\Delta y\Delta z}{4\pi r} \sum_{\text{front face}} \left(H_z \cos \phi + \frac{E_y \sin \theta}{\eta_o} + \frac{E_z \cos \theta \sin \phi}{\eta_o} \right) \times \exp(-j\omega t_{\text{delay}}), \quad (2.37b)$$

where the time delay, t_{delay} , changes from patch to patch. By the same manner, the contributions from the other five faces of the virtual surface can be given as follows:

back face ($\hat{n} = -\hat{x}$);

$$E_{\theta}^r(\bar{r}, \omega) = \frac{j\omega\mu_o\Delta y\Delta z}{4\pi r} \sum_{\text{back face}} \left(-H_y \sin \theta - H_z \cos \theta \sin \phi + \frac{E_z \cos \phi}{\eta_o} \right) \times \exp(-j\omega t_{\text{delay}}) \quad (2.38a)$$

$$E_{\phi}^r(\bar{r}, \omega) = \frac{j\omega\mu_o\Delta y\Delta z}{4\pi r} \sum_{\text{back face}} \left(-H_z \cos \phi - \frac{E_y \sin \theta}{\eta_o} - \frac{E_z \cos \theta \sin \phi}{\eta_o} \right) \times \exp(-j\omega t_{\text{delay}}) \quad (2.38b)$$

right face ($\hat{n} = \hat{y}$);

$$E_{\theta}^r(\bar{r}, \omega) = \frac{j\omega\mu_o\Delta x\Delta z}{4\pi r} \sum_{\text{right face}} \left(-H_x \sin\theta - H_z \cos\theta \cos\phi - \frac{E_z \sin\phi}{\eta_o} \right) \times \exp(-j\omega t_{\text{delay}}) \quad (2.39a)$$

$$E_{\phi}^r(\bar{r}, \omega) = \frac{j\omega\mu_o\Delta x\Delta z}{4\pi r} \sum_{\text{right face}} \left(H_z \sin\phi - \frac{E_x \sin\theta}{\eta_o} - \frac{E_z \cos\theta \cos\phi}{\eta_o} \right) \times \exp(-j\omega t_{\text{delay}}) \quad (2.39b)$$

left face ($\hat{n} = -\hat{y}$);

$$E_{\theta}^l(\bar{r}, \omega) = \frac{j\omega\mu_o\Delta x\Delta z}{4\pi r} \sum_{\text{left face}} \left(H_x \sin\theta + H_z \cos\theta \cos\phi + \frac{E_z \sin\phi}{\eta_o} \right) \times \exp(-j\omega t_{\text{delay}}) \quad (2.40a)$$

$$E_{\phi}^l(\bar{r}, \omega) = \frac{j\omega\mu_o\Delta x\Delta z}{4\pi r} \sum_{\text{right face}} \left(-H_z \sin\phi + \frac{E_x \sin\theta}{\eta_o} + \frac{E_z \cos\theta \cos\phi}{\eta_o} \right) \times \exp(-j\omega t_{\text{delay}}) \quad (2.40b)$$

upper face ($\hat{n} = \hat{z}$);

$$E_{\theta}^u(\bar{r}, \omega) = \frac{j\omega\mu_o\Delta x\Delta y}{4\pi r} \sum_{\text{upper face}} \left(-H_x \cos\theta \sin\phi + H_y \cos\theta \cos\phi + \frac{E_x \cos\phi}{\eta_o} + \frac{E_y \sin\phi}{\eta_o} \right) \times \exp(-j\omega t_{\text{delay}}) \quad (2.41a)$$

$$E_{\phi}^u(\bar{r}, \omega) = \frac{j\omega\mu_o\Delta x\Delta y}{4\pi r} \sum_{\text{upper face}} \left(-H_x \cos\phi - H_y \sin\phi - \frac{E_x \cos\theta \sin\phi}{\eta_o} + \frac{E_y \cos\theta \cos\phi}{\eta_o} \right) \times \exp(-j\omega t_{\text{delay}}) \quad (2.41b)$$

This material is reserved for educational use only, not allowed for commercial use.

Forbidden to modify the content, and cite the document when use.

lower face ($\hat{n} = -\hat{z}$);

$$E_{\theta}'(\bar{r}, \omega) = \frac{j\omega\mu_o\Delta x\Delta y}{4\pi r} \sum_{\text{lower face}} \left(H_x \cos\theta \sin\phi - H_y \cos\theta \cos\phi - \frac{E_x \cos\phi}{\eta_o} - \frac{E_y \sin\phi}{\eta_o} \right) \times \exp(-j\omega t_{\text{delay}}) \quad (2.42a)$$

$$E_{\phi}'(\bar{r}, \omega) = \frac{j\omega\mu_o\Delta x\Delta y}{4\pi r} \sum_{\text{lower face}} \left(H_x \cos\phi + H_y \sin\phi + \frac{E_x \cos\theta \sin\phi}{\eta_o} - \frac{E_y \cos\theta \cos\phi}{\eta_o} \right) \times \exp(-j\omega t_{\text{delay}}) \quad (2.42b)$$

Due to the field components must be in frequency-domain, thus the Discrete Fourier Transformation (DFT) is used to transform all field components in time-domain to be in frequency-domain. The DFT is given by

$$U(\bar{r}, \omega) = \sum_{n=1}^N U|_{\bar{r}}^n \exp(-j\omega n\Delta t) \quad (2.43)$$

where U represents any field components, N is a maximum number of time steps. The postprocessing approach for implementing (2.43) involves storing at every time step the tangential field components for every surface patches. The storage of the full time history of the tangential field components at every surface patch requires a prohibitively large amount of storage. For example, if there are M surface patches on the entire virtual surface (each containing four tangential field components), the required amount of storage is about $4MN$ (real numbers) per transformation frequency. In some cases, a large number of N is needed to make the FDTD simulation reach its steady-state, then the storage space may be excessive. Hence, it is impractical to compute the frequency-domain fields using the Fourier transformation at the conclusion of the FDTD time stepping. Alternatively, the concurrent-processing approach in which (2.43) is implemented “on-the-fly” in step with the FDTD calculation using a running-sum implementation of the DFT. In the running-sum implementation, the update relation for time step, n , is

$$U(\bar{r}, \omega)|_{new} = U(\bar{r}, \omega)|_{previous} + U|_{\bar{r}}^n \exp(-j\omega n\Delta t). \quad (2.44)$$

By using this method, the summation is updated at every time step and stored back to the same variable, $U(\bar{r}, \omega)$. Therefore, the amount of the storage can be reduced to be about only $4M$ (complex numbers) or $8M$ (real numbers).

In practice, the running-sum DFTs are computed during the FDTD calculation and stored for postprocessing. During postprocessing, the radiated fields (E_θ^r, E_ϕ^r) are computed by using (2.37) through (2.42) with the stored frequency-domain tangential field components and the radiation pattern can be obtained by summing up the radiated fields contributed from the virtual surfaces.

2.4.2 Time-domain near-field to far-field transformation

The TD-NFFF transformation is based on the time-domain of Huygens' principle, which is time-domain counterpart of (2.32):

$$\bar{E}^r(\bar{r}, t) = \frac{\mu_0}{4\pi r} \oint_S \left\{ \hat{r} \times \hat{r} \times \frac{\partial}{\partial t'} [\hat{n} \times \bar{H}(\bar{r}', t')] - \frac{1}{\eta_0} \hat{r} \times \frac{\partial}{\partial t'} [\hat{n} \times \bar{E}(\bar{r}', t')] \right\}_{t'=t_r} dS' \quad (2.45)$$

where the retarded time, t_r , is

$$t_r = t - \frac{r - \hat{r} \cdot \bar{r}'}{c} = t - t_{delay}.$$

To illustrate the derivation of the TD-NFFF, the same surface used for the FD-NFFF transformation is used for the TD-NFFF transformation. Thus, the contribution from this surface is

$$E_\theta^r(\bar{r}, t) = \frac{\mu_0 \Delta y \Delta z}{4\pi r} \sum_{front\ face} \left(\sin \theta \frac{\partial H_y}{\partial t'} + \cos \theta \sin \phi \frac{\partial H_z}{\partial t'} - \frac{\cos \phi}{\eta_0} \frac{\partial E_z}{\partial t'} \right)_{t'=t_r} \quad (2.46a)$$

$$E_\phi^r(\bar{r}, t) = \frac{\mu_0 \Delta y \Delta z}{4\pi r} \sum_{front\ face} \left(\cos \phi \frac{\partial H_z}{\partial t'} + \frac{\sin \theta}{\eta_0} \frac{\partial E_y}{\partial t'} + \frac{\cos \theta \sin \phi}{\eta_0} \frac{\partial E_z}{\partial t'} \right)_{t'=t_r}. \quad (2.46b)$$

This material is reserved for educational use only, not allowed for commercial use.

Forbidden to modify the content, and cite the document when use.

As discussed previously, the postprocessing approach for implementing (2.43) and (2.44) requires a prohibitively large amount of storage for storing the full time history of the tangential field components at every surface patch. Therefore, the concurrent-processing approach is considered.

In the concurrent-processing approach, (2.46a) is rewritten as

$$rE_{\theta}^r(\vec{r}, t) = \frac{\mu_o}{4\pi} \left(\frac{\partial}{\partial t} \psi_{\theta}^H + \frac{1}{\eta_o} \frac{\partial}{\partial t} \psi_{\theta}^E \right) \quad (2.47)$$

with the new variables $\psi_{\theta}^H(t)$ and $\psi_{\theta}^E(t)$ given by

$$\psi_{\theta}^H(t) = \Delta y \Delta z \sum_{\text{front face}} \left[\sin \theta \cdot H_y(t - t_{\text{delay}}) + \cos \theta \sin \phi \cdot H_z(t - t_{\text{delay}}) \right], \quad (2.48a)$$

$$\psi_{\theta}^E(t) = \Delta y \Delta z \sum_{\text{front face}} \left[-\cos \phi \cdot E_z(t - t_{\text{delay}}) \right]. \quad (2.48b)$$

During the FDTD time stepping, $\psi_{\theta}^H(t)$ and $\psi_{\theta}^E(t)$ are computed incrementally at each time step. Consider the contribution to (2.48b) from a single surface patch on the right face (i_{front}, j, k). Because the field components in the FDTD simulation are only known at discrete time levels, the time retardation requires temporal interpolation. Applying linear interpolation, the function $\psi_{\theta}^E(t)$ at time step n can be obtained as

$$\psi_{\theta}^E \Big|_n = -\cos \phi \Delta y \Delta z \left\{ \begin{aligned} & \left[1 - q_{\text{front}}^E(j, k) \right] E_z \Big|_{i_{\text{front}}, j+1/2, k+1/2}^{n-n_{\text{front}}^E(j, k)} \\ & + \left[q_{\text{front}}^E(j, k) \right] E_z \Big|_{i_{\text{front}}, j+1/2, k+1/2}^{n-n_{\text{front}}^E(j, k)+1} \end{aligned} \right\}, \quad (2.49)$$

$$\text{where} \quad n_{\text{front}}^E(j, k) = \text{int} \left[t_{\text{delay}}(i_{\text{front}}, j, k) / \Delta t \right], \quad (2.50a)$$

$$q_{\text{front}}^E(j, k) = \left[t_{\text{delay}}(i_{\text{front}}, j, k) / \Delta t \right] - \text{int} \left[t_{\text{delay}}(i_{\text{front}}, j, k) / \Delta t \right], \quad (2.50b)$$

Hence, in the concurrent-processing approach, (2.49) is rewritten as

$$\psi_{\theta}^E \Big|_{new}^{n+n_{front}^E} = \psi_{\theta}^E \Big|_{previous}^{n+n_{front}^E} - \Delta y \Delta z \cos \theta [q_{front}^E(j, k)] E_z \Big|_{i_{front}, j+1/2, k+1/2}^n, \quad (2.51a)$$

$$\psi_{\theta}^E \Big|_{new}^{n+n_{front}^E+1} = \psi_{\theta}^E \Big|_{previous}^{n+n_{front}^E+1} - \Delta y \Delta z \cos \theta [1 - q_{front}^E(j, k)] E_z \Big|_{i_{front}, j+1/2, k+1/2}^n. \quad (2.51b)$$

Note that (2.51a) and (2.51b) are updated relations for each surface patch. The incremental computation of $\psi_{\theta}^H(t)$ is similar to that for $\psi_{\theta}^E(t)$.

At the conclusion of the FDTD time stepping, the far field is simply computed from a discretized form of (2.52), that is

$$rE_{\theta}^r \Big|_{\bar{r}}^n = \frac{\mu_o}{4\pi\Delta t} \left[\left(\psi_{\theta}^H \Big|^{n+1} - \psi_{\theta}^H \Big|^n \right) + \frac{1}{\eta_o} \left(\psi_{\theta}^E \Big|^{n+1} - \psi_{\theta}^E \Big|^n \right) \right]. \quad (2.52)$$

This equation and the similar one for $rE_{\phi}^r \Big|_{\bar{r}}^n$ give the far field response in the time domain.

2.5 Conclusions

In this chapter, the basic elements for the FDTD analysis of a transmitting antenna, which is composed of the FDTD formulations, PML absorbing boundary condition, antenna excitation and feed models, and near-field to far-field transformations, are provided.

The standard FDTD algorithm is directly derived from Maxwell's equations in differential form. The finite-difference schemes are applied with the position of field components on the grid cell as shown in Fig. 2.2 to approximate the differential equations (to approximate the space and time derivatives). That gives the FDTD equations for updating the magnetic and electric fields in time-domain. For determination of the stable region in FDTD calculation, the stability criterion in rectangular coordinates is presented.

For the analysis of an antenna that is the radiation problem, an absorbing boundary condition is needed to truncate the solution region. The PML absorbing boundary condition is introduced for this purpose. The PML approach is based on a splitting of electric or magnetic field components in the absorbing boundary region with the possibility of assigning losses to the individual split field components. To illustrate the PML approach, the problem concerns with the wave propagation in TE case is

presented, and the FDTD equations with exponential time-stepping is used to update the field components inside PML regions.

For the antenna excitation, the implementation of antenna excitation depends on the particular application. It should be selected to be suitable for the analysis of antenna. It means that, if the antenna is analyzed at a single frequency f_0 , the sinusoidal wave of frequency f_0 can be used as the antenna excitation. While the antenna is analyzed over a band of frequencies, it is efficient to excite the antenna with a Gaussian pulse. For the antenna feeding, especially, the coaxial probe feed can be accomplished by various models, i.e., delta-gap feed, magnetic-frill and the full model with coaxial line model.

Finally, the far-field responses can be obtained by the near-field to far-field transformation. The transformation is performed on the virtual surface, which is placed between the antenna and an absorbing boundary condition. The two standard schemes of near-field to far-field transformations, the frequency-domain near-field to far-field (FD-NFFF) transformation and time-domain near-field to far-field (TD-NFFF) transformation, are presented. The FD-NFFF and TD-NFFF transformations are based on the frequency-domain and time-domain analytic form of Huygens' principle, respectively. These two schemes is useful for different purposes, that is, the FD-NFFF transformation is useful for obtaining the single-frequency radiation patterns, whereas the TD-NFFF transformation gives the far-field responses in time-domain that is useful for obtaining the time-dependent radiation patterns and broadband gain.

CHAPTER 3

A SWITCHED-BEAM FLAT DIVERSITY ANTENNA

Usually, the antenna, especially for mobile communications, is desired to be small, lightweight and low profile. In addition, the diversity antenna is needed to overcome the multipath fading in mobile environment and its effectiveness can be evaluated from how low correlation coefficient can be achieved. A switched-beam flat diversity antenna is proposed to be a pattern diversity antenna for mobile application. It is designed to apply for wireless local area network (WLAN) system as a mobile terminal antenna. The structure of the antenna and FDTD model for antenna analysis are illustrated in this chapter.

3.1 Antenna Configuration

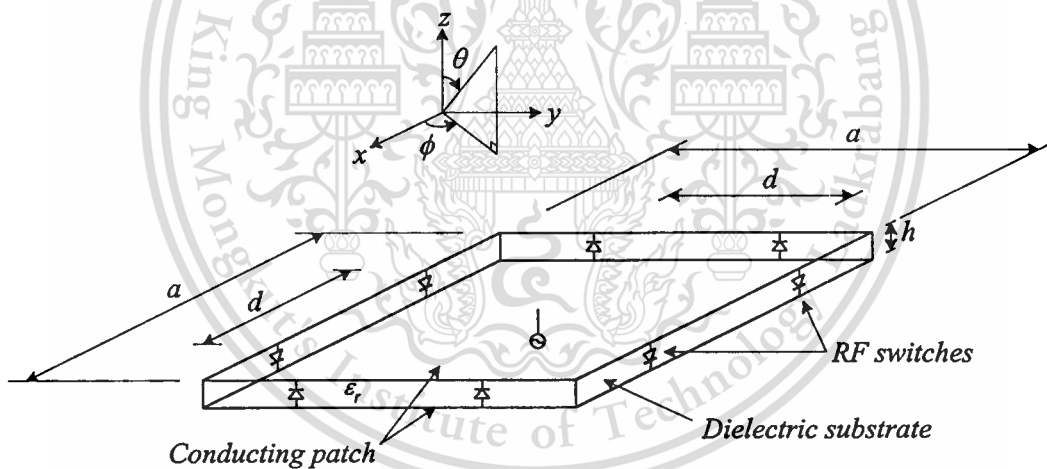


Fig. 3.1 Antenna configuration

The structure of the antenna is based on a center-fed square patch printed antenna with shunting posts at the corners of the patch. From this structure, the fundamental requirements for the mobile antenna, which are small size, lightweight and low profile, can be obtained. Also, in order to apply the diversity technique to this antenna, the beam switching is implemented to achieve the pattern diversity technique. Consequently, the RF switches are installed on each side of the patch, as shown in Fig. 3.1, to switch the beam of the antenna. The beam switching can be done by turn on/off the RF switches. By

This material is reserved for educational use only, not allowed for commercial use.

Forbidden to modify the content, and cite the document when use.

simultaneously turn on the RF switches on left and right sides of the patch and the other switches are turned off, the RF switches on left and right sides of the patch will be short-circuited and radiation on those sides (radiation in y direction) will be suppressed, thus, the beam is radiated in x direction ($\phi = 0^\circ, 180^\circ$). On the other hand, the beam will be switched to y direction ($\phi = 90^\circ, 270^\circ$) by simultaneously turn on the RF switches on front and backsides of the patch to suppress radiation in x direction, and the other switches are turned off. By this method, the beam can be switched to orthogonal directions, so the pattern diversity technique can be approached. However, the diversity performance of this antenna will be obtained when the correlation coefficient between the radiation patterns of the antenna is low.

For antenna analysis, the patch size, a , is specified to be equal to a half wavelength and the space between two RF switches on each side of the patch, d , are varied to find the radiation patterns with the lowest correlation coefficient. By using the FDTD method to compute the radiation patterns of this antenna, the FDTD model used for antenna analysis is presented as below.

3.2 FDTD Model

Due to the antenna is designed to apply for WLAN system at ISM band (2.40 - 2.48 GHz), where the center frequency is at 2.44 GHz, so the patch size is specified to be 61.5 mm which corresponds to a half wavelength at 2.44 GHz. The dielectric substrate is 1.6 mm thick with relative permittivity $\epsilon_r = 2.95$. Then, the knowledge of the FDTD antenna analysis presented in previous chapter is implemented to model and solve the problem.

In order to construct the FDTD model, the problem space including the antenna is quantized by Yee cells. Fig. 3.2 shows the FDTD model with dimensions of the problem space. The cell size is defined as $\Delta x = \Delta y = 0.615$ mm and $\Delta z = 0.4$ mm to fit the dimension of the antenna. Thus, the antenna is modeled by $100 \times 100 \times 4$ cells. The conducting surfaces at upper and lower sides of the patch are assumed as the perfectly electric conductor (PEC) and the tangential field components (E_x and E_y components) on conducting surfaces are set to zero. Also, the shorting posts are model by the PEC wire and the E_z components are set to zero along the wire model. For the RF switch modeling, it is assumed that the turned on and turned off RF switches are ideally short-circuited and open-circuited, respectively. Thus, the turned on RF switch is simply modeled by using

the PEC wire model located at the position of the RF switch, and the wire model will be removed when the RF switch is turned off or open-circuited. Consequently, in computational model, there are four PEC wire models located at the position of the turned on RF switches as shown in Fig. 3.2, and the space between two RF switches on each side of the patch will be changed by varying the number of cells m .

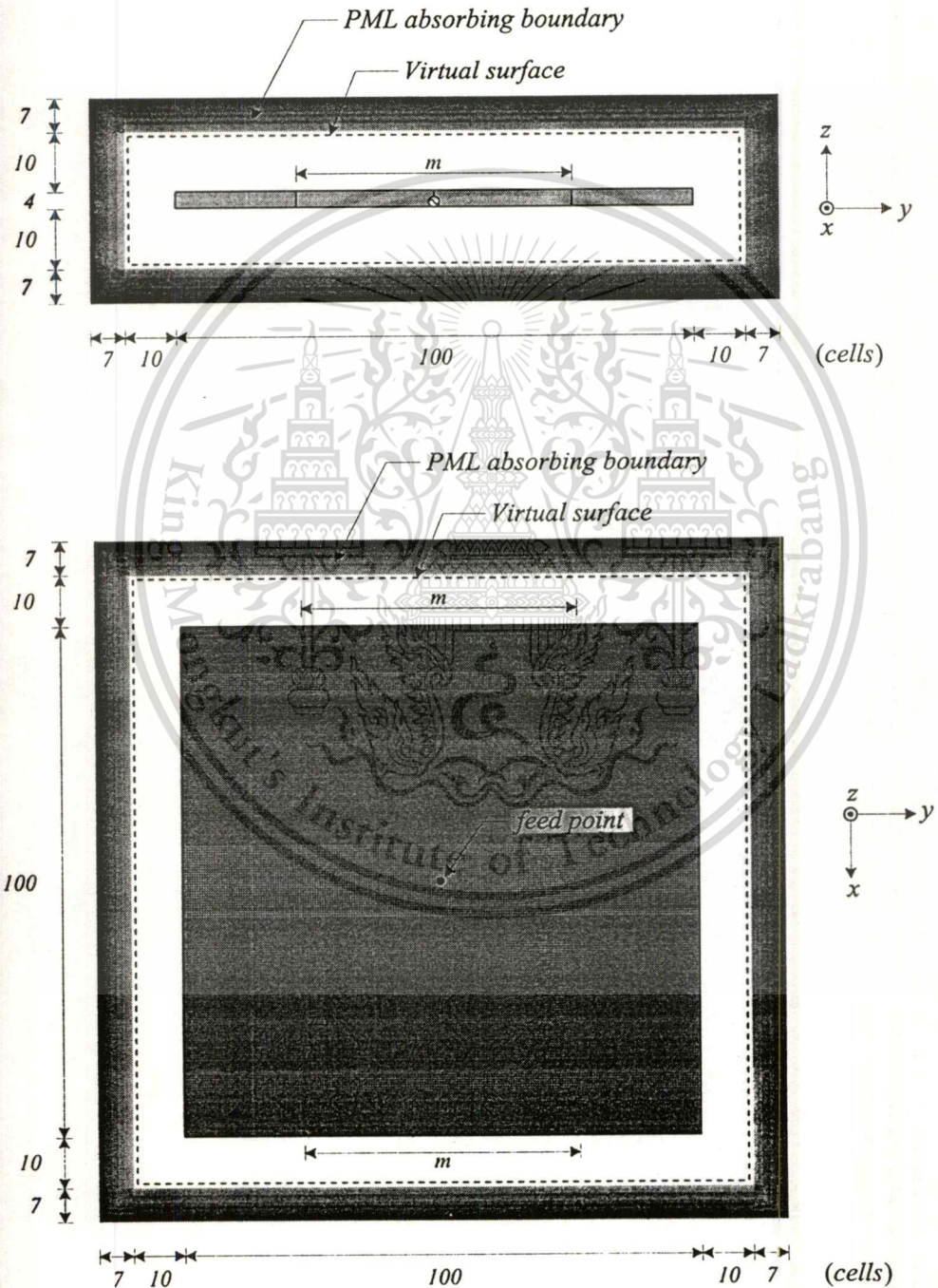


Fig. 3.2 FDTD model and dimensions of the problem space

The problem space is terminated by a PML absorbing boundary with 7 layers ($\delta = 7$ cells), a parabolic profile ($n = 2$) and 1% reflection ($R(0) = 0.01$). This ensures that reflections from the boundary walls are below -40 dB [31]. There are 10 cells between the antenna model and the PML region in each direction of the axis coordinates. Consequently, the numbers of cells are 134 in x direction, 134 in y direction and 38 in z direction.

To obtain the far-field responses, the virtual surfaces or transformation surfaces are placed between the antenna and PML absorbing boundary. Each surface is placed in the distance of 8 cells from the outer boundary in each direction of the axis coordinates to enclose entire antenna model.

Since the symmetry of the antenna and the symmetry of the excitation, the computational space can be reduced to a half of the problem space. The perfectly magnetic conductor (PMC) image plane with respect to xz plane is used to reduce the computational space by using the relationships between the field components at PMC image plane as illustrated in Fig. 3.3 [23]. Thus, the numbers of cells in computational space are reduced to 134 in x direction, 67 in y direction and 38 in z direction.

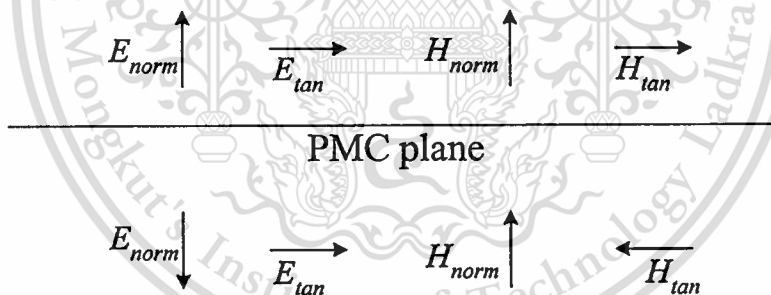


Fig. 3.3 Relationships for field components at the PMC image plane

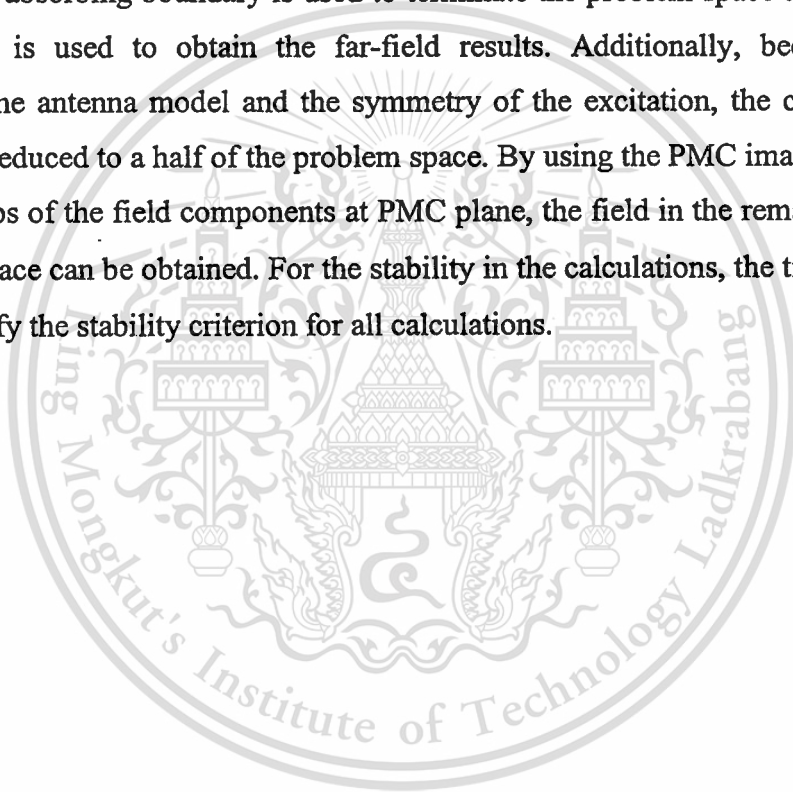
For antenna feeding, the delta gap feed model described in Section 2.3.2 is applied and the sinusoidal voltage excitation at single frequency of 2.44 GHz is used. According to the stability criterion, the time step of $\Delta t = 9.80469 \times 10^{-13}$ seconds, which is slightly lower than the upper limit of stability criterion, is used for all calculations.

3.3 Conclusions

A switched-beam flat diversity antenna is presented. It is proposed to apply as a mobile terminal antenna for WLAN system at ISM band. The structure of antenna is a

center-fed half wavelength square printed antenna, which can give the fundamental requirements for mobile antenna. In order to perform as a diversity antenna, the pattern diversity technique is applied to this antenna that can be performed by switch beam of the antenna. By installing the RF switches on each side of the antenna to control beam of the antenna to be directed in x direction ($\phi = 0^\circ, 180^\circ$) or y direction ($\phi = 90^\circ, 270^\circ$).

In calculations, the model of the antenna is established for analysis by FDTD method. The problem space is discretized by Yee cells and the cell size is restricted to fit to the dimensions of the antenna. In order to compute the far-field patterns of the antenna, the sinusoidal voltage excitation with a delta-gap feed is used to excite the antenna as well as a PML absorbing boundary is used to terminate the problem space and the NFFF transformation is used to obtain the far-field results. Additionally, because of the symmetry of the antenna model and the symmetry of the excitation, the computational region can be reduced to a half of the problem space. By using the PMC image plane with the relationships of the field components at PMC plane, the field in the remainder part of the problem space can be obtained. For the stability in the calculations, the time step Δt is chosen to satisfy the stability criterion for all calculations.



CHAPTER 4

RADIATION CHARACTERISTICS OF THE ANTENNA

Since the pattern diversity antenna is proposed in this thesis, hence low correlation coefficient between two patterns of the antenna is desirable. It is expected to be achieved by using appropriate spacing d between two RF switches on each side of the antenna. In addition, the appropriate radiation characteristics of the antenna such as radiation patterns and directivity must be accomplished. This chapter investigates radiation characteristics as a function of spacing d between two RF switches on each side of the antenna by using FDTD method with the FDTD model presented in the previous chapter. Furthermore, the radiation patterns and directivity of the antenna with and without the shorting posts are compared to know whether the shorting posts is necessary or not.

4.1 Radiation Patterns

Firstly, the radiation patterns of the antenna with single RF switch on each side of the antenna are investigated. The results have been shown in Fig. 4.1. As the results, the radiation in undesired direction is slightly suppressed that will give the high correlation coefficient, which is unsatisfied for diversity antenna. Therefore, more than one RF switch is needed. However, for cost-effective, only two RF switches are used.

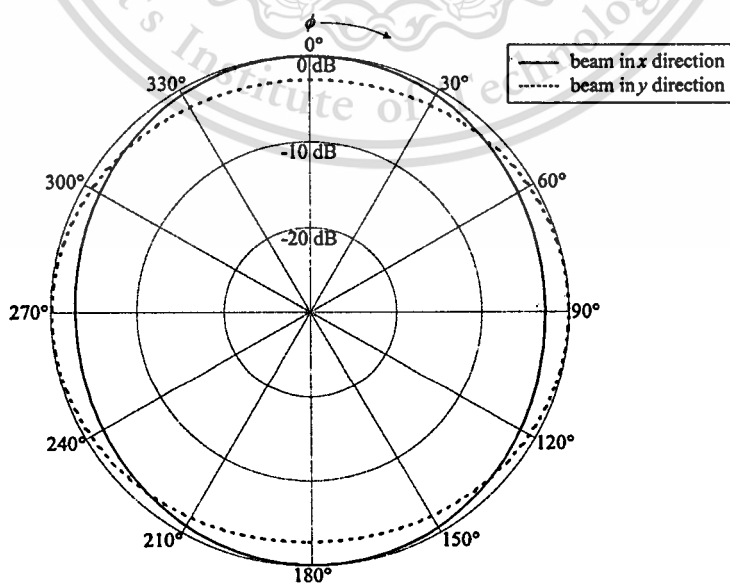


Fig. 4.1 Radiation patterns of the antenna with single RF switch on each side of the antenna

Two RF switches are installed on each side of the antenna, and the radiation patterns of the antenna are investigated. By using the FDTD method, the radiation pattern of the antenna with sinusoidal excitation is calculated, therefore, the numbers of time step are needed to reach the sinusoidal steady-state and obtain the stable results. Fig. 4.2 shows the comparative result of the radiation patterns with various time duration. The results are compared with the ninth period calculated radiation pattern, which provided the reasonable results [32].

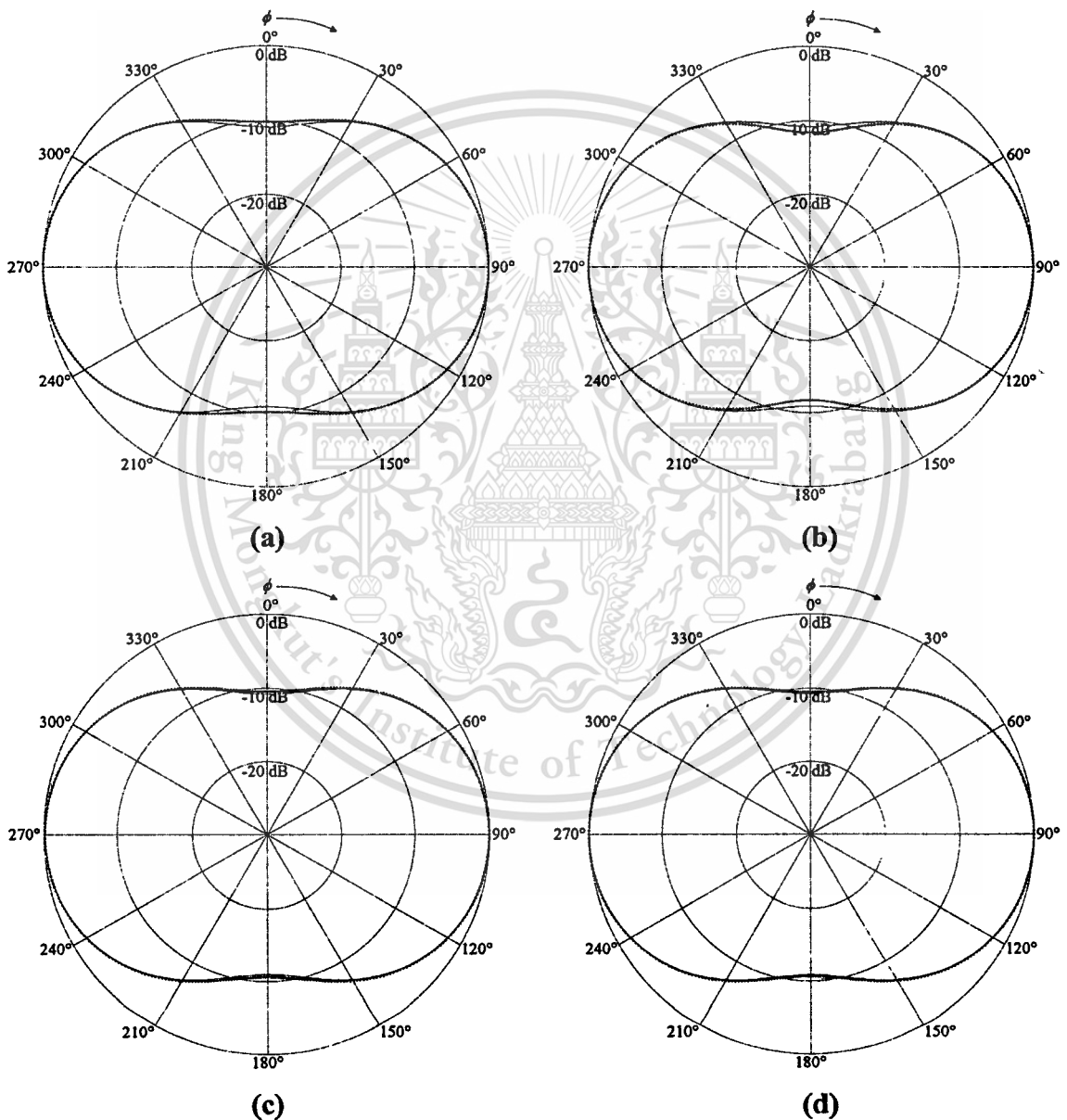


Fig. 4.2 Comparative results of the radiation pattern from the ninth period data (solid line) and the radiation pattern from various period data (dot line)
(a) second period, **(b)** third period, **(c)** seventh period, **(d)** eighth period

This material is reserved for educational use only, not allowed for commercial use.

Forbidden to modify the content, and cite the document when use.

In Fig. 4.2, it can be seen that the radiation pattern from the second and third period data differ from the reasonable one, and it is closed to the reasonable one for increasing time periods. That is, the radiation pattern from the seventh and eighth period data is close to the radiation pattern from the ninth period data.

In addition, grid size used for FDTD model is considered. The radiation pattern obtained from the FDTD model using grid size of $\Delta x = \Delta y = 0.615$ mm and $\Delta z = 0.4$ mm, which is presented in Section 3.2, is compare with the radiation pattern obtained from the FDTD model using grid size of $2\Delta x, 2\Delta y, 2\Delta z$ and $4\Delta x, 4\Delta y, 4\Delta z$. The number of time step of 3,762 time steps is used to reach the reasonable result. The result is shown in Fig. 4.3. It is found that the radiation in undesired direction is about 1 dB difference for two times grid size ($2\Delta x, 2\Delta y, 2\Delta z$), and more difference about 3 dB is observed for four times grid size ($4\Delta x, 4\Delta y, 4\Delta z$). Therefore, in this case, larger grid size is used more error is observed.

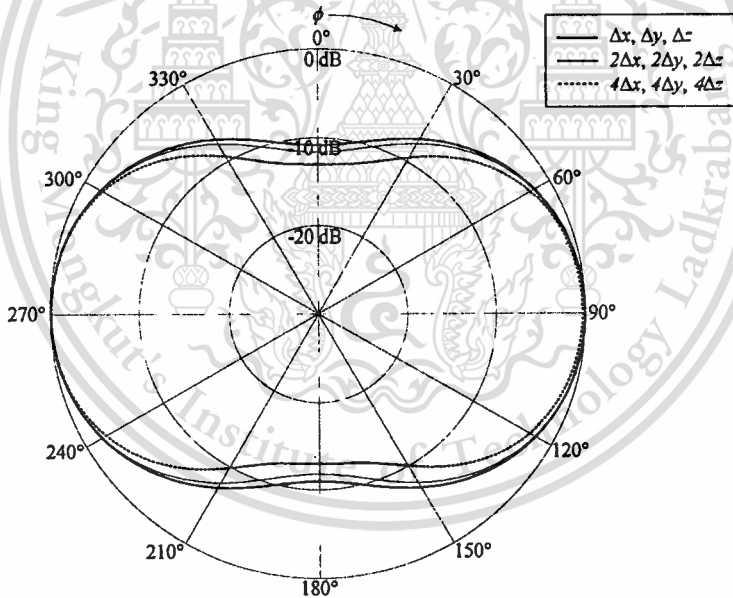


Fig. 4.3 Radiation patterns obtained from FDTD model with various grid size

Consequently, the radiation patterns are computed at the single frequency of 2.44 GHz by using the FDTD model shown in Section 3.2. The FD-NFFF transformation is applied to obtain the far-zone electric field of the antenna. In each computation, the time step of 9.80469×10^{-13} seconds is used for stability. The time duration of 9 periods of the 2.44 GHz sinusoidal excitation, which is equal to 3.688525×10^{-9} seconds and correspond to 3,762 time steps, are used to reach the sinusoidal steady-state and obtain

This material is reserved for educational use only, not allowed for commercial use.

Forbidden to modify the content, and cite the document when use.

the stable results. Fig. 4.4 shows the computed radiation patterns directed in y direction ($\phi = 90^\circ, 270^\circ$) of the antenna for d equals 0.15λ , 0.25λ and 0.35λ . As the results of the radiation pattern in azimuth plane, the radiation in the undesired direction (x direction) is suppressed. It is more suppressed for d equals 0.25λ , as shown in Fig. 4.4(a), and the radiation patterns in elevation plane are the same for different values of d , as shown in Fig. 4.4(b). The results are agree with the results presented in [19] that the antenna is analyzed by Numerical Electromagnetic Code (NEC-2) based on the Method of Moments with wire grid model. However, the wire grid model is unable to model the dielectric substrate, which is modeled as air-filled, therefore the FDTD method is used to analyze the antenna with more practical model.

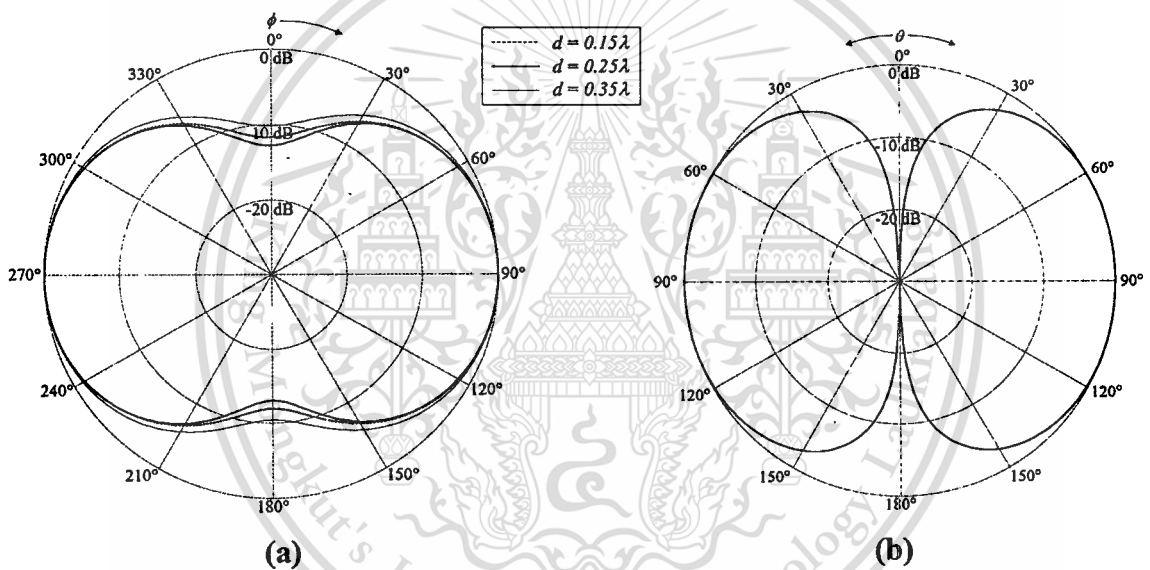


Fig. 4.4 Radiation patterns of the antenna with the shorting posts

(a) Azimuth plane

(b) Elevation plane

In order to compare with the radiation patterns of the antenna with the shorting posts, as shown in Fig. 4.4, the radiation patterns of the antenna without shorting posts for d equals 0.15λ , 0.25λ and 0.35λ are computed and illustrated in Fig. 4.5. It is found that for the radiation pattern in the azimuth plane, the more suppression of radiation in the undesired direction is obtained when d equals 0.25λ , as shown in Fig. 4.5(a), but it is less than that for the antenna with shorting posts. For the radiation pattern in elevation plane, the radiation patterns are the same for the antenna with and without shorting posts, as shown in Fig. 4.4(b) and 4.5(b).

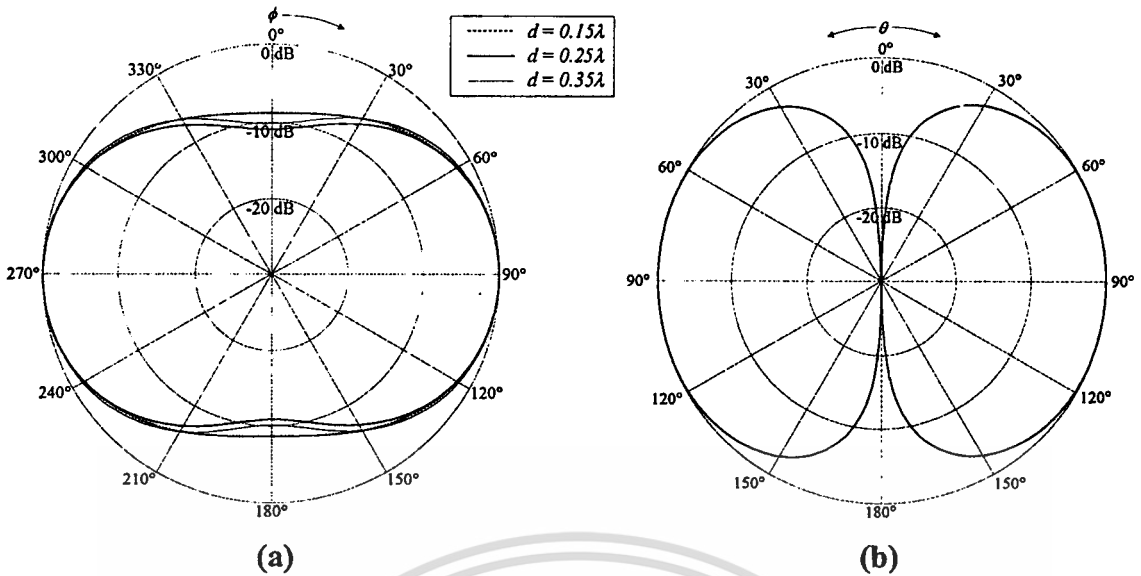


Fig. 4.5 Radiation patterns of the antenna without the shorting posts

(a) Azimuth plane

(b) Elevation plane

Since the incident waves are assumed to be concentrated in horizontal plane in practical use [33], the radiation patterns in the azimuth plane of the antenna are considered. Furthermore, the radiation patterns with low correlation coefficient are required for diversity antenna, however, it is found that the radiation pattern with more suppression of radiation in the undesired direction can provide the lower correlation coefficient [19]. The correlation coefficient of the antenna, which is calculated from the radiation pattern in the azimuth plane, will be investigated and presented in the next chapter.

Here, the radiation pattern of the antenna with and without shorting posts for d equals 0.25λ are compared. Fig 4.6(a) and 4.6(b) show the radiation pattern directed in x and y directions, respectively. It can be seen that the antenna with shorting posts provides the radiation pattern with more suppression of radiation in the undesired direction than the radiation pattern provided by the antenna without shorting posts. However, the correlation coefficient between the radiation patterns for antenna with and without shorting posts are slightly different for d equals 0.25λ that will be presented in the next chapter. It causes no difference in diversity performance of the antenna with and without shorting posts for d equals 0.25λ . Subsequently, the switched-beam pattern of the antenna is considered. As illustrated in Fig. 4.7, if the beam switching is performed, the radiation

patterns of the antenna with and without shorting posts are the same and close to omnidirectional pattern.

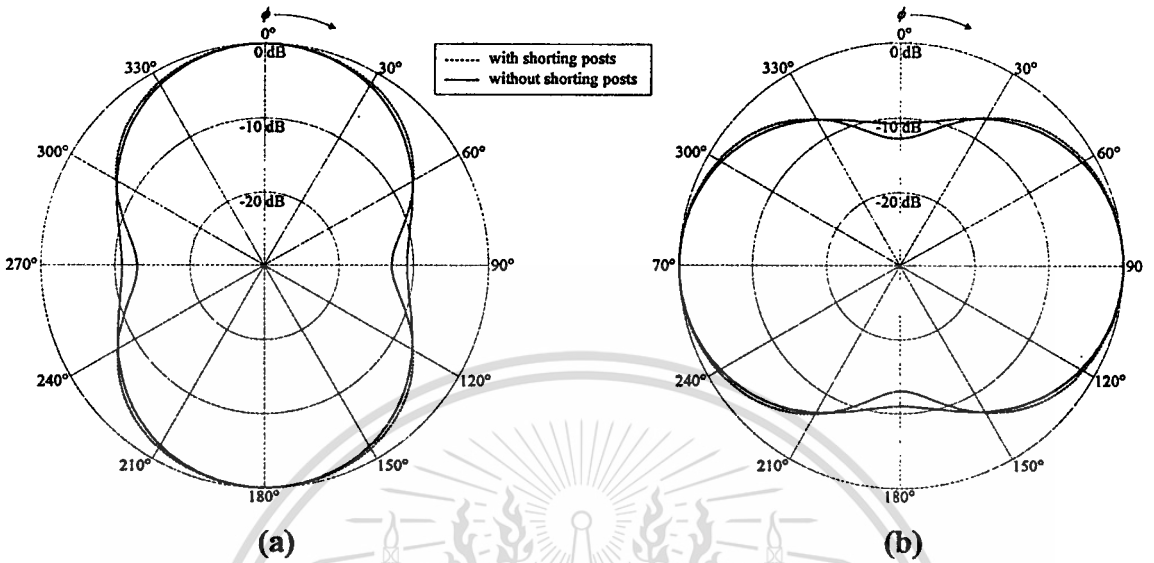


Fig. 4.6 Comparisons of radiation patterns of the antenna with and without shorting posts

(a) x direction

(b) y direction

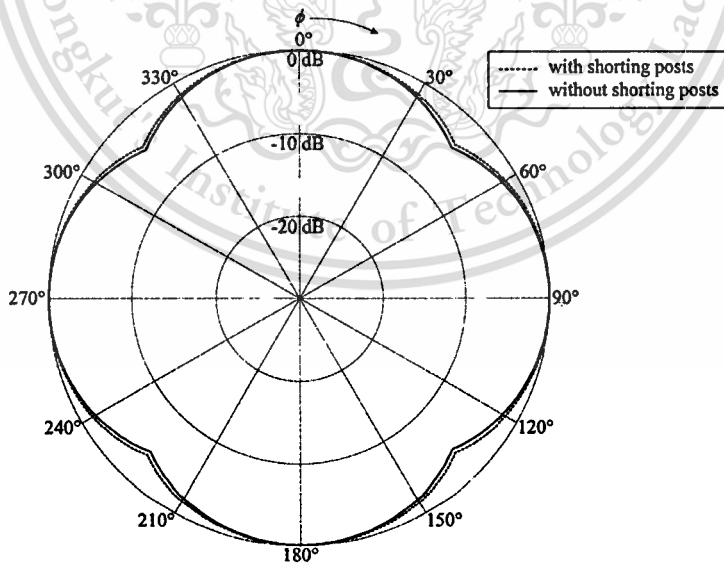


Fig. 4.7 Switched-beam pattern of the antenna

4.2 Directivity

In this section, the directivity of the antenna is investigated as a function of d . The directivity for antenna with and without shorting posts are compared. The higher directivity of the antenna is required to reduce the transmitting power or extend the communication range.

The definition of the directivity is given [34]

$$D = \frac{4\pi U}{P_{rad}}, \quad (4.1)$$

where U is the radiation intensity, which can be approximated from the far-zone electric field of the antenna as

$$U(\theta, \phi) \approx \frac{1}{2\eta} (|E_\theta(\theta, \phi)|^2 + |E_\phi(\theta, \phi)|^2). \quad (4.2)$$

where η is impedance of free space.

If lossless antenna is considered, the radiated power is equal to the input power of the antenna, which is given by

$$P_{in} = \frac{1}{2} \text{Re}[V_{in}(\omega)I_{in}^*(\omega)], \quad (4.3)$$

where $\text{Re}[\cdot]$ takes the real part of the complex expression and the asterisk indicates the complex conjugate. The input voltage $V_{in}(\omega)$ and input current $I_{in}(\omega)$ can be obtained from the complex Fourier transforms of input voltage and input current in time-domain, $V_{in}(t)$ and $I_{in}(t)$, as follow:

$$V_{in}(\omega) + V_{in}(n\Delta t) \times e^{-j\omega n\Delta t} \rightarrow V_{in}(\omega), \quad (4.4)$$

$$I_{in}(\omega) + I_{in}(n\Delta t) \times e^{-j\omega n\Delta t} \rightarrow I_{in}(\omega). \quad (4.5)$$

Therefore, the directivity of the antenna for a lossless antenna relative to an isotropic antenna is given by

$$D(\theta, \phi) = \frac{4\pi(|E_\theta(\theta, \phi)|^2 + |E_\phi(\theta, \phi)|^2)/\eta}{\text{Re}[V_{in}(\omega)I_{in}^*(\omega)]}. \quad (4.6)$$

The far-zone electric field in this equation is obtained from radiation pattern calculation.

By using (4.6), the directivity of the antenna for different values of d can be approximated as shown in Fig. 4.8. As the result, the maximum directivity of the antenna without shorting posts is higher than the maximum directivity of the antenna with shorting posts. The higher directivity can be observed when d is closed to 0.25λ , and then, the directivity of the antenna decreases for increasing value of d . Let us consider the maximum directivity of the antenna for d of 0.25λ , the maximum directivity of the antenna with and without shorting posts are equal to 3.11 and 5.55 dBi, respectively.

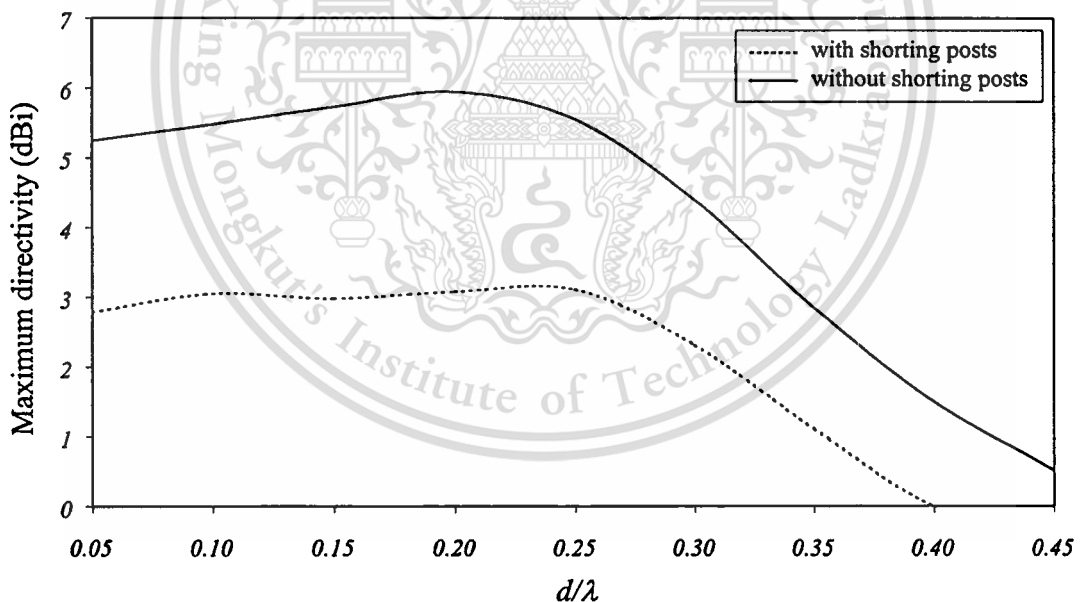


Fig. 4.8 Calculated directivity with respect to d

4.3 Experimental Results

According to the calculated results, it can be concluded that the antenna with two RF switches installed with the spacing of 0.25λ on each side of the antenna, and without the shorting posts at the corners of the antenna can provide the radiation patterns with low correlation coefficient and higher directivity.

In order to verify the radiation characteristics of the antenna, a prototype of a switched-beam flat diversity antenna is fabricated and tested. The antenna is made of a square patch of 1.6 mm thick Taconic substrate, which has a relative dielectric constant of 2.95, printed antenna. The width and length of the patch are equal to 61.5 mm. The antenna is fed through a SMA connector at center of the antenna. Two RF switches are installed with the spacing of 30.75 mm on each side of the antenna, as shown in Fig. 4.9, for beam switching. The BAP51-02 PIN diodes are used as the RF switches. Also, the specification of the PIN diodes is available in Appendix C.



Fig. 4.9 Prototype of the antenna

The measurement is set up to measure the radiation patterns of the antenna at the frequency of 2.44 GHz. The transmitting antenna is a 90° corner reflector antenna and the receiving antenna (under tested antenna) is a switched-beam flat diversity antenna. The transmitting antenna is connected to the HP8530A Network Analyzer on port 1 to transmit the electromagnetic wave. The receiving antenna (under tested antenna) is rotated to collect the received power in each angle. The HP83050A Microwave System Amplifier is used to amplified the received power before input to the HP8530A Network Analyzer on port 2 and then the radiation pattern will be recorded. In the measurement, the transmitting and receiving antennas are placed 2.6 m apart to avoid the near-field effects. The HP8530A Network Analyzer is set for measuring S_{21} parameter (transmission measurement) at a single frequency of 2.44 GHz in angle domain starting from 0° to 360° with 2° increment angle to collect the radiation pattern of the receiving antenna (under tested antenna).

This material is reserved for educational use only, not allowed for commercial use.

Forbidden to modify the content, and cite the document when use.

From the experiment, the radiation pattern of the antenna can be directed in x direction by switched on the RF switches in y direction and switched off the RF switches in x direction. On the other hand, the radiation pattern of the antenna can be directed in y direction by switched on the RF switches in x direction and switched off the RF switches in y direction. The measured radiation patterns of the antenna are compared with the calculated results and illustrated in Fig. 4.10(a) and 4.10(b). The measured results agree with the calculated results. The radiation in undesired direction can be suppressed by switched on the RF switches in that direction. In addition, the narrower beamwidth can be observed in measured radiation pattern. For the radiation pattern in elevation plane, the measured radiation pattern is compared with the calculated radiation pattern as shown in Fig. 4.11. The radiation pattern is rather symmetrical in front lobe and is null at $\theta = 0^\circ$ and 180° , which is agree with the calculated result. But the back lobe of the radiation pattern is not quite agree with the calculation because it is disturbed from the feeding connector and coaxial line which is connected to the antenna. However, the back lobe of the radiation pattern is insignificant in practical use (the antenna will be installed on the case of computer or laptop that will cancel the back lobe).

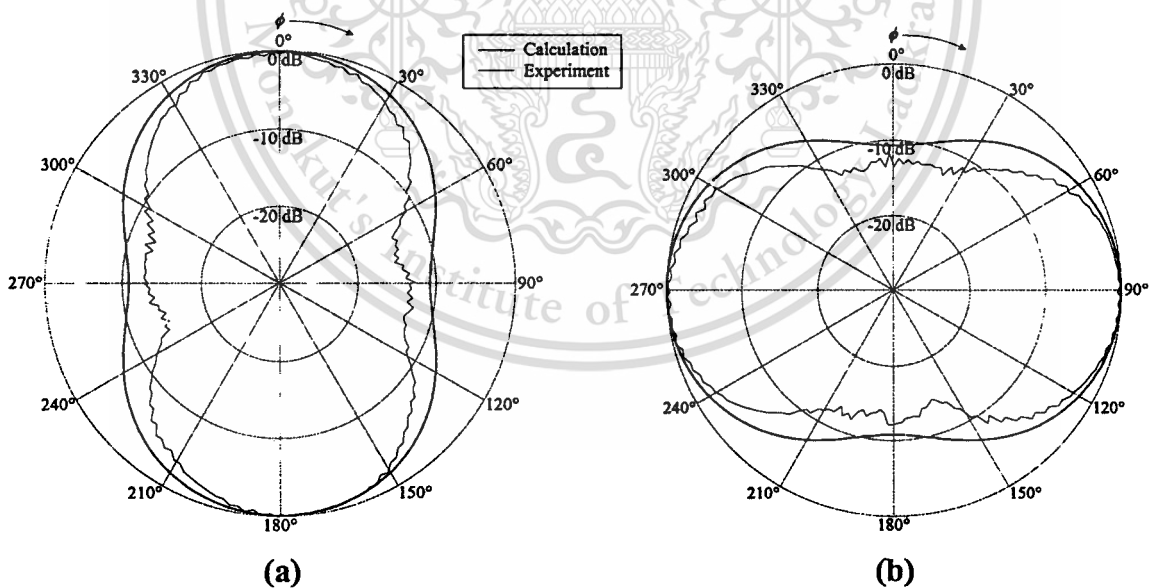


Fig. 4.10 Radiation patterns in azimuth plane

(a) x direction

(b) y direction

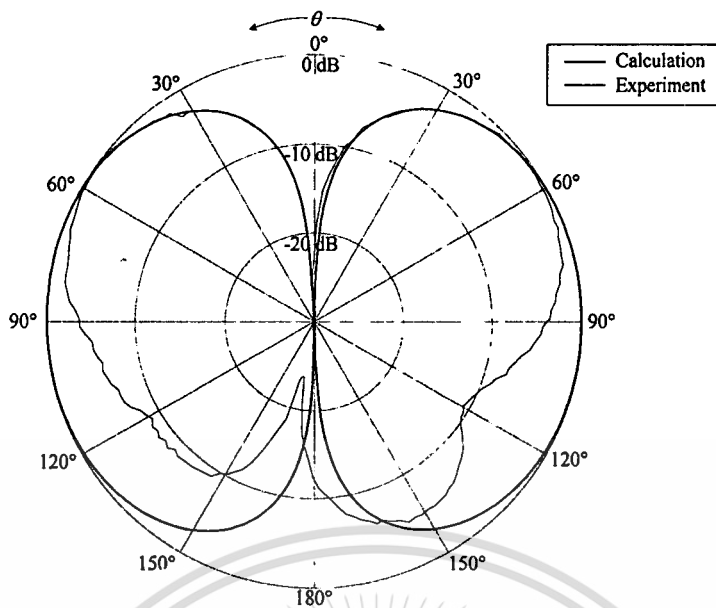


Fig. 4.11 Radiation patterns in elevation plane

In addition, the directivity of the antenna as a function of frequency is found out. The directivity of the antenna can be obtained from the Friis Equation as shown below [34];

$$\frac{P_r}{P_t} = \left(\frac{\lambda}{4\pi R} \right)^2 D_{o_t} D_{o_r} \quad (4.7)$$

where P_t and P_r are transmitted and received power, respectively. The term $(\lambda/4\pi R)^2$ is the free-space loss. R is the distance between the transmitting and receiving antennas. D_{o_t} and D_{o_r} are the directivity of the transmitting and receiving antennas, respectively. From (4.7), the directivity of the receiving antenna can be obtained from the knowledge of the ratio P_r/P_t . Therefore, the measurement is set up to get the ratio P_r/P_t .

The measurement set-up is the same as for radiation pattern measurement but the HP8530A Network Analyzer is set for measuring S_{21} parameter in frequency domain with start and stop frequency of 2.40 and 2.48 GHz, respectively, which corresponds to the operating frequency range for WLAN system in ISM frequency band. From the measurement, the S_{21} , which corresponds to the ratio P_r/P_t , is recorded with respect to the frequency. The maximum directivity of the transmitting antenna is about 9 dBi throughout the testing frequency range. With above results, the directivity of the receiving antenna (under tested antenna) can be found out. Thus, the maximum directivity

This material is reserved for educational use only, not allowed for commercial use.

Forbidden to modify the content, and cite the document when use.

of a switched-beam flat diversity antenna over the operating frequency range is obtained as illustrated in Fig. 4.12.

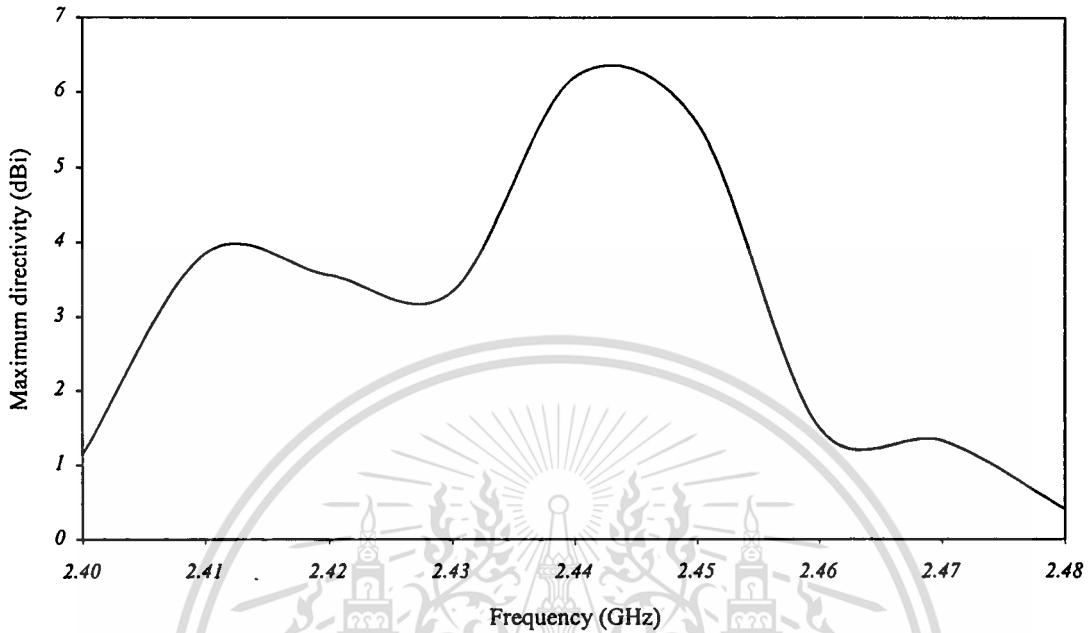


Fig. 4.12 Measured directivity with respect to frequency

As the result, the maximum directivity of the antenna is not flat over the operating band. It increases for increasing frequency until the highest directivity is observed at the center frequency of 2.44 GHz, then the directivity decreases for the increasing frequency. In addition, the directivity at the lower frequency is higher than for the upper frequency. The highest directivity of 6.21 dBi at the center frequency of 2.44 GHz can be obtained.

4.4 Conclusions

The radiation characteristics of the antenna are investigated in this chapter. The radiation patterns and the directivity of the antenna are computed by FDTD method. The different values of the spacing d between two RF switches on each side of the antenna are applied in FDTD computation to find the optimum configuration of the antenna that can provide the suitable characteristics. In addition, the characteristics of the antenna with and without the shorting posts at the corners of the antenna are compared. As the results, it is found that the radiation pattern with more suppression of radiation in undesired direction can be obtained when the spacing d between two RF switches on each side of the antenna is equal to 0.25λ for both of the antenna with and without the shorting posts. However,

the maximum directivity of the antenna without the shorting posts is higher than for the antenna with the shorting posts. Therefore, the suitable characteristics can be obtained from the optimum configuration of antenna with two RF switches installed with the spacing d equals 0.25λ on each side of the antenna, and without the shorting posts. Accordingly, the antenna is fabricated and tested. The measurement is set up to measure the radiation patterns and directivity of the antenna. The radiation patterns are measured in azimuth and elevation planes. The results show that the radiation pattern with more suppression of the radiation in undesired direction can be obtained by switched on the RF switches that are installed with the appropriate spacing of 0.25λ between two RF switches on each side of the antenna. The experimental results agree with calculated results both of the radiation pattern in azimuth and elevation planes. In addition, the more than 0 dBi antenna directivity is required for the WLAN system [14]. The directivity of the antenna is found out in the operating frequency range of 2.40-2.48 GHz. The highest directivity of 6.21 dBi is obtained at the center frequency of 2.44 GHz, and the directivity of the antenna is greater than 0 dBi over the operating frequency range. Therefore, this antenna can serve the requirement for the system. From the experimental results, the radiation characteristics of a switched-beam diversity flat antenna are verified and the suitable radiation characteristics of the antenna for WLAN application can be provided by this antenna.

CHAPTER 5

DIVERSITY CHARACTERISTICS OF THE ANTENNA

Since signal fading in the mobile environment causes severe reception problem, diversity techniques are used to reduce fading effects. Usually, the diversity is applied to the receiving site, and it can take the form of space diversity, field component diversity, frequency diversity, polarization diversity and directivity diversity. The diversity performance of each diversity scheme can be evaluated from the correlation coefficient between the antennas, and the same performance can be obtained from the same correlation coefficient. Also, the combining techniques, that are used to combine two signals which are received from the diversity scheme, have to be considered. There are four general combining techniques: Maximal ratio combining (MRC), Equal-gain combining (EGC), Selective combining (SEC) and Switch combining (SWC). Each of the combining techniques is based on different approach that causes the different complication of circuit, cost and the performance. Accordingly, the diversity scheme and the combining technique should be chosen appropriately to yield the better diversity performance. In this chapter, the correlation coefficient of the antenna is investigated and used to evaluate the diversity performance of the antenna in term of the diversity gain, which is dependent on the correlation coefficient of the antenna and the combining technique.

5.1 Correlation coefficient

In order to evaluate the diversity performance of the diversity antenna, the correlation coefficient has to be investigated. The correlation coefficient is a statistical value indicating the similarity in the voltages received by the antennas. It is most commonly used to evaluate the diversity performance of two antennas on a single receiver. The theoretical expression of the correlation coefficient of antenna diversity is written as [35]

$$\rho = \frac{R_{12}}{(\sigma_1^2 \sigma_2^2)^{1/2}} \quad (5.1)$$

The cross-covariance of the two received voltages, R_{12} , is given by

$$\begin{aligned}
 R_{12} &= \langle V_1(t)V_2^*(t) \rangle \\
 &= \int_0^{2\pi} \int_0^{2\pi} [XPR \cdot E_{\theta_1}(\theta, \phi)E_{\theta_2}^*(\theta, \phi)P_{\theta}(\theta, \phi) \\
 &\quad + E_{\phi_1}(\theta, \phi)E_{\phi_2}^*(\theta, \phi)P_{\phi}(\theta, \phi)]e^{-jkx} \sin \theta d\theta d\phi
 \end{aligned} \tag{5.2}$$

where the brackets indicate the average, and the asterisk indicates the complex conjugate. XPR represents the cross-polarization power ratio. $E_{\theta n}$ and $E_{\phi n}$ are the complex expressions of the θ and ϕ components of the electric field pattern of the antenna n ($n = 1, 2$). P_{θ} and P_{ϕ} are the θ and ϕ components of the angular density functions of incoming plane waves, respectively. k is the wave number and x is the phase difference of the incident waves at the two antennas. Also, the standard deviations σ_1 and σ_2 of the complex envelope of the first and the second signal are given by

$$\begin{aligned}
 \sigma_1^2 &= \langle V_1(t)V_1^*(t) \rangle \\
 &= \int_0^{2\pi} \int_0^{2\pi} [XPR \cdot E_{\theta_1}(\theta, \phi)E_{\theta_1}^*(\theta, \phi)P_{\theta}(\theta, \phi) \\
 &\quad + E_{\phi_1}(\theta, \phi)E_{\phi_1}^*(\theta, \phi)P_{\phi}(\theta, \phi)] \sin \theta d\theta d\phi,
 \end{aligned} \tag{5.3}$$

$$\begin{aligned}
 \sigma_2^2 &= \langle V_2(t)V_2^*(t) \rangle \\
 &= \int_0^{2\pi} \int_0^{2\pi} [XPR \cdot E_{\theta_2}(\theta, \phi)E_{\theta_2}^*(\theta, \phi)P_{\theta}(\theta, \phi) \\
 &\quad + E_{\phi_2}(\theta, \phi)E_{\phi_2}^*(\theta, \phi)P_{\phi}(\theta, \phi)] \sin \theta d\theta d\phi.
 \end{aligned} \tag{5.4}$$

Substituting (5.2), (5.3) and (5.4) into (5.1), the general theoretical equation, which takes into account the effect of XPR and the incident wave distribution of the θ and ϕ components, can be obtained. Notice that the correlation coefficient can be calculated by the knowledge of the radiation patterns of the mobile antenna and the distribution function of incident waves or propagation model.

In this work, the Clarke's model [32] is applied. It is assumed that the incident waves arriving at the mobile antenna are concentrated in the horizontal plane ($\theta = \pi/2$), and that the angular density function of incident waves is uniformly distributed throughout 0 to 2π . Therefore, the angular density function of incident waves can be written as

$$P_\theta = P_\phi = \frac{1}{2\pi} \delta(\theta - \frac{\pi}{2}). \quad (5.5)$$

In addition, it is assumed that the incident wave is vertically polarized and the polarization is unchanged on the scattering so that the received field is also vertically polarized. Thus, only the co-polarization is considered and the effect of XPR will be neglected in this model. According to this assumption, the expressions of the cross-covariance R_{12} and the standard deviation σ_1 and σ_2 are simplified to

$$R_{12} = \frac{1}{2\pi} \int_0^{2\pi} E_{\theta_1}(\pi/2, \phi) E_{\theta_2}^*(\pi/2, \phi) d\phi, \quad (5.6)$$

$$\sigma_1^2 = \frac{1}{2\pi} \int_0^{2\pi} E_{\theta_1}(\pi/2, \phi) E_{\theta_1}^*(\pi/2, \phi) d\phi, \quad (5.7)$$

$$\sigma_2^2 = \frac{1}{2\pi} \int_0^{2\pi} E_{\theta_2}(\pi/2, \phi) E_{\theta_2}^*(\pi/2, \phi) d\phi. \quad (5.8)$$

Then, the simplified equation of the correlation coefficient can be obtained as

$$\rho = \frac{\int_0^{2\pi} E_{\theta_1}(\phi) E_{\theta_2}^*(\phi) d\phi}{\left[\int_0^{2\pi} E_{\theta_1}(\phi) E_{\theta_1}^*(\phi) d\phi \cdot \int_0^{2\pi} E_{\theta_2}(\phi) E_{\theta_2}^*(\phi) d\phi \right]^{1/2}}. \quad (5.9)$$

From (5.9), the correlation coefficient can be calculated from the radiation patterns of the two antennas. Although, a switched-beam flat diversity antenna is based

This material is reserved for educational use only, not allowed for commercial use.

Forbidden to modify the content, and cite the document when use.

on the structure of only one printed antenna but the antenna provides the switchable beam, so this antenna can perform as good as two antennas. Since, the radiation pattern of the antenna in each direction, x direction and y direction, is corresponding to the radiation pattern of the first and the second antenna. Thus, the correlation coefficient between the radiation patterns in x direction and y direction are investigated.

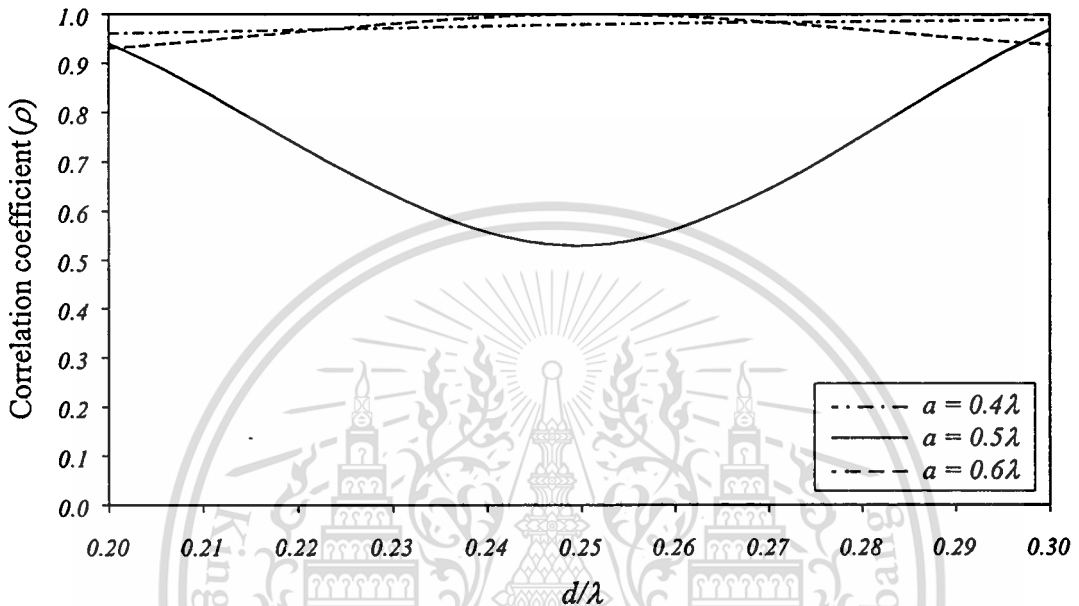


Fig. 5.1 Relation between correlation coefficient and the RF switches spacing d

The correlation coefficient of this antenna have been investigated and presented in [19]. The antenna is analyzed by Numerical Electromagnetic Code (NEC-2) based on the method of moments with wire grid model. The radiation patterns of the antenna are calculated and used to evaluate the correlation coefficient of the antenna. Due to the low correlation coefficient of the antenna is required, so the patch size a and the spacing d between RF switches are varied to obtained the appropriate value of a and d that can give the lowest correlation coefficient. It is found that the lowest correlation coefficient of 0.53 can be observed when the patch size equals a half-wavelength ($a = 0.5\lambda$) and the space between RF switches equals a quarter-wavelength ($d = 0.25\lambda$), otherwise the correlation coefficient is higher, especially for a equals 0.4λ and 0.6λ , the correlation coefficient is closed to a unit as shown in Fig. 5.1.

Since the wire grid model is unable to model the dielectric substrate, just modeled as air-filled, then the FDTD method is used to analyze the antenna with more practical model. The dielectric substrate can be modeled by FDTD method, and the antenna model.

This material is reserved for educational use only, not allowed for commercial use.

Forbidden to modify the content, and cite the document when use.

of interest is the antenna model with the patch size of 0.5λ . Because the low correlation coefficient can be observed at the patch size of 0.5λ as shown in preliminary results (in Fig. 5.1). Thus, the calculated radiation patterns of the antenna by using FDTD method as presented in the previous chapter are used to estimate the correlation coefficient of the antenna. The correlation coefficient of the antenna is investigated as a function of the spacing d between RF switches.

In general, the envelope correlation coefficient (ρ_e) is the quantity that obtained in the experimentation and, in theoretical, it can be approximated from the correlation coefficient (ρ), which is voltage correlation coefficient, as [32]

$$\rho_e \approx |\rho|^2. \quad (5.10)$$

The value of envelope correlation coefficient of the antenna should not exceed 0.7 in order that the diversity performance can be obtained [36].

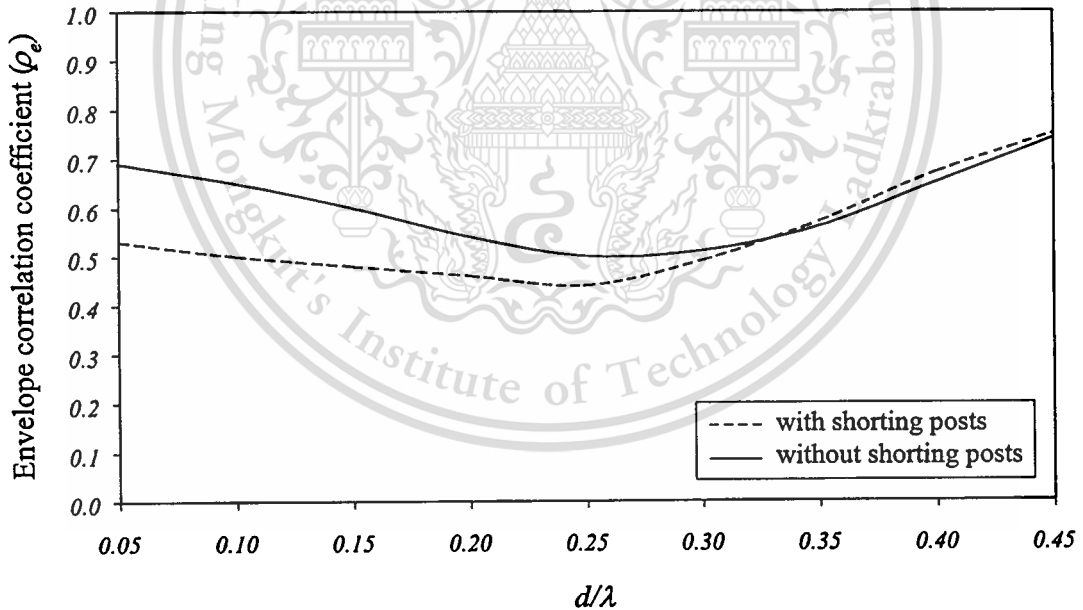


Fig. 5.2 Calculated envelope correlation coefficient of the antenna

The envelope correlation coefficient of this antenna is investigated as a function of the spacing d between two RF switches on each side of the antenna. Fig. 5.2 shows the envelope correlation coefficient of the antenna with and without shorting posts. The dash line shows the envelope correlation coefficient of the antenna with shorting posts. It is

This material is reserved for educational use only, not allowed for commercial use.

Forbidden to modify the content, and cite the document when use.

found that the lowest envelope correlation coefficient of 0.44 will be obtained when d equals 0.25λ and otherwise the envelope correlation coefficient of the antenna is increasing. For the envelope correlation coefficient of the antenna without shorting posts, the result is given by solid line in Fig. 5.2. As the result, the lowest envelope correlation coefficient also be obtained when d equals 0.25λ . The envelope correlation coefficient of 0.5 is obtained that is slightly higher than the envelope correlation coefficient of the antenna with shorting posts.

From the results, it can be concluded that the lowest envelope correlation coefficient will be obtained when d equals 0.25λ . There is a slightly difference between the envelope correlation coefficient of the antenna with and without shorting posts, so it can be understood that there is no difference of the diversity performance obtained from the antenna with and without shorting posts. Because the diversity performance decreases when the correlation coefficient increases, but this dependence is weak as long as the correlation coefficient is low [36].

5.2 Diversity gain

Generally, the diversity performance is measured as diversity gain. It is defined as the ratio of the received signal of the diversity combiner, r_c , relative to its mean value, \bar{r}_c , and the received signal of the single branch, r_1 , relative to its mean value, \bar{r}_1 , for a given signal level probability. Thus, the diversity gain is the improvement in received signal for a given signal level probability. It can be written in decibels as

$$\text{Diversity gain (dB)} = \left[\frac{r_c}{\bar{r}_c} (\text{dB}) - \frac{r_1}{\bar{r}_1} (\text{dB}) \right]_{\text{at given probability}} \quad (5.11)$$

and the ratios within this equation are found from the signal cumulative probability functions.

Since the Rayleigh fading is assumed, the probability density function (PDF) of the received signal at the single branch is given by

$$p(r_1) = \frac{1}{\bar{r}_1} \exp\left[-\frac{r_1}{\bar{r}_1}\right]. \quad (5.12)$$

The associated cumulative distribution function (CDF) is

$$\text{Prob}(r_1 \leq x) = 1 - \exp\left[-\frac{r_1}{\bar{r}_1}\right], \quad (5.13)$$

where x is a given signal level. For two correlated diversity branches, the joint PDF of two Rayleigh distribution is considered, which is given as [37]

$$p(r_1, r_2) = \frac{1}{\bar{r}_1 \bar{r}_2 (1 - |\rho|^2)} \cdot I_0 \left[\frac{2|\rho| \sqrt{r_1 r_2 / \bar{r}_1 \bar{r}_2}}{(1 + |\rho|^2)} \right] \cdot \exp \left[-\frac{r_1 / \bar{r}_1 + r_2 / \bar{r}_2}{(1 - |\rho|^2)} \right]. \quad (5.14)$$

where $I_0(\cdot)$ is the zero-order modified Bessel function of the first kind. From this equation, the CDF of received signal after combining can be determined for different combining techniques:

In this work, the switched combining is implemented. By this technique, the received signal power is chosen as the switching criterion; the switching algorithm is as follow: the power on the chosen (first) branch is compared with a certain preset threshold value A . If the power on this branch drops below A , the other (second) branch is chosen. If the power on this second branch is above A , it becomes the output branch. However, if the power on the second branch is also below A , two different strategies can be perceived:

- (1) The second branch stays the chosen branch to avoid needless switching, a strategy called “switch-and-stay”. A switch to other branch is only made if power on the chosen branch cross A in negative direction.
- (2) A switch back to the first branch is made, which may lead to a period of continuous switching between branches until the power on one of them exceeds A , this strategy is called “switch-and-examine”.

For example, two fading signals are received as shown in Fig. 5.3(a), the resultant signal using switch-and-stay and switch-and-examine strategies are illustrated in Fig. 5.3(b) and (c), respectively. The switch-and-stay approach has the disadvantage that the output signal can stay longer below the threshold A . On the other hand, the switch-and-examine approach has the inconvenience of the noise bursts caused by the rapid switching between the two signals when both are below the threshold A .

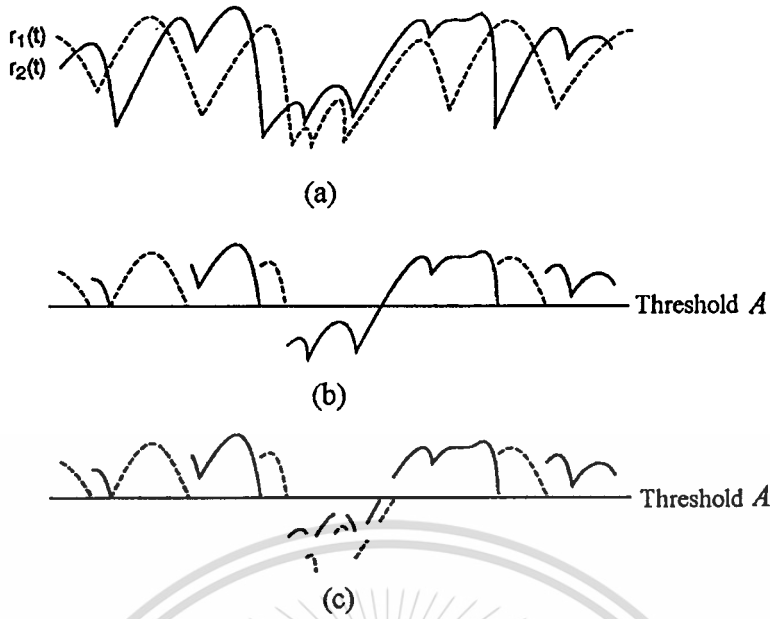


Fig. 5.3 Switched combining techniques

(a) Two fading signals

(b) Resultant signal using switch-and-stay strategy

(c) Resultant signal using switch-and-examine strategy

In order to evaluate the performance, the CDF of received signal after combining for switched combining for correlated branches is determined and given as

$$\text{Prob}(r \leq x) = \begin{cases} \int_0^x \int_0^A p(r_1, r_2) dr_1 dr_2 & , 0 < x < A \\ \int_0^x \int_0^x p(r_1, r_2) dr_1 dr_2 + \int_x^A \int_0^x p(r_1, r_2) dr_1 dr_2 & , x \geq A \end{cases} \quad (5.15)$$

which is based on the switch-and-examine strategy [38]. The joint PDF, $p(r_1, r_2)$, in this equation comes from (5.14). Accordingly, the diversity gain can be evaluated. Fig. 5.4 shows the plots of (5.15) for the envelope correlation coefficient of 0.44 and 0.5, which correspond to the lowest correlation coefficient of the antenna with and without shorting posts, respectively. It can be seen that the diversity gain increases for the decreasing probabilities until the threshold A is reached and gain settles at a constant value, which is the highest diversity gain obtained with the switched combining. In Fig. 5.4, the diversity gain is evaluated at 1% probability and the diversity gain of 8 dB is obtainable from the

This material is reserved for educational use only, not allowed for commercial use.

Forbidden to modify the content, and cite the document when use.

antenna without shorting posts ($\rho_e = 0.5$) that is only 0.3 dB less than the diversity gain obtained from the antenna with shorting posts ($\rho_e = 0.44$), as was mentioned before that the diversity gain decreases slightly at the low correlation coefficient.

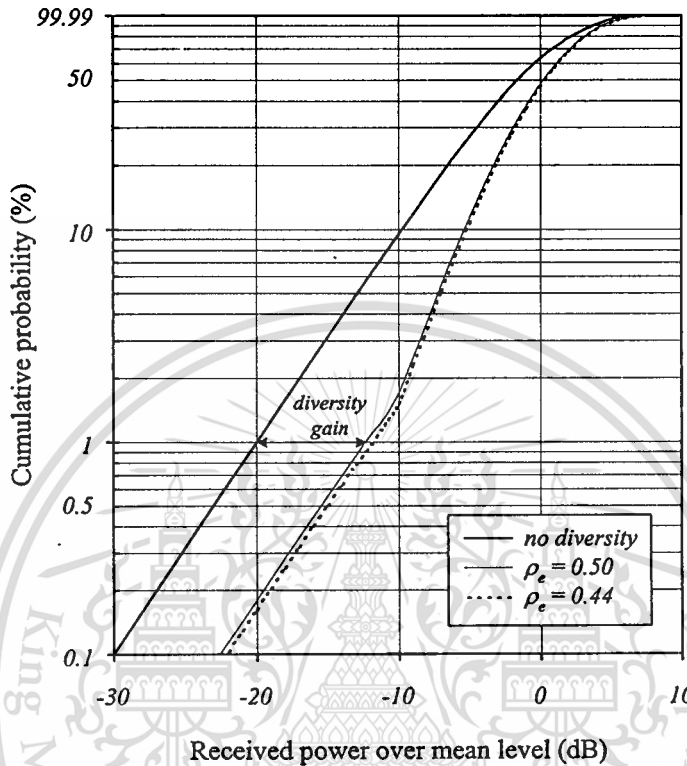


Fig. 5.4 CDF of received signal after combining for switched combining with $A = -10$ dB for correlated branches

Fig. 5.5 shows the plots of (5.15) for different values of threshold A for the correlated branches with the envelope correlation coefficient of 0.5. It is found that the diversity gain for switched combining is influenced by the choice of the threshold value. The highest diversity gain increases for the decreasing threshold value. If the threshold value is very low, the reliability that power on a chosen branch is above the threshold increases, which means that the probability of a switch decreases. Such the threshold value of -5 , -10 and -15 dB, the reliabilities that power on a chosen branch is above the threshold are 10%, 98.5% and 99.8%, respectively. However, the threshold value must be set to the lowest acceptable received signal level.

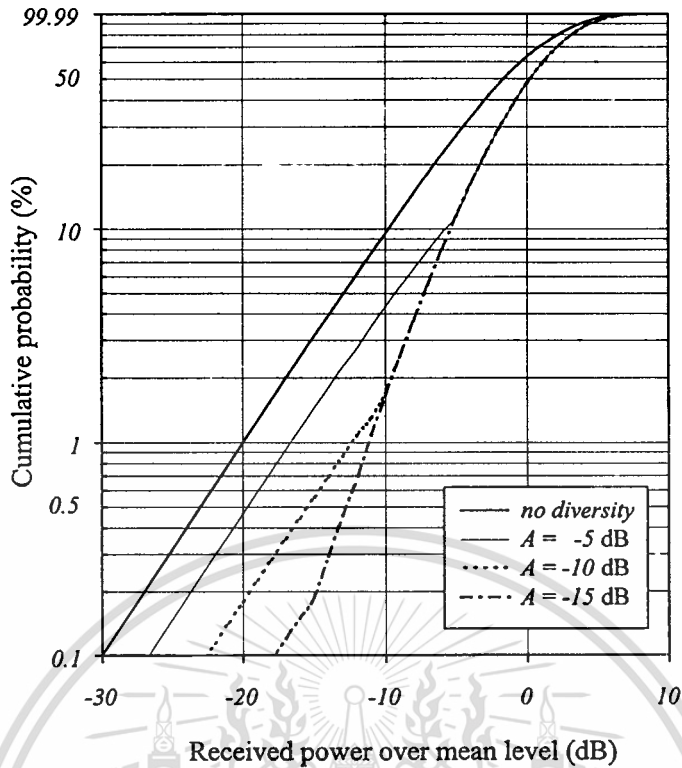


Fig. 5.5 CDF of received signal after combining for switched combining with different values of A for correlated branches with the envelope correlation coefficient of 0.5

5.3 Experimental results

In this section, the correlation coefficient and diversity gain of the antenna are investigated experimentally. The correlation coefficient of the antenna can be investigated from the measured radiation patterns. In addition, the circuit that is used to control the beam switching and combine the receiving signals is formed and applied to the antenna. Subsequently, the received signal of a switched-beam flat diversity antenna are measured and compared with the received signal of a non-diversity (do not switch beam) antenna to verify the diversity performance of the antenna and received signal improvement.

The correlation coefficient of the antenna for different values of the spacing d between the RF switches on each side of the antenna can be evaluated from the radiation patterns directed in x and y direction by using relation expressed in (5.9). From the measured radiation patterns, the correlation coefficient between radiation patterns in x and y direction for each value of d are evaluated and illustrated in Fig. 5.6. As the result, the lowest correlation coefficient of the antenna can be obtained when d is equal to 0.25λ , which agree with the calculated result. The correlation coefficient of 0.27 is obtained that

This material is reserved for educational use only, not allowed for commercial use.

Forbidden to modify the content, and cite the document when use.

is lower than the calculated one. By this correlation coefficient of the antenna, it can verify that the diversity performance and received signal improvement can be obtained from this antenna. However, the diversity performance of the antenna also be tested to clarify that the received signal can be improved by this antenna.

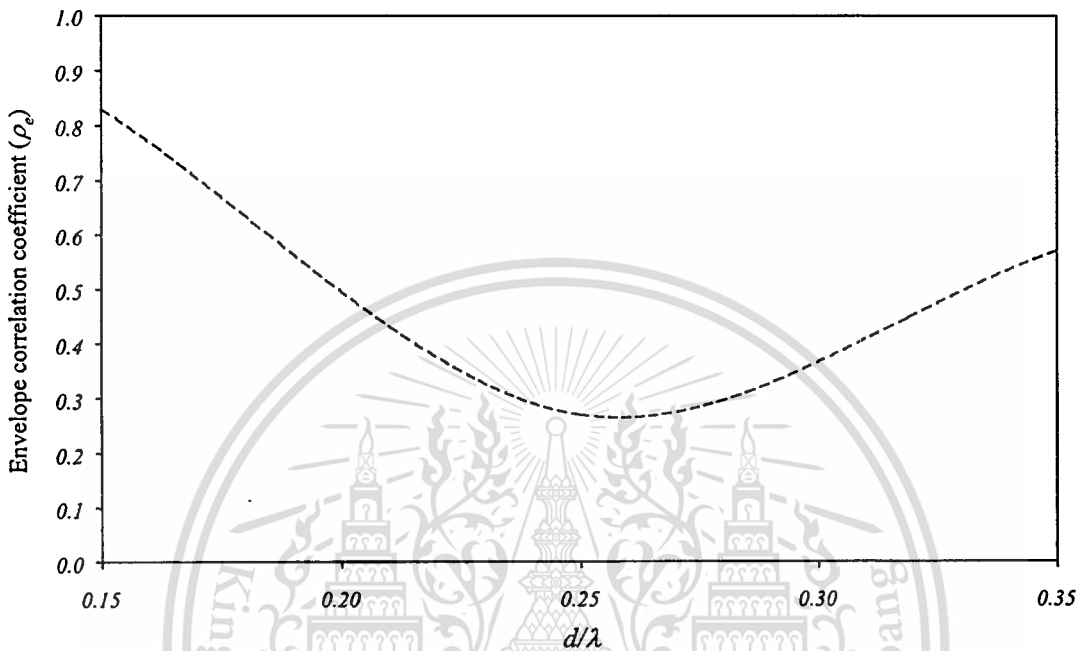


Fig. 5.6 Measured envelope correlation coefficient as a function of d

Since the pattern diversity technique is applied to a switched-beam flat diversity antenna by switching the beam of the antenna, the switched combining technique is used to combine the received signals. The beam switching can be realized by switched on/off the RF switches (PIN diodes) that are installed on each side of the antenna. Therefore, the switched combining circuit is established to control the switching of RF switches and combining the received signals at the input of a receiver. The diagram of the circuit can be illustrated in Fig. 5.7.

With this circuit, the beam switching will be performed when the received signal is lower than the threshold level. In Fig. 5.7, the beam switching can be controlled by the process as described below:

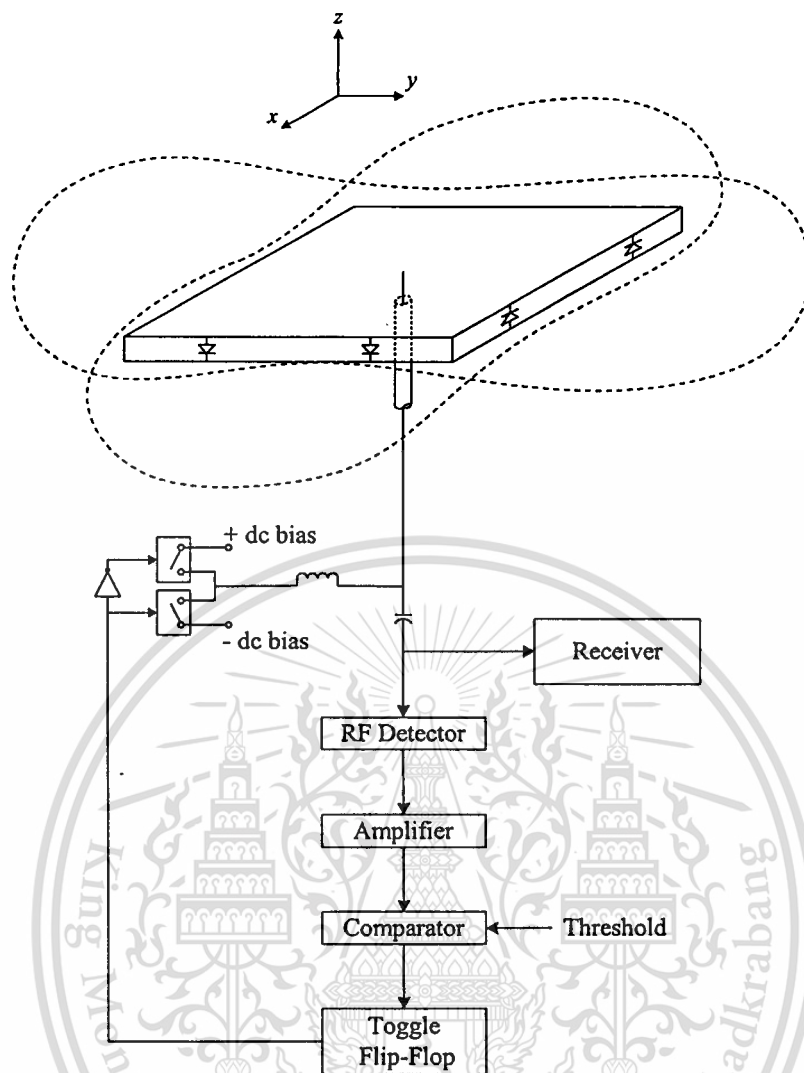


Fig. 5.7 Diagram of the switched combining circuit

Firstly, the received signal input to the receiver and simultaneously detected by the RF detector. The dc level is detected at the output of the RF detector and it is amplified before input to the comparator. Then, the dc level is compared with the threshold level. The condition for decision of comparator is set to allow the positive and negative output for the input which is lower and higher than the threshold level, respectively. By this condition, the toggle flip-flop with positive-edge triggered is used so that it will be triggered when the received signal is lower than the threshold level. The output of the toggle flip-flop, which is used as the control signal of the analog switches, will be toggled that causes the status of the analog switches are changed and the dc bias will be switched from positive to be negative dc bias (or negative to be positive dc bias), then the beam of the antenna is switched to orthogonal direction.

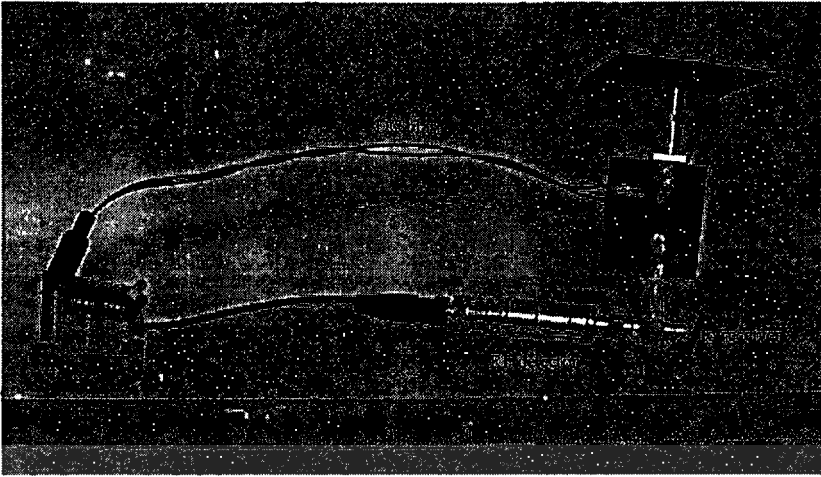


Fig. 5.8 Antenna with switched combining circuit

Accordingly, the switched combining circuit is incorporated with the antenna, as illustrated in Fig. 5.8, and the radiation pattern of this pattern diversity antenna is tested. The threshold level is about -30 dBm, which is the lowest signal level that the RF detector can detect. The radiation pattern of the antenna can be given in Fig. 5.9. As the result, it can be seen that the received signal can be improved by this antenna. In addition, the diversity gain of the antenna is approximated by comparing the received signals of the diversity (switched beam) antenna to non-diversity (do not switched beam) antenna. The diversity gain of 3 dB at 1% probability can be obtained from the antenna, as shown in Fig. 5.10.

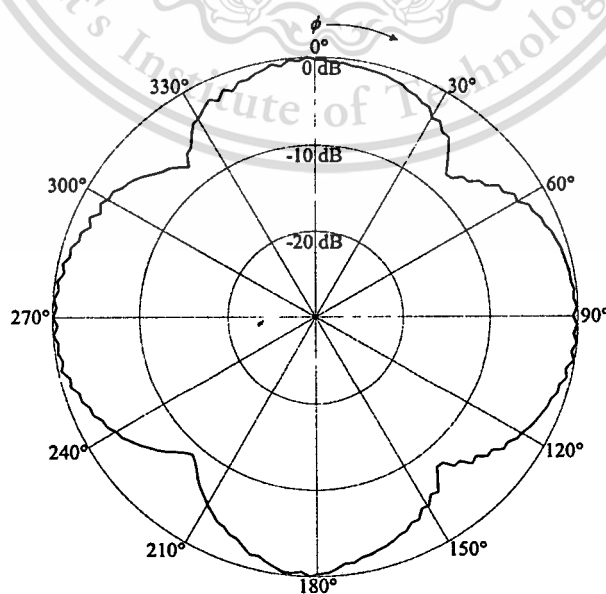


Fig. 5.9 Radiation pattern of a switched beam flat diversity antenna

This material is reserved for educational use only, not allowed for commercial use.

Forbidden to modify the content, and cite the document when use.

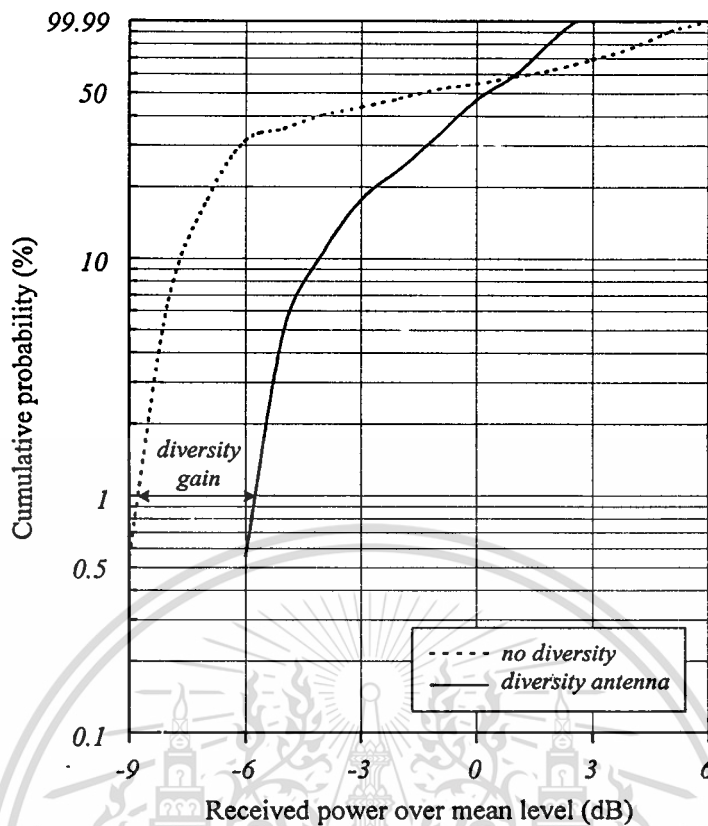


Fig. 5.10 Cumulative probability and diversity gain

As the result, the diversity gain is lower than the calculated result because the number of the collected data used for diversity gain approximation is too small. Moreover, in calculation, the signal distribution is considered as Rayleigh distribution but the experiment environment is not Rayleigh distribution. Therefore, if the propagation test is carried out in Rayleigh distribution environment, the number of the collected data will be larger than and distribution of the signals will agree with calculation. It is predicted that larger diversity gain will be obtained and show agreement with calculation. But the propagation test can not be performed because of the limitation of sensitivity of the RF detector. However, the diversity gain that is approximated from the radiation pattern is able to demonstrate the performance of the antenna.

5.4 Conclusions

In this chapter, the diversity characteristics of the antenna have been evaluated. The correlation coefficient of the antenna is calculated by using the radiation pattern of the antenna and the Clarke's model as an angular density function of the incident waves. It is calculated for different values of spacing d between two RF switches on each side of

This material is reserved for educational use only, not allowed for commercial use.

Forbidden to modify the content, and cite the document when use.

the antenna. The lowest correlation coefficient of can be obtained for d equals 0.25λ . The correlation coefficient of 0.44 and 0.5 are obtained from the antenna with and without the shorting posts, respectively. In addition, the diversity gain of the antenna with switched combining technique is evaluated. The diversity gain of the antenna with correlation coefficient of 0.44 and 0.5 for the antenna with and without the shorting posts are calculated. The diversity gain of 8 dB can be obtained from the antenna with shorting posts, and the antenna without shorting posts can give slightly lower diversity gain than for the antenna with shorting posts. Considering the diversity characteristics together with the radiation characteristics of the antenna, the antenna without shorting posts can give the diversity gain as close as to the diversity gain of the antenna with shorting posts, and the higher directivity can obtain from the antenna without shorting posts. Therefore, the optimum characteristics can be obtained from the antenna without shorting posts, which is fabricated and tested.

In order to clarify the diversity characteristics of the antenna, the correlation coefficient of the antenna for different values of spacing d between two RF switches on each side of the antenna are approximated from the measured radiation patterns. The lowest correlation coefficient can be obtained for d equals 0.25λ , which agree with the numerical result. The lowest correlation coefficient of 0.27 is obtained. For diversity gain, the switched combining technique is used to combine the received signals. The received signal can be improved and the diversity gain of 3 dB at 1% probability, which is approximated from the radiation pattern, is obtained.

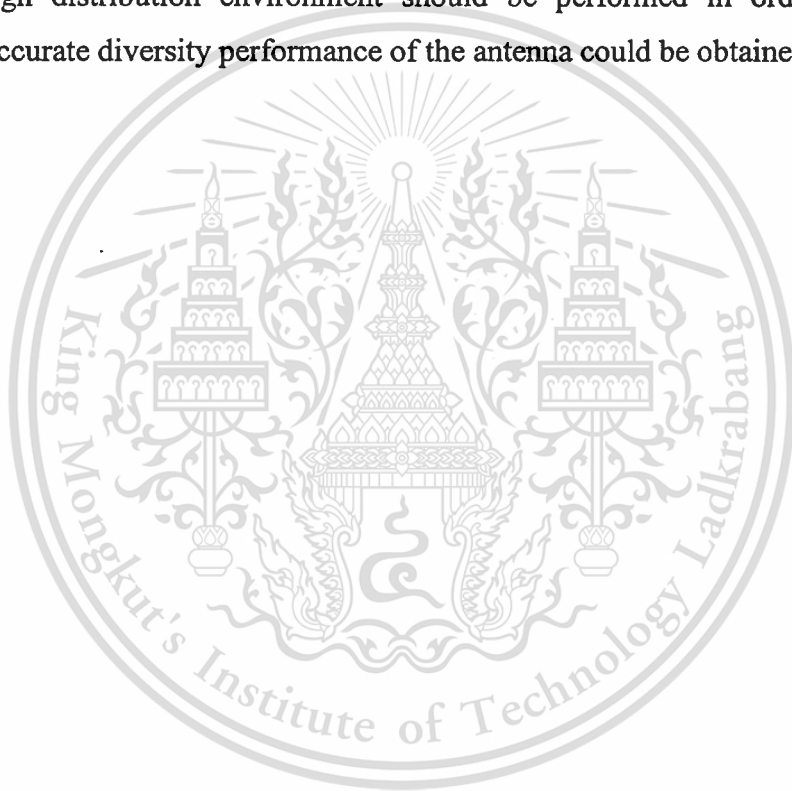
CHAPTER 6

CONCLUSIONS

Since this thesis proposes a switched-beam flat diversity antenna as a pattern diversity antenna, the literatures on diversity antenna are given in chapter 1. For the antenna analysis, the FDTD method is used that the basic elements of FDTD antenna analysis are addressed in chapter 2. The FDTD formulation in rectangular coordinates is derived. The PML absorbing boundary condition for radiation problem simulation and two standard schemes of near-field to far-field (NFFF) transformations, frequency-domain and time-domain near-field to far-field transformations, are introduced to obtain far-field responses. Also, the antenna excitation and feeding models for FDTD method are presented. In chapter 3, the antenna configuration is presented and the FDTD model of the problem is constructed. By using the FDTD method, the radiation characteristics, which are radiation patterns and directivity, of the antenna are investigated in chapter 4. The optimum radiation characteristics are found out. The calculated results show the radiation patterns of the antenna can be directed in x and y directions with the maximum directivity of 5.55 dBi at frequency of 2.44 GHz. In order to verify the characteristics of the antenna, the experiment is set up to test the radiation patterns and directivity of the antenna. From the experimental results, the radiation patterns of the antenna can be switched to direct in x and y directions. The directivity is higher than 0 dBi throughout the operating frequency band that is satisfied the requirement for the WLAN system, and the maximum directivity of 6.21 dBi can be obtained at the center frequency of 2.44 GHz. In chapter 5, the diversity characteristics of the antenna are investigated theoretically, and also, the testing of the diversity antenna is carried out to verify the diversity performance of the antenna. From the numerical results, the correlation coefficient and diversity gain of the antenna are calculated and it is found that the correlation coefficient of 0.5 can be obtained from this antenna and diversity gain of 8 dB can be obtained with the switched combining technique. In addition, the testing of the diversity antenna can clarify the diversity performance of the antenna. The correlation coefficient of 0.27 can be obtained. Due to the propagation test cannot be performed, therefore the diversity gain is approximated from the radiation pattern by comparing the received signal of the non-diversity (do not switched-beam) antenna with the received signal of the diversity (switched-beam) antenna. Consequently, the distribution of the signals are not Rayleigh

distribution as considered in calculation that effects the difference between calculation and experiment. However, the improvement of received signal with the diversity gain of 3 dB at 1% probability can be observed. Accordingly, the characteristics of the antenna can be clarified and the antenna is validated for WLAN system. Also, the received signal can be improved by this diversity antenna.

However, in order to apply the switched-beam flat diversity antenna for practical use, some development should be done in the future. Such as the sensitivity of the RF detector should be improved. The switched combining circuit should be integrated with VLSI technology in order to reduce the space for installation. In addition, the propagation test in Rayleigh distribution environment should be performed in order that more practical and accurate diversity performance of the antenna could be obtained.



REFERENCES

- [1] Ebine Y. and Yamada Y. "Vehicular-mounted diversity antennas for land mobile radios." IEEE 38th Vehicular Technology Conference, 1988. pp. 326-333.
- [2] Vaughan R.G. "Polarization diversity in mobile communications." IEEE Trans. Vehicular Technol., vol. 39, Aug. 1990. pp. 177-186.
- [3] Awadalla K.H. "Direction diversity in mobile communications." IEEE Trans. Vehicular Technol., vol. 30, Aug. 1981. pp. 121-123.
- [4] Aubrey T. and White P. "A comparison of switched pattern diversity antennas." IEEE 43rd Vehicular Technology Conference, 1993. pp. 89-92.
- [5] Ebine Y. and Yamada Y. "A vehicular-mounted vertical space diversity antenna for a land mobile radio." IEEE Trans. Vehicular Technol., vol. 40, May 1991. pp. 420-425.
- [6] Hosono S., Goto N. and Arai H. "A flat diversity antenna by disk loaded monopole and three notches." IEEE Trans. Vehicular Technol., vol. 43, May 1994. pp. 353-358.
- [7] Jensen M.A. and Samii Y.R. "Performance analysis of antennas for hand-held transceivers using FDTD." IEEE Trans. Antennas Propagat., vol. 42, Aug. 1994. pp. 1106-1113.
- [8] Ogawa K. and Uwano T. "A diversity antenna for very small 800-MHz band portable telephones." IEEE Trans. Antennas Propagat., vol. 42, Sep. 1994. pp. 1342-1345.
- [9] Colburn J.S., Samii Y.R., Jensen M.A. and Pottie G.J. "Evaluation of personal communications dual-antenna handset diversity performance." IEEE Trans. Vehicular Technol., vol. 47, Aug. 1998. pp. 737-746.
- [10] Douglas M.G., Okoniewski M. and Stuchly M.A. "A planar diversity antenna for handheld PCS devices." IEEE Trans. Vehicular Technol., vol. 47, Aug. 1998. pp. 747-754.
- [11] Vaughan R. "Switched parasitic elements for antenna diversity." IEEE Trans. Antennas Propagat., vol. 47, Feb. 1999. pp. 399-405.
- [12] Ogawa K. and Uwano T. "A variable tilted fan beam antenna for indoor base stations." Antenna and Propagation Society International Symposium, 1994. pp. 332-335.

This material is reserved for educational use only, not allowed for commercial use.

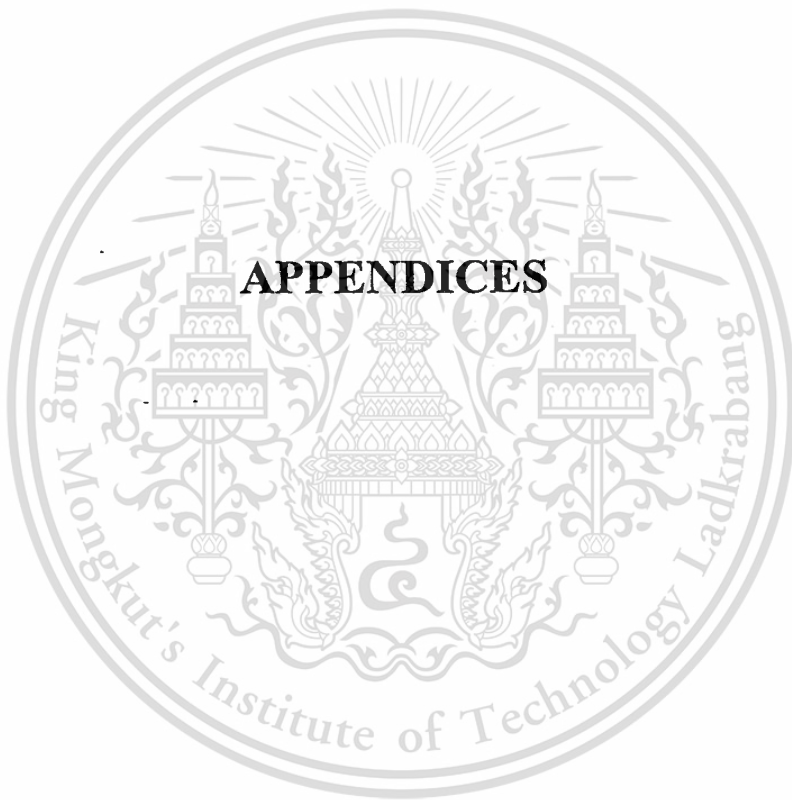
Forbidden to modify the content, and cite the document when use.

- [13] Kuga N., Arai H. and Goto N. "A notch-wire composite antenna for polarization diversity reception." *IEEE Trans. Antennas Propagat.*, vol. 46, June 1998. pp. 902-906.
- [14] Kuga N. and Arai H. "A flat four-beam switched array antenna." *IEEE Trans. Antennas Propagat.*, vol. 44, Sep. 1996. pp. 1227-1230.
- [15] Liebendörfer M. and Dersch U. "Wireless LAN diversity antenna system for PCMCIA card integration." *IEEE 47th Vehicular Technology Conference*, 1997. pp. 2022-2026.
- [16] Murakami Y., Kijima T., Iwasaki H., Ihara T., Manabe T. and Iigusa K. "A switchable multi-sector antenna for indoor wireless LAN systems in the 60 GHz band." *IEEE Trans. Microwave Theory Tech.*, vol. 46, June 1998. pp. 841-843.
- [17] Desclos L., Drenski T. and Madihian M. "An interdigitated printed antenna for PC card applications." *IEEE Trans. Antennas Propagat.*, vol. 46, Sep. 1998. pp. 1388-1389.
- [18] Ali M., Okoniewski M., Stuchly M.A. and Stuchly S.S. "Dual-frequency strip-sleeve monopole for laptop computers." *IEEE Trans. Antennas Propagat.*, vol. 47, Feb. 1999. pp. 317-323.
- [19] Ngamjanyaporn P. and Krairiksh M. "A switchable flat antenna for pattern diversity." *IEEE International Symposium on Intelligent Signal Processing and Communication Systems*, Dec. 1999. pp. 701-704.
- [20] Yee K.S. "Numerical solution of initial boundary value problems involving Maxwell's equations in isotropic media." *IEEE Trans. Antennas Propagat.*, vol. 14, May 1966. pp. 302-307.
- [21] Berenger J.P. "A perfectly matched layer for the absorption of electromagnetic waves." *J. Computational Physics*, vol. 114, Oct. 1994. pp. 185-200.
- [22] Taflove A. **Computational Electrodynamics the Finite-Difference Time-Domain Method**. Boston: Artech House. 1995.
- [23] Taflove A. **Advances in Computational Electrodynamics: The Finite-Difference Time-Domain Method**. Boston: Artech House. 1998.
- [24] Umashankar K.R., Taflove A. and Beker B. "Calculation and experimental validation of induced currents on coupled wires in an arbitrary shaped cavity." *IEEE Trans. Antennas Propagat.*, vol. 35, Nov. 1987. pp. 1248-1257.

- [25] Luebbers R., Chen L., Uno T. and Adachi S. "FDTD calculation of radiation patterns, impedance, and gain for a monopole antenna on a conducting box." *IEEE Trans. Antennas Propagat.*, vol. 40, Dec. 1992. pp. 1577-1583.
- [26] Maloney J.G., Shlager K.L. and Smith G.S. "A simple FDTD model for transient excitation of antennas by transmission lines." *IEEE Trans. Antennas Propagat.*, vol. 42, Feb. 1994. pp. 289-292.
- [27] Yee K.S., Ingham D. and Shlager K. "Time-domain extrapolation to the far field based on FDTD calculations." *IEEE Trans. Antennas Propagat.*, vol. 39, Mar. 1991. pp. 410-413.
- [28] Luebbers R.J., Kunz K.S., Schneider M. and Hunsberger F. "A finite-difference time-domain near zone to far zone transformation." *IEEE Trans. Antennas Propagat.*, vol. 39, Apr. 1991. pp. 429-433.
- [29] Luebbers R.J., Ryan D. and Beggs J. "A two-dimensional finite-difference time-domain near zone to far zone transformation." *IEEE Trans. Antennas Propagat.*, vol. 40, July 1992. pp. 848-851.
- [30] Shlager K.L. and Smith G.S. "Near-field to near-field transformation for use with FDTD method for use with FDTD method and its application to pulsed antenna problems." *Electron. Lett.*, vol. 30, Aug. 1994. pp. 1262-1264.
- [31] Douglas M.G., Okoniewski M. and Stuchly M.A. "A planar diversity antenna for handheld PCS devices." *IEEE Trans. Vehicular Technol.*, vol. 47, Aug. 1998. pp. 747-754.
- [32] Omiya M., Hikage T., Ohno N., Horiguchi K. and Itoh K. "Design of cavity-backed slot antennas using the finite-difference time-domain technique." *IEEE Trans. Antennas Propagat.*, vol. 46, Dec. 1998. pp. 1853-1858.
- [33] Clarke R.H. "A statistical theory of mobile radio reception." *Bell Syst. Tech. J.*, vol. 47, Jul.-Aug. 1968. pp. 957-1000.
- [34] Balanis C.A. **Antenna Theory: Analysis and Design**. 2nd edition. New York: John Wiley & Sons, Inc. 1997.
- [35] Fujimoto K. and James J.R. **Mobile Antenna Systems Handbook**. Boston: Artech House. 1994.
- [36] Jakes W.C. **Microwave Mobile Communications**. New Jersey: IEEE Press. 1994.
- [37] Lee W.C.Y. **Mobile Communications Engineering: Theory and Applications**. 2nd edition. New York: McGraw-Hill. 1998.

- [38] Deursen J.-P.V. and Jansen M.G. "Switched antenna diversity within a DECT system." IEEE 2nd Symposium on Communications and Vehicular Technology, 1994. pp. 141-148.





This material is reserved for educational use only, not allowed for commercial use.

Forbidden to modify the content, and cite the document when use.

By substitution (A.2a) into (A.1b), the result is

$$\hat{u}^{n+1} e^{ikx_j} = T(\Delta t, \Delta x) \hat{u}^n e^{ikx_j} \quad (\text{A.2b})$$

or

$$\hat{u}^{n+1} = e^{-ikx_j} T(\Delta t, \Delta x) \hat{u}^n e^{ikx_j} \hat{u}^n = G(\Delta t, \Delta x) \hat{u}^n, \quad (\text{A.2c})$$

where G is the amplification matrix of the difference scheme for the Fourier mode of wave number k .

The Fourier modes can be expressed as an expansion in the eigenvectors of the amplification matrix G . In particular let \hat{u}_μ^o be the amplitude of the vector Fourier mode along the eigenvector $\bar{S}^{(\mu)}$ at time step zero, then

$$\hat{u}^o = \sum_{\mu} \hat{u}_\mu^o \bar{S}^{(\mu)} \quad (\text{A.3a})$$

From \hat{u}^o and (A.2c), one can find \hat{u}^n as

$$\hat{u}^n = (G)^n \hat{u}^o = (G)^n \sum_{\mu} \hat{u}_\mu^o \bar{S}^{(\mu)} \quad (\text{A.3b})$$

Now $\bar{S}^{(\mu)}$ as an eigenvector of G satisfies

$$(G - g_\mu) \bar{S}^{(\mu)} = 0 \text{ or } G \bar{S}^{(\mu)} = g_\mu \bar{S}^{(\mu)} \quad (\text{A.3c})$$

Thus, from (A.3b)

$$\hat{u}^n = \sum_{\mu} \hat{u}_\mu^o (g_\mu)^n \bar{S}^{(\mu)} \quad (\text{A.3d})$$

For $|g_\mu| \leq 1$ this behavior for \hat{u}^n is stable. Equivalently, it is required that

$$g_\mu^* g_\mu = |g_\mu|^2 \leq 1 \quad (\text{A.4})$$

Now, the time centered leapfrog method is being recasted into a form with G , finding the g_μ and determining under what conditions that yield $|g_\mu| < 1$.

The difference equations in 1-D are of the form

$$u_j^{n+1/2} = u_j^{n-1/2} - \frac{\Delta t}{\Delta x} (f_{j+1}^n - f_{j-1}^n) \quad (\text{A.5a})$$

or

$$E_j^{n+1/2} = E_j^{n-1/2} - \frac{\Delta t}{\varepsilon \Delta x} (H_{j+1/2}^n - H_{j-1/2}^n) \text{ from } \left(\frac{\partial D}{\partial t} + \frac{\partial H}{\partial x} \right) = 0, \quad (\text{A.5b})$$

$$H_{j+1/2}^n = H_{j+1/2}^{n-1} - \frac{\Delta t}{\mu \Delta x} (E_{j+1}^{n-1/2} - E_j^{n-1/2}) \text{ from } \left(\frac{\partial B}{\partial t} + \frac{\partial E}{\partial x} \right) = 0. \quad (\text{A.5c})$$

By substituting (A.5c) into (A.5b) and rearranging, one obtains

$$E_j^{n+1/2} = E_j^{n-1/2} + \left(\frac{v \Delta t}{\Delta x} \right)^2 (E_{j+1}^{n-1/2} - 2E_j^{n-1/2} + E_{j-1}^{n-1/2}) - \frac{\Delta t}{\varepsilon \Delta x} (H_{j+1/2}^{n-1} - H_{j-1/2}^{n-1}), \quad (\text{A.5d})$$

$$H_{j+1/2}^n = H_{j+1/2}^{n-1} - \frac{\Delta t}{\mu \Delta x} (E_{j+1}^{n-1/2} - E_j^{n-1/2}). \quad (\text{A.5e})$$

Now let
$$\hat{u}^n = \begin{pmatrix} \hat{E}^{n-1/2} e^{ikx} \\ \hat{H}^{n-1} e^{ik(x+\Delta x/2)} \end{pmatrix}. \quad (\text{A.6a})$$

Hence, $\hat{u}^{n+1} = G\hat{u}^n$ can be written as

$$\hat{u}^{n+1} = \begin{bmatrix} 1 + \left(\frac{v \Delta t}{\Delta x} \right) (e^{ik\Delta x} - 2 + e^{-ik\Delta x}) & -\frac{\Delta t}{\varepsilon \Delta x} (1 - e^{-ik\Delta x}) \\ -\frac{\Delta t}{\mu \Delta x} (e^{-ik\Delta x} - 1) & 1 \end{bmatrix} \hat{u}^n \quad (\text{A.6b})$$

where the following equation have been used

$$\left. \begin{aligned} E_{j+1}^{n-1/2} - E_j^{n-1/2} &= \left(\hat{E}^{n-1/2} e^{ikx_j} \right) \cdot \left(e^{ik\Delta x} - 1 \right) \\ E_{j+1}^{n-1/2} - 2E_j^{n-1/2} + E_{j-1}^{n-1/2} &= \left(\hat{E}^{n-1/2} e^{ikx_j} \right) \cdot \left(e^{ik\Delta x} - 2 + e^{-ik\Delta x} \right) \end{aligned} \right\}. \quad (\text{A.6c})$$

Thus, the eigenvalues of (A.3c) may be found from the determinant of $|G - g|$, by setting the determinant to zero so that

$$\left\{ \left[1 + \left(\frac{v\Delta t}{\Delta x} \right) \right]^2 (e^{ik\Delta x} - 2 + e^{-ik\Delta x}) - g \right\} \cdot (1 - g) - \left(\frac{v\Delta t}{\Delta x} \right)^2 (e^{ik\Delta x} - 2 + e^{-ik\Delta x}) = 0, \quad (\text{A.6d})$$

this simplifies to

$$g^2 - \left[2 \left(\frac{v\Delta t}{\Delta x} \right)^2 (e^{ik\Delta x} - 2 + e^{-ik\Delta x}) \right] g + 1 = 0. \quad (\text{A.6e})$$

For $(v\Delta t)/(\Delta x) = 1$ or equivalently $\Delta t = \Delta x/v$ the expression further simplifies to

$$g^2 - 2(\cos k\Delta x)g + 1 = 0 \quad (\text{A.6f})$$

and

$$\begin{aligned} g &= \frac{2(\cos k\Delta x) \pm \sqrt{4 \cos^2 k\Delta x - 4}}{2} \\ &= \cos k\Delta x \pm \sqrt{\cos^2 k\Delta x - 1} \end{aligned} \quad (\text{A.6g})$$

$$= \cos k\Delta x \pm i \sin k\Delta x$$

Therefore $|g| = 1$ and the scheme is stable for $\Delta t = \Delta x/v$ in 1-D. In 3-D and for cubical cells the stability condition generalizes to $\Delta t = \Delta x/\sqrt{3}v$.

APPENDIX B

PROPAGATION OF PLANE WAVE IN PML MEDIUM

Consider a wave whose electric field of magnitude E_0 forms an angle φ with the y axis as depicted in Fig. B.1. The magnitude of magnetic field components H_{zx} and H_{zy} are denoted as H_{zx0} and H_{zy0} . If the plane wave propagates in the PML medium, then the four components of the field can be expressed as

$$E_x = -E_0 \sin \varphi \cdot e^{i\omega(t-\alpha x-\beta y)} \quad (\text{B.1a})$$

$$E_y = E_0 \cos \varphi \cdot e^{i\omega(t-\alpha x-\beta y)} \quad (\text{B.1b})$$

$$H_{zx} = H_{zx0} e^{i\omega(t-\alpha x-\beta y)} \quad (\text{B.1c})$$

$$H_{zy} = H_{zy0} e^{i\omega(t-\alpha x-\beta y)} \quad (\text{B.1d})$$

where ω is the pulsation of the wave, t is the time, and α and β are complex constants.

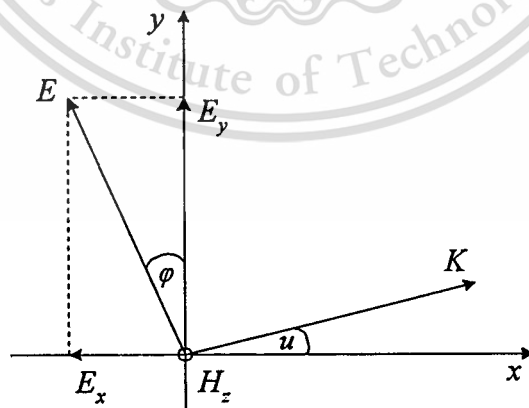


Fig. B.1 The transverse electric problem

Since the magnitude E_0 is given, the set of (B.1) involves four unknown quantities to be determined, α , β , H_{zx0} and H_{zy0} . Enforcing E_x , E_y , H_{zx} , H_{zy} from (B.1) in the PML

This material is reserved for educational use only, not allowed for commercial use.

Forbidden to modify the content, and cite the document when use.

equations for TE case yields the following set of equations connecting the four unknowns:

$$\varepsilon_0 E_0 \sin \varphi - i \frac{\sigma_y}{\omega} E_0 \sin \varphi = \beta (H_{zx0} + H_{zy0}) \quad (\text{B.2a})$$

$$\varepsilon_0 E_0 \cos \varphi - i \frac{\sigma_x}{\omega} E_0 \cos \varphi = \alpha (H_{zx0} + H_{zy0}) \quad (\text{B.2b})$$

$$\mu_0 H_{zx0} - i \frac{\sigma_x^*}{\omega} H_{zx0} = \alpha E_0 \cos \varphi \quad (\text{B.2c})$$

$$\mu_0 H_{zy0} - i \frac{\sigma_y^*}{\omega} H_{zy0} = \beta E_0 \sin \varphi \quad (\text{B.2d})$$

Obtaining H_{zx0} and H_{zy0} from (B.2c) and (B.2d) and bringing them respectively into (B.2a) and (B.2b) yields

$$\varepsilon_0 \mu_0 \left(1 - i \frac{\sigma_y}{\varepsilon_0 \omega} \right) \sin \varphi = \beta \left[\frac{\alpha \cos \varphi}{1 - i(\sigma_x^*/\mu_0 \omega)} + \frac{\beta \sin \varphi}{1 - i(\sigma_y^*/\mu_0 \omega)} \right] \quad (\text{B.3a})$$

$$\varepsilon_0 \mu_0 \left(1 - i \frac{\sigma_x}{\varepsilon_0 \omega} \right) \cos \varphi = \alpha \left[\frac{\alpha \cos \varphi}{1 - i(\sigma_x^*/\mu_0 \omega)} + \frac{\beta \sin \varphi}{1 - i(\sigma_y^*/\mu_0 \omega)} \right] \quad (\text{B.3b})$$

This system of two equations connects the unknowns α and β . It may be solved by means of writing the ratio (B.3a) over (B.3b),

$$\frac{\beta}{\alpha} = \frac{\sin \varphi}{\cos \varphi} \frac{1 - i(\sigma_y/\varepsilon_0 \omega)}{1 - i(\sigma_x/\varepsilon_0 \omega)} \quad (\text{B.4})$$

and then obtaining α^2 from (B.4) and (B.3b) and β^2 from (B.4) and (B.3a). That yields two sets of (α, β) of opposite signs for two opposite directions of propagation. Choosing the positive sign we have

$$\alpha = \frac{\sqrt{\varepsilon_0 \mu_0}}{G} \left(1 - i \frac{\sigma_x}{\varepsilon_0 \omega} \right) \cos \varphi \quad (\text{B.5a})$$

$$\beta = \frac{\sqrt{\varepsilon_0 \mu_0}}{G} \left(1 - i \frac{\sigma_y}{\varepsilon_0 \omega} \right) \sin \varphi \quad (\text{B.5b})$$

where

$$G = \sqrt{w_x \cos^2 \varphi + w_y \sin^2 \varphi} \quad (\text{B.6})$$

$$w_x = \frac{1 - i(\sigma_x / \varepsilon_0 \omega)}{1 - i(\sigma_x^* / \mu_0 \omega)} \quad (\text{B.7a})$$

$$w_y = \frac{1 - i(\sigma_y / \varepsilon_0 \omega)}{1 - i(\sigma_y^* / \mu_0 \omega)} \quad (\text{B.7b})$$

Denoting as ψ any component of the field, ψ_0 its magnitude, and c the speed of light, with (B.1) and (B.5), we can write.

$$\psi = \psi_0 e^{i\omega(t - (x \cos \varphi + y \sin \varphi) / cG)} e^{-(\sigma_x \cos \varphi / \varepsilon_0 cG)x} e^{-(\sigma_y \sin \varphi / \varepsilon_0 cG)y} \quad (\text{B.8})$$

The last two unknowns H_{zx0} and H_{zy0} can be found as functions of α and β from (B.2c) and (B.2d), and then enforcing the α and β values (B.5) yields

$$H_{zx0} = E_0 \sqrt{\varepsilon_0 / \mu_0} \frac{1}{G} w_x \cos^2 \varphi \quad (\text{B.9a})$$

$$H_{zy0} = E_0 \sqrt{\varepsilon_0 / \mu_0} \frac{1}{G} w_y \sin^2 \varphi \quad (\text{B.9b})$$

Taking into account (B.6), the summation of H_{zx0} and H_{zy0} is then

$$H_0 = E_0 \sqrt{\varepsilon_0 / \mu_0} G \quad (\text{B.10})$$

and the ratio Z of the electric magnitude over the magnetic one is

$$Z = \sqrt{\mu_0/\varepsilon_0} \frac{1}{G} \quad (\text{B.11})$$

For formulas (B.8) and (B.11), an important occurrence is when both (σ_x, σ_x^*) and (σ_y, σ_y^*) satisfy the condition,

$$\frac{\sigma}{\varepsilon_0} = \frac{\sigma^*}{\mu_0} \quad (\text{B.12})$$

Then, the quantities w_x, w_y, G , equal unity at any frequency, and so the expression of the wave components (B.8) and of the impedance (B.11) become respectively

$$\psi = \psi_0 e^{i\omega(t - (x \cos \varphi + y \sin \varphi)/c)} e^{-(\sigma_x \cos \varphi / \varepsilon_0 c)x} e^{-(\sigma_y \sin \varphi / \varepsilon_0 c)y} \quad (\text{B.13})$$

$$Z = \sqrt{\mu_0/\varepsilon_0} \quad (\text{B.14})$$

The first exponential of (B.13) shows that the wave phase propagates normally to the electric field (that means $u = \varphi$ on Fig. B.1) with the speed of light c . The last two exponentials rule the magnitude of the wave which decreases exponentially along x and y . Formula (B.14) shows that the impedance of the medium equals that of vacuum. The matching impedance condition (B.12) of the lossy medium is a matching impedance condition for the PML media too. Differences lie only in the fact that in the case of PML media, two couples of conductivities must satisfy (B.12), both (σ_x, σ_x^*) and (σ_y, σ_y^*) .

APPENDIX C

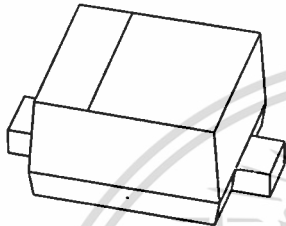
DATA SHEET OF BAP51-02 GENERAL PURPOSE PIN DIODE



This material is reserved for educational use only, not allowed for commercial use.

Forbidden to modify the content, and cite the document when use.

DATA SHEET



BAP51-02 General purpose PIN diode

Product specification
Supersedes data of 1999 Jul 01

2000 Jul 06

Philips
Semiconductors



PHILIPS

This material is reserved for educational use only, not allowed for commercial use.

General purpose PIN diode

BAP51-02

FEATURES

- Low diode capacitance
- Low diode forward resistance.

APPLICATIONS

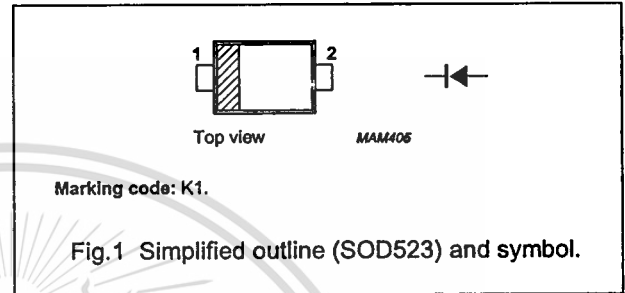
- General RF applications.

DESCRIPTION

General purpose PIN diode in a SOD523 ultra small SMD plastic package.

PINNING

PIN	DESCRIPTION
1	cathode
2	anode



LIMITING VALUES

In accordance with the Absolute Maximum Rating System (IEC 60134).

SYMBOL	PARAMETER	CONDITIONS	MIN.	MAX.	UNIT
V_R	continuous reverse voltage		–	60	V
I_F	continuous forward current		–	50	mA
P_{tot}	total power dissipation	$T_b = 90\text{ }^\circ\text{C}$	–	715	mW
T_{stg}	storage temperature		–65	+150	$^\circ\text{C}$
T_j	junction temperature		–65	+150	$^\circ\text{C}$

ELECTRICAL CHARACTERISTICS

$T_j = 25\text{ }^\circ\text{C}$ unless otherwise specified.

SYMBOL	PARAMETER	CONDITIONS	MIN.	TYP.	MAX.	UNIT
V_F	forward voltage	$I_F = 50\text{ mA}$	–	0.95	1.1	V
V_R	reverse voltage	$I_R = 10\text{ }\mu\text{A}$	50	–	–	V
I_R	reverse current	$V_R = 50\text{ V}$	–	–	100	nA
C_d	diode capacitance	$V_R = 0; f = 1\text{ MHz}$	–	0.4	–	pF
		$V_R = 1\text{ V}; f = 1\text{ MHz}$	–	0.3	0.55	pF
		$V_R = 5\text{ V}; f = 1\text{ MHz}$	–	0.2	0.35	pF
r_D	diode forward resistance	$I_F = 0.5\text{ mA}; f = 100\text{ MHz}; \text{note 1}$	–	5.5	9	Ω
		$I_F = 1\text{ mA}; f = 100\text{ MHz}; \text{note 1}$	–	3.6	6.5	Ω
		$I_F = 10\text{ mA}; f = 100\text{ MHz}; \text{note 1}$	–	1.5	2.5	Ω

Note

1. Guaranteed on AQL basis: inspection level S4, AQL 1.0.

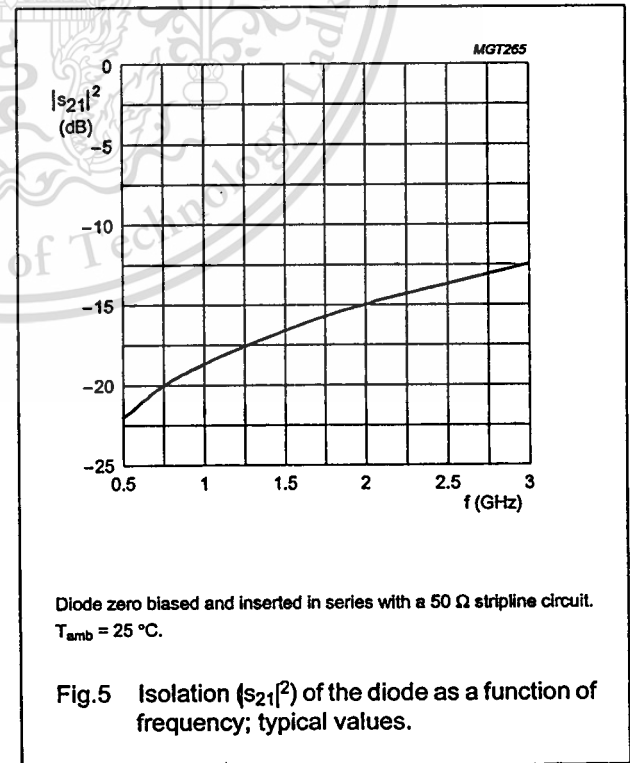
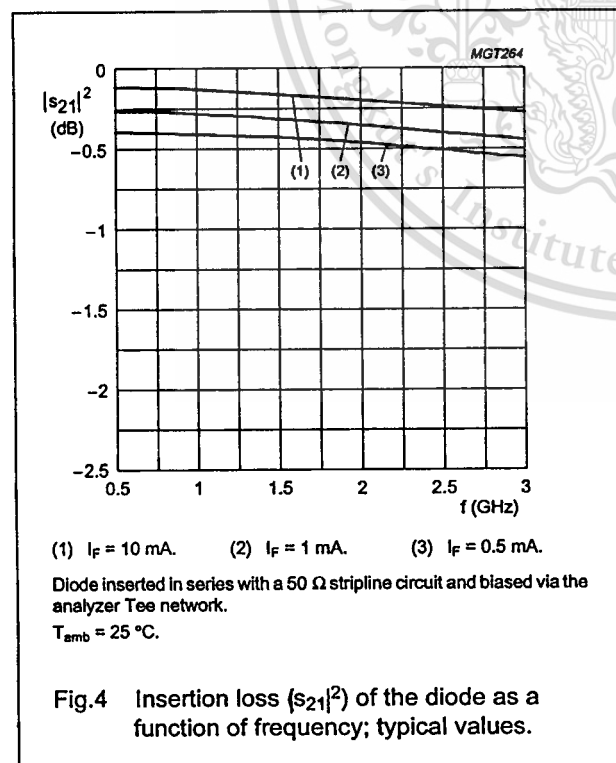
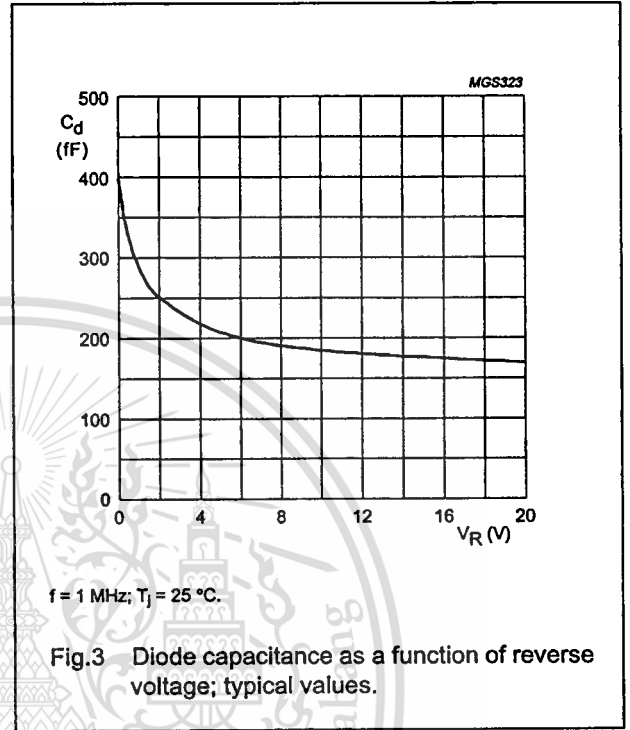
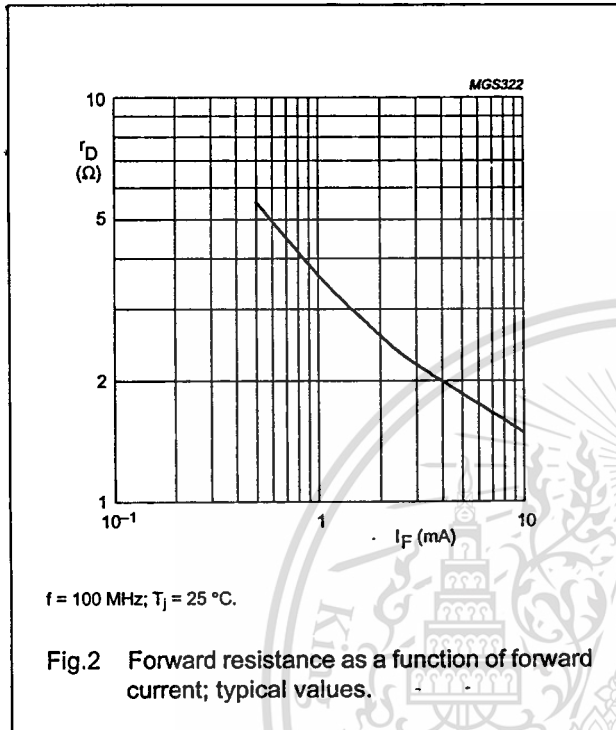
THERMAL CHARACTERISTICS

SYMBOL	PARAMETER	VALUE	UNIT
$R_{th(j-s)}$	thermal resistance from junction to soldering point	85	K/W

General purpose PIN diode

BAP51-02

GRAPHICAL DATA



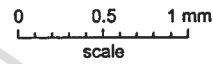
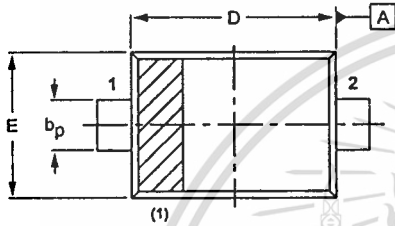
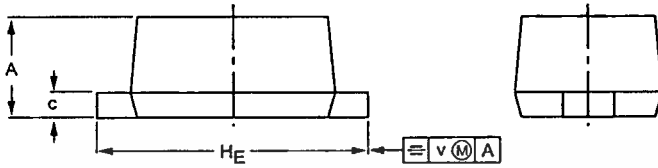
General purpose PIN diode

BAP51-02

PACKAGE OUTLINE

Plastic surface mounted package; 2 leads

SOD523



DIMENSIONS (mm are the original dimensions)

UNIT	A	bp	c	D	E	HE	v
mm	0.7 0.5	0.35 0.25	0.2 0.1	1.3 1.1	0.9 0.7	1.7 1.5	0.15

Note

1. The marking bar indicates the cathode.

OUTLINE VERSION	REFERENCES			EUROPEAN PROJECTION	ISSUE DATE
	IEC	JEDEC	EIAJ		
SOD523			SC-79		98-11-25

General purpose PIN diode

BAP51-02

DATA SHEET STATUS

DATA SHEET STATUS	PRODUCT STATUS	DEFINITIONS (1)
Objective specification	Development	This data sheet contains the design target or goal specifications for product development. Specification may change in any manner without notice.
Preliminary specification	Qualification	This data sheet contains preliminary data, and supplementary data will be published at a later date. Philips Semiconductors reserves the right to make changes at any time without notice in order to improve design and supply the best possible product.
Product specification	Production	This data sheet contains final specifications. Philips Semiconductors reserves the right to make changes at any time without notice in order to improve design and supply the best possible product.

Note

1. Please consult the most recently issued data sheet before initiating or completing a design.

DEFINITIONS

Short-form specification— The data in a short-form specification is extracted from a full data sheet with the same type number and title. For detailed information see the relevant data sheet or data handbook.

Limiting values definition— Limiting values given are in accordance with the Absolute Maximum Rating System (IEC 60134). Stress above one or more of the limiting values may cause permanent damage to the device. These are stress ratings only and operation of the device at these or at any other conditions above those given in the Characteristics sections of the specification is not implied. Exposure to limiting values for extended periods may affect device reliability.

Application information— Applications that are described herein for any of these products are for illustrative purposes only. Philips Semiconductors make no representation or warranty that such applications will be suitable for the specified use without further testing or modification.

DISCLAIMERS

Life support applications— These products are not designed for use in life support appliances, devices, or systems where malfunction of these products can reasonably be expected to result in personal injury. Philips Semiconductors customers using or selling these products for use in such applications do so at their own risk and agree to fully indemnify Philips Semiconductors for any damages resulting from such application.

Right to make changes— Philips Semiconductors reserves the right to make changes, without notice, in the products, including circuits, standard cells, and/or software, described or contained herein in order to improve design and/or performance. Philips Semiconductors assumes no responsibility or liability for the use of any of these products, conveys no licence or title under any patent, copyright, or mask work right to these products, and makes no representations or warranties that these products are free from patent, copyright, or mask work right infringement, unless otherwise specified.

AUTHOR BIOGRAPHY

Author: Mr.Phaisan Ngamjanyaporn

Date of Birth: September 11, 1977

Place of Birth: Chonburi Province, Thailand

Bachelor Degree: B.Eng. in Telecommunication Engineering

Institution: Department of Telecommunication Engineering

Faculty of Engineering

King Mongkut's Institute of Technology Ladkrabang

Year of Graduation: 1998

Interested Researches:

Antennas for mobile and wireless LAN applications

Finite-Difference Time-Domain method

Related Publications:

1. P.Ngamjanyaporn and M.Krairiksh, "A Switchable Flat Antenna for Pattern Diversity," *Proceedings of the 1999 IEEE International Symposium on Intelligent Signal Processing and Communication Systems*, Phuket, Thailand, pp.701–704, Dec. 1999.
2. P.Ngamjanyaporn and M.Krairiksh, "A Pattern Diversity Antenna for WLAN Application," *Proceedings of the 2000 Asia-Pacific Symposium on Broadcasting and Communications*, Bangkok, Thailand, pp. 258-262, Dec. 2000.